

**Siavash Iran Pour**

**Sampling the Earth's Time-Variable Gravity Field  
from Satellite Orbit**

**– Design of Future Gravity Satellite Missions –**

**München 2013**

---

**Verlag der Bayerischen Akademie der Wissenschaften  
in Kommission beim Verlag C. H. Beck**



**Sampling the Earth's Time-Variable Gravity Field  
from Satellite Orbit**

– Design of Future Gravity Satellite Missions –

Von der Fakultät Luft- und Raumfahrttechnik und Geodäsie  
der Universität Stuttgart  
zur Erlangung der Würde eines  
Doktors der Ingenieurwissenschaften (Dr.-Ing.)  
genehmigte Abhandlung

Vorgelegt von

**M.Sc. Siavash Iran Pour**

geboren in Esfahan, Iran

**München 2013**

---

Verlag der Bayerischen Akademie der Wissenschaften  
in Kommission beim Verlag C. H. Beck

Adresse der Deutschen Geodätischen Kommission:



Deutsche Geodätische Kommission

Alfons-Goppel-Straße 11 • D – 80 539 München

Telefon +49 – 89 – 23 031 1113 • Telefax +49 – 89 – 23 031 -1283 / - 1100

e-mail hornik@dgfi.badw.de • <http://www.dgk.badw.de>

Hauptberichter: Prof. Dr.-Ing. N. Sneeuw

Mitberichter: Prof. Dr.-Ing. J. Flury

Tag der mündlichen Prüfung: 29.08.2013

Diese Dissertation ist auch auf dem Dokumentenserver der Universität Stuttgart veröffentlicht

<http://elib.uni-stuttgart.de/opus/volltexte/2013/8681/>

---

© 2013 Deutsche Geodätische Kommission, München

Alle Rechte vorbehalten. Ohne Genehmigung der Herausgeber ist es auch nicht gestattet,  
die Veröffentlichung oder Teile daraus auf photomechanischem Wege (Photokopie, Mikrokopie) zu vervielfältigen.

# Contents

<b>Abbreviations</b>	<b>5</b>
<b>Abstract</b>	<b>7</b>
<b>Zusammenfassung</b>	<b>9</b>
<b>1 Introduction</b>	<b>11</b>
1.1 What is Satellite Geodesy? . . . . .	11
1.2 History of Gravity Measurement by Satellite Missions . . . . .	11
1.3 Limitations of Current Missions . . . . .	12
1.4 Future Mission Requirements and Optimizing Gravity Field Recovery . . . . .	13
1.5 Overview of the Thesis . . . . .	16
<b>2 The Earth's Gravitational Field</b>	<b>19</b>
2.1 Potential Theory . . . . .	19
2.2 Earth's Potential in terms of Spherical Harmonics . . . . .	19
2.3 Normal Field . . . . .	21
2.4 Geoid . . . . .	23
2.5 Surface Mass Density . . . . .	24
2.6 Geoid Degree Error . . . . .	25
<b>3 Sampling the Earth's Gravity Field from Satellite Orbit</b>	<b>27</b>
3.1 Reference Systems . . . . .	27
3.1.1 International Earth Rotation and Reference Systems Service (IERS) . . . . .	27
3.1.2 Rotation of the Earth . . . . .	28
3.1.3 Transformation between Reference Frames . . . . .	29
3.2 Theory of Satellite Motion . . . . .	30
3.2.1 Lagrange Planetary Equations (LPE) . . . . .	31
3.2.2 Hill's Equations (HE) . . . . .	33
3.3 Sampling the Earth's Gravity Field . . . . .	35
3.3.1 Sampling Theorems . . . . .	36
3.3.2 Satellite Ground-track Distribution . . . . .	38
<b>4 Simulation Procedure</b>	<b>43</b>
4.1 Time-variable Gravity Field . . . . .	43
4.1.1 Gravitational Forces by Mass Transport inside the Earth's System . . . . .	43
4.1.2 Gravitational Forces by Third Body . . . . .	48
4.1.3 Non-gravitational Forces . . . . .	48
4.1.4 Relativistic Effects . . . . .	49
4.2 Orbit Simulation . . . . .	49
4.2.1 Realistic Orbit . . . . .	51
4.2.2 Nominal Orbit . . . . .	52
4.2.3 Validation . . . . .	53

## Contents

4.3	Gravity Field Estimation . . . . .	53
4.3.1	Least Squares Estimation . . . . .	53
4.3.2	Regularization . . . . .	55
4.4	Empirical Orthogonal Functions (EOF) . . . . .	57
4.4.1	Basic EOF Theory . . . . .	57
4.4.2	Selection Rules . . . . .	58
4.4.3	EOF Analysis + KS-Test as a White Noise Filtering Tool . . . . .	59
4.4.4	EOF Analysis as a Correlation Analysis Tool . . . . .	60
<b>5</b>	<b>Orbit Design and Formation Flight Mission Scenarios</b>	<b>61</b>
5.1	Mission Scenarios' Design Concerns . . . . .	61
5.2	Inline (GRACE-like) Missions . . . . .	61
5.3	Alternative Formations . . . . .	71
5.4	Double Pair Missions . . . . .	74
<b>6</b>	<b>Quality Assessment of Sub-Nyquist Recovery from Future Gravity Satellite Missions</b>	<b>77</b>
6.1	Quality of the Gravity Field Recoveries . . . . .	77
6.1.1	Recovery Quality from Different Satellite Configurations and Formations	78
6.1.2	Effect of White Noise on the Recovery Quality . . . . .	94
6.2	Error Simulations and Post-processing . . . . .	99
6.2.1	Choosing the Optimal Scenarios . . . . .	99
6.2.2	Noise Filtering . . . . .	100
<b>7</b>	<b>Conclusions and Recommendations</b>	<b>111</b>
	<b>Bibliography</b>	<b>115</b>
	<b>Acknowledgments</b>	<b>121</b>

# Abbreviations

AO	Atmosphere and Ocean
AOHIS	Atmosphere, Ocean, Hydrology, Ice and Solid Earth
ANX	Ascending Node Crossing
BGC	Bristol Glaciology Centre
BMBF	Bundesministerium für Bildung und Forschung
CDF	Cumulative Distribution Function
CEP	Celestial Ephemeris Pole
CHAMP	CHAllenging Minisatellite Payload
CIO	Conventional Inertial Pole
CNR	Colombo-Nyquist Rule
DLR	Deutsches Zentrum für Luft- und Raumfahrt
DoD	US Department of Defense
ECMWF	European Centre for Medium-Range Weather Forecasts
EOF	Empirical Orthogonal Functions
ESA	European Space Agency
EWH	Equivalent Water Height
GFZ	Deutsches GeoForschungsZentrum
GOCE	Gravity Field and Steady-State Ocean Circulation
GPS	Global Positioning System
GRACE	Gravity Recovery And Climate Experiment
GRS	Geodetic Reference System
HE	Hill's Equations
IAG	International Association of Geodesy
ICRF	International Celestial Reference Frame
ICRS	International Celestial Reference System
IERS	International Earth Rotation and Reference Systems Service
InSAR	Interferometric Synthetic Aperture Radar
ITRF	International Terrestrial Reference Frame
ITRS	International Terrestrial Reference System
JPL	Jet Propulsion Laboratory
KS-Test	Kolmogorov-Smirnov Test
LEO	Low-Earth Orbit
LLR	Lunar Laser Ranging
ll-SST	low-low Satellite to Satellite Tracking
LPT	Linear Perturbation Theory
NASA	National Aeronautics and Space Administration
NCEP	US National Centre for Environmental Prediction
OMCT	Ocean Model for Circulation and Tides
PCA	Principal Component Analysis

## *Abbreviations*

PCR-GLOBWB	PCRaster GLOBAL Water Balance Model
PGR	Post-Glacial Rebound
PSD	Power Spectral Density
RC	Repeat Cycle
RMS (rms)	Root Mean Square
SC	Sub-cycle
SH	Spherical Harmonics
SLR	Satellite Laser Ranging
SMB	Surface Mass Balance
SVD	Singular Value Decomposition
VLBI	Very Long Baseline Interferometry
WGS84	World Geodetic System 1984

# Abstract

The launch of the GRACE mission has generated a broad interest within the geophysical community in the detection of temporal gravity fields and their applications, e.g. the detection of ice mass loss over Greenland and Antarctica, the hydrological cycle over Amazon and central Africa and the estimation of sea level rise. However the spatio-temporal resolution of GRACE solutions is limited by a restricted sensitivity of the metrology system, the reduced isotropy of the inline leader-follower formation (which mainly manifests itself in a North-South striped error pattern) and the temporal aliasing of high frequency time variable geophysical signals into the long time-interval solutions.

When using high quality sensors in future gravity missions, aliasing of the high frequency (short period) geophysical signals to the lower frequency (longer period) signals is one of the most challenging obstacles. Two sampling theorems mainly govern the space-time sampling of a satellite-mission: (i) a Heisenberg-type principle in satellite geodesy which states that the product of spatial resolution and time resolution is constant, and (ii) the Colombo-Nyquist rule (CNR), which requires the number of satellite revolutions in the full repeat-cycle to be equal at least twice the maximum spherical harmonic degree to be detected. The latter rule, therefore, limits the spatial resolution of the solution.

This study investigates the quality of sub-Nyquist recoveries, i.e. solutions from time intervals shorter than required by CNR, of different orbit configurations and satellite formations. In particular, the dependence of such quality on the measurement duration and ground-track patterns is investigated. It is shown that (i) the number of observations with specific coverage of the Earth by a satellite configuration (as indicated by a modified Colombo-Nyquist rule), (ii) the mission altitude and (iii) avoidance of large unobserved gaps by satellite ground-track patterns have the most important effect on the quality of the recoveries. The sub-cycle concept apparently does not play an important role in assessing the quality.

Moreover, the study investigates the modified Colombo-Nyquist rule for two pairs of satellites, where the number of revolutions by both satellite pairs is taken into account. It is also found that sub-Nyquist recoveries by such double pair scenarios outperform the ones from single inline satellite missions with twice the size of time intervals. It is indeed expected that using an inclined satellite mission, together with a near-polar mission, adds East-West measurement component to the North-South component of the near-polar satellite mission. Furthermore, the short time interval recoveries suffer less from temporal aliasing of certain time-variable gravity field components. Consequently, it means that the recovery also benefits from higher time resolution.

The gravity recovery simulations of this study are based on a quick-look tool, developed at the Institute of Geodesy, University of Stuttgart. The closed-loop simulation tool assumes a nominal repeat orbit for a satellite mission. Based on the quality assessment of the recoveries and the technical concerns with the implementation of formation flights, a near-polar moderate pendulum formation with an opening angle of less than  $10^\circ$ , approximately 300 km altitude and almost homogeneous gap evolution is suggested for a next generation of single pair gravity mission. For double pair satellite missions, a combination of a near-polar inline or moderate pendulum and a  $72^\circ$  inclined inline pair is recommended. The suggested optimal scenarios of this study are selected through the quality assessment of sub-Nyquist gravity

## *Abstract*

recoveries of different configurations.

It is also shown that the quality of the sub-Nyquist gravity recoveries can be improved by employing post processing tools. The post-processing tools of this research study include a white noise filter, based on EOF+KS-Test analysis and a regularization method which can handle all kinds of noise. The tools are employed to deal with the poorer quality of short-time interval recoveries due to the spatial aliasing, although it is almost impossible to remove all noise without diminishing some of the real signals.

# Zusammenfassung

Die Schwerefeldmission GRACE hat seit ihrem Satellitenstart ein großes Interesse innerhalb der Geowissenschaftsgemeinde in Bezug auf die Bestimmung zeitlicher Schwerefelder und deren vielfachen Anwendungen geweckt: die Modellierung des Eismassenschwundes über Grönland und der Antarktis, die Quantifizierung des Wasserkreislaufs im Amazonas-Becken und innerhalb Zentralafrikas, oder die Schätzung des Meeresspiegelanstiegs. Die räumliche und zeitliche Auflösung von GRACE Feldern ist jedoch durch einige Einflussfaktoren eingeschränkt. Dazu gehören die begrenzte Sensitivität der Messsysteme und die Nicht-Isotropie der *Leader-Follower*-Formation, was sich hauptsächlich als Nord-Süd gestreiftes Störungsmuster manifestiert. Des Weiteren schleichen sich sogenannte Aliasing-Fehler, verursacht von schnellen zeitvariablen geophysikalischen Gravitationssignalen in die monatlichen Lösungen ein.

Eine der größten Herausforderungen bei der Anwendung neuer Sensorgenerationen in zukünftige Schwerefeldmissionen besteht darin, das Aliasing kurzperiodischer geophysikalischer Signale zu begrenzen. Zwei Abtast-Theoreme beschreiben das raumzeitliche Abtastverhalten einer Satellitenmission: (i) ein Heisenberg-ähnliches Prinzip, welches besagt, dass das Produkt von räumlicher und zeitlicher Auflösung konstant ist; und (ii) die Colombo-Nyquist Regel (CNR), welche eine Anzahl von Satellitenumläufen innerhalb des Wiederholungszyklus bedingt, die mindestens dem Doppelten des maximalen Kugelfunktionsgrades entspricht. Letzteres Theorem begrenzt daher die räumliche Auflösung.

Die vorliegende Studie erforscht die Qualität von sub-Nyquist Schwerefeldlösungen, also von Lösungen aus Zeitintervallen die kürzer sind als strikt von CNR benötigt, unterschiedlicher Orbitkonfigurationen und Satellitenformationen. Insbesondere wird die Abhängigkeit dieser Qualität von dem Beobachtungszeitraum und dem Muster der Satellitenbodenspuren untersucht. Es zeigt sich, dass die Qualität der Schwerefeldlösungen wesentlich von folgenden Faktoren beeinflusst wird: (i) das raum-zeitliche Abtastverhalten einer Satellitenkonfiguration, ausgedrückt durch eine modifizierte CNR, (ii) die Höhe der Satellitenbahn und (iii) das Vermeiden von großen unbeobachteten Lücken in der Zeitentwicklung der Bodenspur. Offensichtlich spielt beim Letzteren das *sub-cycle* Konzept keine bedeutende Rolle.

Darüber hinaus erforscht die Arbeit eine modifizierte Colombo-Nyquist Regel für zwei Satellitenpaare, bei der die Anzahl der Umläufe beider Satellitenpaare berücksichtigt wird. Es wird sogar gezeigt, dass sub-Nyquist Ergebnisse zweier Satellitenpaare die Ergebnisse eines einzelnen Satellitenpaares mit doppelter Messdauer übertreffen. In einer Konfiguration zweier *in-line* Satellitenpaare, das eine polar und das andere auf einer geneigten Bahn, stellt man wie erwartet eine gewisse Ost-West Sensitivität fest. Des Weiteren wird festgestellt, dass die Schwerefeldlösungen aus kurzen Beobachtungszeiträumen weniger von Aliasing-Fehlern betroffen sind. Folglich profitieren die Lösungen von einer höheren zeitlichen Auflösung.

Die Schwerefeldsimulationen dieser Arbeit basieren auf einem *quick-look* Instrument, welches am Geodätischen Institut, Universität Stuttgart, entwickelt wurde. Das *closed-loop* Verfahren geht von Satellitenmissionen mit nominalen Wiederholungsbahnen aus. Basierend auf der Qualitätsbewertung der Schwerefeldlösungen und der technischen Realisierbarkeit von Formationsflügen empfiehlt sich als potenzielle künftige Schwerefeldmission (in Einzelpaar-Modus) der Einsatz einer moderaten Pendelformation (mit einem Öffnungswinkel von weniger

## *Zusammenfassung*

als  $10^\circ$ ) auf einer fast-polaren Bahn in etwa 300 km Höhe. Das Wiederholungsmuster sollte dabei so gewählt werden, dass die Bodenspur sich ohne große Beobachtungslücken entwickelt. Für Missionen bestehend aus zwei Satellitenpaaren könnte das eine Paar im in-line Modus oder als moderates Pendel (fast-)polar die Erde umkreisen, das zweite Paar dagegen auf einer Bahn mit z.B.  $72^\circ$  Bahnneigung fliegen. Die vorgeschlagenen Optimal-Szenarien dieser Arbeit stammen aus der Bewertung einer Vielzahl von sub-Nyquist Schwerefeldlösungen unterschiedlicher Konfigurationen.

Es wurde ebenso festgestellt, dass die Qualität der sub-Nyquist Schwerefeldlösungen durch Nachprozessierungsverfahren verbessert werden kann. Methodisch wurde einerseits eine empirische Orthogonalzerlegung (EOF) mit anschließender Kolmogorov-Smirnov (KS) Testanalyse eingesetzt, was in der Kombination einen kräftigen Filter zum Unterdrücken von weißem Rauschen darstellt. Andererseits konnten mittels Regularisierung weitere Rauscharten behandelt werden. Die Nachprozessierungswerkzeuge sind teilweise in der Lage, Aliasing-Fehler zu beseitigen. Die Gefahr besteht nichtsdestotrotz, dass gleichzeitig Signale mitrausgefiltert werden.

# 1 Introduction

## 1.1 What is Satellite Geodesy?

Helmert (1880) defined geodesy as *the science of the measurement and mapping of the Earth's surface*. Measuring devices are mainly operating within the Earth's gravity field. Therefore, most of the geodetic observations are gravity field dependent. That means gravity field mapping always come with geometric mapping.

Utilizing satellites for mapping and determination of gravity field of the Earth is the subject of satellite geodesy. Therefore, satellite geodesy mainly deals with the following problems (Seeber, 2003):

1. Determination of precise global, regional and local three-dimensional positions, e.g. the establishment of geodetic control;
2. Determination of Earth's gravity field and functionals of the field such as a precise geoid;
3. Measurement and modelling of geodynamical phenomena, e.g. polar motion, Earth rotation.

Dynamic Satellite Geodesy is the application of celestial mechanics to geodesy. In particular, it describes the satellite orbits under the influence of gravitational forces. That also provides a tool for gravity field recovery from orbit analysis when we know how gravity disturbances cause orbit perturbations. Therefore, the satellites in dynamic satellite geodesy are employed as gravity field sensing devices, where the satellites are considered as passive point masses whose orbit is mostly controlled by the gravity field of the Earth. The problem in dynamical satellite geodesy can be simplified as follows: Given the orbit from observations, determine the gravity field. That means the satellite geodesy is within the celestial mechanics. However, when satellite observations are used for solving the geophysical problems, it is connected to many disciplines like hydrology, meteorology, solid Earth study, oceanography, etc.

## 1.2 History of Gravity Measurement by Satellite Missions

After the launch of SPUTNIK-1 in 1957, satellite geodesy became an active field of geodetic research. The tracking of SPUTNIK-1 provided important information for determining the oblateness of the Earth which is responsible for the largest difference of the real Earth from spherical shape.

During the years 1959 – 2000, several techniques and satellites were employed for Earth's gravity field determination. Among them were the Doppler tracking from U.S. Navy TRANET network, Earth-to-Lunar Tracking, satellite altimetry and GPS tracking in the following decades. During these years, satellite methods with increased observation accuracy were increasingly employed by the surveying community and replaced conventional methods (Seeber,

2003).

The launch of the German satellite CHALLENGING Minisatellite Payload (CHAMP) in 2000, managed by German Research Centre for Geosciences (GFZ) and German Aerospace Center (DLR), opened a new era in modelling the Earth's gravity field. One of the goals of CHAMP was to determine of the Earth's gravity field using a high precision GPS receiver (Reigber et al., 1999).

In 2002 the satellite pair Gravity Recovery And Climate Experiment (GRACE) was launched. The GRACE mission aimed for improvement of the gravity field determination using tracking between the two low satellites (ll-SST), i.e. a tracking pair of satellites in Low Earth Orbit (LEO) (Figure 1.1). The mission was capable of measuring the time-variable gravity field, and increased spatial resolution of mass transport measurement inside the Earth system. The original GRACE mission was designed for five years performance in orbit. However, the satellite mission provided gravity field measurements beyond the designated lifetime up to the time of writing this statement, but the batteries failure may shorten lifetime of the mission at any time. Moreover, the mission may run out fuel and changes its orbit to lower altitudes due to atmospheric drag forces. The launch of GRACE provided unprecedented improvement in determining the Earth's gravity field and the data are vastly used for geophysical purposes, among them for hydrological, glaciology and atmospheric studies. The GRACE mission consists of two identical satellites in near-polar orbit (by inclination of  $89^\circ$ ) that are separated in along-track direction by approximately 220 km. The mission altitude is approximately 500 km, but due to lack of altitude control, the satellites' orbit continually decays by atmospheric drag forces. A K-Band microwave ranging system is employed to measure the distance change between the two satellites at level of few tenths of micron/second. The main observable of the GRACE satellite mission is the set of inter-satellite range-rate measurement. The GPS receivers on the satellites allow for precise orbit determination of the satellites as well as precise time-tagging of the inter-satellite range-rate measurements (Tapley et al., 2004). Moreover, each spacecraft is equipped with a high precision accelerometer to measure and remove the effect of all non-conservative forces like atmospheric drag, solar radiation pressure, Earth radiation pressure which allows to isolate the gravitational motion of the satellites (Touboul et al., 1999).

The single satellite mission Gravity Field and Steady-State Ocean Circulation (GOCE) was designed to concentrate on a higher resolution and much more accurate static field model of the Earth's gravity field (Drinkwater et al., 2007). The mission was launched in March 2009 by the European Space Agency (ESA) and the first results from the mission showed a great success in achieving its targets. However, due to its special design, the mission is not able to determine the time-variable gravity field.

### 1.3 Limitations of Current Missions

The GRACE satellite mission has provided the time varying gravity field at about 400 km spatial resolution and monthly time resolution. The satellite GOCE, on the other hand, provides the static gravity field at spatial scale of 100 km. However, there is still room for improvement of both static and time variable fields. Figure 1.2 illustrates frames of spatial and temporal scales covered by the GRACE and GOCE satellite missions together with gravity field recovery requirements of future gravity missions in different spatial and temporal scales of Earth's geophysical processes. It is seen that while some geophysical phenomena like sea level change is within the provided resolution by GRACE, other phenomena such as ocean tides and instantaneous or small co-seismic deformation are beyond the capability of GRACE to detect. Several previous studies (e.g. Loomis et al., 2011) discuss the largest errors associated

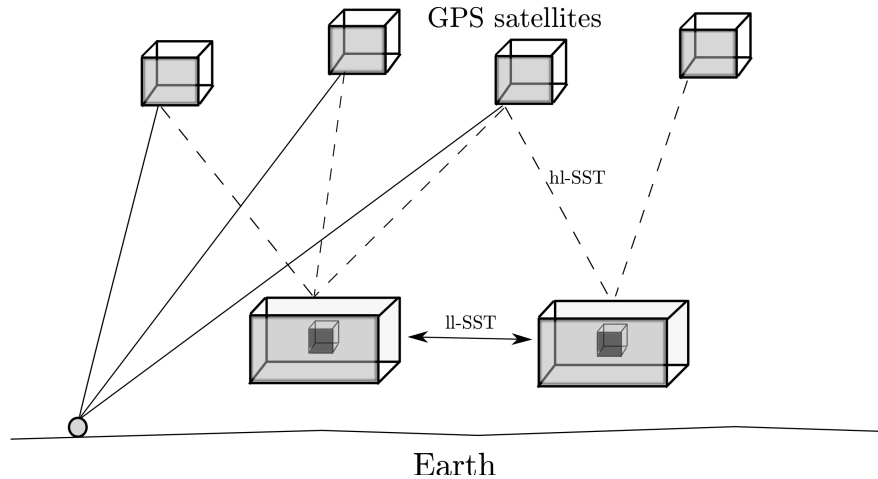


Figure 1.1: Measurement principle of GRACE configuration.

with the GRACE mission such as the errors within the microwave ranging instrument, the accelerometers, attitude control, orbit determination, temporal aliasing due to undersampling geophysical signals and mis-modelling unwanted signals. Moreover, Bonin et al. (2012) make a discussion over the poor measurement ability and reliability of high frequency signals for the short time solutions of GRACE. These errors are obviously the subjects of improvement in the design of next generation of satellite missions for time-variable gravity field.

## 1.4 Future Mission Requirements and Optimizing Gravity Field Recovery

Obviously, it is not possible to determine the full range of spatial and temporal scales of gravity field by any single satellite mission. However, with the design of future missions, one can achieve more than what is now provided by GRACE and GOCE. As it has been mentioned, not only the design of mission orbit and formation type, but also the improvement in measuring instrument and the geophysical models (provided by other methods like terrestrial gravity information) contribute to the final improvement of gravity field recovery.

Regarding the aliasing error by under-sampling, it is very important to consider two main sampling theorems which govern the space-time sampling of a satellite-mission:

- (i) a Heisenberg-type principle in satellite geodesy which states the product of spatial resolution and time resolution is constant (ESA, 2007; Reubelt et al., 2010);
- (ii) the Colombo-Nyquist rule (CNR), which requires the number of satellite revolutions in the full repeat-cycle to be equal or at least twice the maximum spherical harmonic degree to be detected (Colombo, 1984).

CNR limits the maximum spherical harmonic degree to detect and consequently the spatial resolution of the gravity solution. That means the short-time gravity solutions of a satellite mission with high temporal resolution but with the time-interval shorter than the CNR requirement suffer from insufficient samples in the spatial domain which is then responsible for significant spatial aliasing. The problem is also caused by inhomogeneous satellite coverage of the Earth system in short-time intervals. On the other hand, the long-time gravity solutions with high spatial resolution suffer from low temporal resolution. The trade-off between spatial and temporal resolutions is addressed by a Heisenberg-type principle in satellite geodesy.

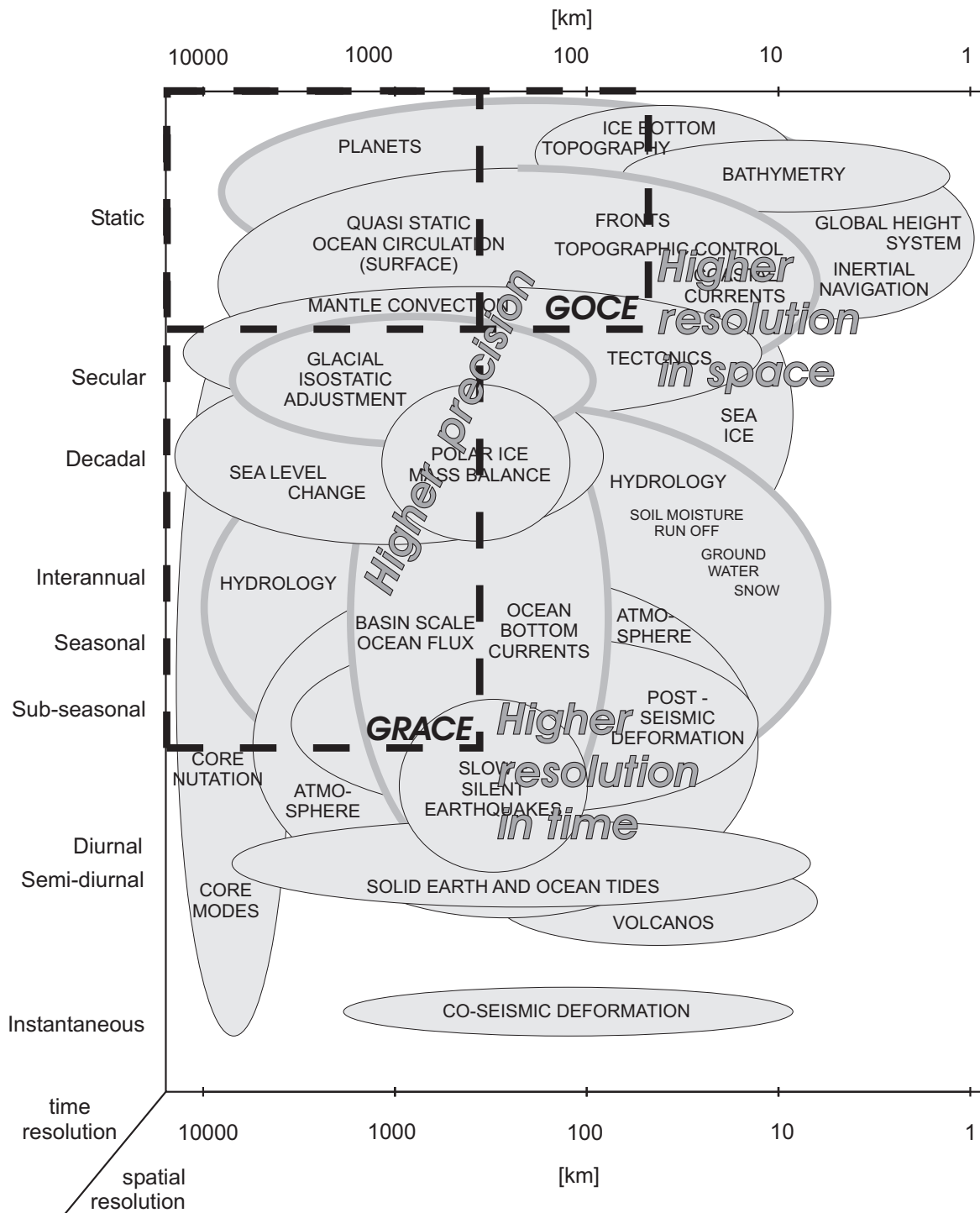


Figure 1.2: Spatial and temporal scales of geophysical processes and gravity recovery requirements after GRACE and GOCE (Sneeuw et al., 2005).

However, the works by Visser et al. (2011) and Weigelt et al. (2012) show the spatial resolution can be improved, not by twice the maximum degree  $L_{\max}$ , but by  $L_{\max}$  itself. That means one may achieve satisfying gravity solutions in the time-intervals which are shorter than what is required by CNR.

The Colombo-Nyquist rule can be expressed as follows: When using high quality sensors in future gravity missions, aliasing of the short period geophysical signals to the longer period signals is one of the most challenging obstacles for improving the quality of gravity field recovery. In other words, under-sampling of geophysical signals causes aliasing of high frequency signals to the lower frequencies. The Nyquist sampling rule, in general, implies that for the geophysical phenomena with the frequencies higher than half of the sampling frequency, the signals alias to the lower frequencies phenomena. In satellite geodesy, this law is expressed by Colombo-Nyquist rule (as above). Different strategies have been introduced to deal with this problem. For example,

- (i) more frequent sampling with more than one pair of satellite missions as Bender et al. (2008) show by employing a second pair of GRACE-like (inline) satellite formation in an inclined orbit (in addition to the original near-polar inline mission);
- (ii) improving the geophysical models by other methods to subtract their effects on the final solutions for geophysical signals of interest (dealiasing), particularly, dealiasing of atmosphere, ocean and tides by better modelling to deduce hydrological and ice signals (e.g. improved non-tidal atmospheric and oceanic de-aliasing for GRACE and SLR satellites, Flechtner et al., 2010);
- (iii) co-estimating the parameters which vary at high frequencies, like estimating spherical harmonic coefficients which describe the high frequency signals (e.g. estimating low resolution gravity fields at short time intervals to reduce temporal aliasing errors, Wiese et al., 2011a).

Another important problem associated with a GRACE-like formation is the correlation between coefficients of a specific order and the same parity of degree which leads to longitudinal (North-South) striping in the gravity solutions. This problem is due to the fact that GRACE-like formation scenarios are not sensitive to the East-West variations of the gravity field. The difficulty arises when we want to separate the correlated coefficients in the estimation process. Different techniques are introduced by several studies, categorized to:

- (i) the methods which are independent of outside information and based on empirical filters (Swenson and Wahr, 2006; Chambers, 2006; Chen et al., 2007; Schrama et al., 2007; Wouters and Schrama, 2007; Davis et al., 2008; Duan et al., 2009);
- (ii) the methods which use the error-covariance information (Koch and Kusche, 2002; Kusche, 2007; Klees et al., 2008; Save, 2009; Lorenz, 2009; Kurtenbach, 2011).

There are other sources of errors associated with the quality of gravity recoveries. However, even for the current GRACE, the error sources are not completely understood (Visser et al., 2010). By simulation tools, one can investigate the effect of individual error sources separately, although it can be just an approximation of reality. Here, a very brief discussion of two of these error sources is given.

The K-band microwave ranging instrument in GRACE mission measures the inter-satellite baseline distances to the micrometer level which makes a limit in the spatial resolution of gravity recoveries. Bender (1992); Colombo and Chao (1997); Bender et al. (2003); Aguirre-Martinez and Sneeuw (2002) discuss replacement of the microwave ranging instrument with

## 1 Introduction

a laser interferometer which allows to measure the inter-satellite distances with higher accuracy. By the replacement, the expected improvement in sensor precision is approximately 3 orders of magnitude which is, then, in nanometer level.

Another limit of GRACE mission performance is the use of accelerometers to measure the non-gravitational forces. In contrast, the GOCE mission takes advantage of single-axis drag-free control by using a shielded proof mass as a reference point which can be employed for the inter-satellite measurements. The mission accelerometry senses drag forces and compensates them by employing electric propulsion. The proof mass acceleration noise of GOCE is lower than the noise level of an accelerometer. That is because the uncertainty associated with accelerometer scale factor is avoided. The GOCE mission successfully implemented single-axis drag-free control (Drinkwater et al., 2007). Further developments in drag-free system may allow us to benefit from better sensitivity of short wavelength features of the gravity field by flying the spacecraft in lower altitudes (Aguirre-Martinez and Sneeuw, 2002). However, flying at lower altitudes causes drag forces to increase exponentially which limits the lifetime of the mission. This fact should also be considered when formation flights for future missions are designed. As an example, the GRACE mission was originally designed for 5 years in operation at an altitude of 480 km, while GOCE is expected to be in operation for approximately 2 years at its orbit around 255 km.

Finally, it should also be mentioned that some previous studies (Sharifi et al., 2007; Wiese et al., 2009; Elsaka, 2010; ESA, 2011) show that alternative formations like Pendulum, Cartwheel, LISA, ... which measure other components than only the along-track GRACE measurement component improve the quality of the gravity recoveries. Moreover, dealing with the Heisenberg-type principle in satellite geodesy, Bender et al. (2008) suggests that employing two pairs of satellites, one pair in a near-polar orbit and the other in a lower inclined orbit, improves the quality of recoveries of the time-variable gravity field in both spatial and temporal domains. A range of parameters' choices for the dual satellite missions are also suggested by Wiese et al. (2011b) for the mission design. Obviously, these studies should also be integrated to the work of searching for the optimal solutions of future gravity satellite missions. Moreover, one important issue which should be considered in orbit design is the coverage pattern of satellite mission i.e. the distribution of ground-tracks. It is expected that the mission scenarios with different ground-track distributions result in different spatial resolutions of gravity recoveries.

Clearly, from the viewpoint of orbit and formation flight design, it is desirable to have the best possible resolution in time and space domains, for example by employing more pairs of satellites in lower altitudes than GRACE. However, the technical problems associated with some of the formations as well as costs of those scenarios limit the search space to the formation flights which are optimal in all the involving areas.

### 1.5 Overview of the Thesis

The purpose of this research is to assess the quality of short-time (high temporal resolutions) gravity recoveries, when the number of samples is smaller than required by the Colombo-Nyquist Rule. Although Kurtenbach (2011) explains methods to achieve even daily solution by help of Kalman filter and external signal information, this work mostly searches for optimal satellite configurations and formation flights for sub-Nyquist time interval solutions. Thus, the sampling issue by different scenarios is at the center of attention here. A quick-look software is employed in closed loop simulations of different scenarios and the effect of orbital coverage by given satellite configurations is studied as well. Furthermore, the improvement of gravity recovery quality by employing more than one satellite mission and alternative forma-

tions is investigated. Afterwards, Empirical Orthogonal Functions (EOF) analysis together with Kolmogorov-Smirnov test (KS-Test) for white noise identification and filtering as well as regularization are exploited as post-processing tools to handle the spatial resolution decrease of retrieved fields. In addition, EOF analysis is used as a correlation analysis tool for quality assessment of the retrieved gravity fields by different mission scenarios.

This study assumes the use of a laser interferometry tracking system for inter-satellite distance measurement, and does neither consider non-gravitational forces nor gravitational forces by third body objects (Sun, Moon and the planets). Furthermore, only the temporal aliasing effect of geophysical models by different orbit configurations, formation flights and different time-interval gravity solutions as well as the effect of white noise on the solutions are investigated. The aliasing effects in a colored noise environment is not included in this study.

A short description for each of the remaining six chapters is provided as follows:

- *Chapter 2* provides an overview of mathematical background and basis needed for description of Earth's gravity field. The Earth's potential field is described in terms of spherical harmonic coefficients. Moreover, the relevant properties of spherical harmonics are briefly discussed.
- *Chapter 3* presents the basics of satellite geodesy. The chapter contains a brief overview of reference systems, Earth rotation, Linear Perturbation Theory (LPT), Hill's Equations of satellite motion and the determination of the Earth's gravity field from satellite orbit. A trade-off between spatial and temporal resolutions by satellite missions in terms of the fundamental sampling theorems and the sub-cycle concept are briefly discussed.
- *Chapter 4* starts with an overview of gravitational forces acting on a satellite and the time-variable gravity field models used in this study. The important non-gravitational forces are also briefly mentioned. Two tools, an orbit integration software and a quick-look simulation tool, which are employed for simulating the orbits of satellite mission scenarios in the time-variable Earth's gravity forces are introduced. A comparison of the results by the orbit simulation softwares is then given. Moreover, a regularization method in data inversion for gravity solution is introduced in this chapter. The chapter also provides a mathematical overview of Empirical Orthogonal Functions (EOF) analysis together with Kolmogorov-Smirnov test (KS-Test) as a post-processing tool for dealing with white noise. Furthermore, a brief discussion over the use of EOF as a correlation analysis tool for comparison of the input and output of the closed loop simulation of this study is provided.
- *Chapter 5* This chapter provides a short discussion over satellite orbit design for future satellite mission scenarios. The Earth coverage by satellite ground-tracks of different single pair inline missions and the scheme design of alternative formations and double pair scenarios are briefly discussed.
- *Chapter 6* deals with assessment of quality of sub-Nyquist gravity field recovery of different satellite orbit configurations and formation flights. In this chapter, the quality of gravity solutions of the time-intervals with the number of satellite revolutions below the required number by Colombo-Nyquist rule is investigated. Furthermore, three satellite mission scenarios with near-optimal gravity solutions in terms of spatial and temporal resolutions are chosen and then subjected to the post-processing tools.
- *Chapter 7* contains a brief summary and conclusion of the dissertation. Recommendations for further research are also provided.



## 2 The Earth's Gravitational Field

This chapter provides an overview of the mathematical background needed for a description of Earth's gravity field. The Earth's potential field is described in terms of spherical harmonic coefficients. Moreover, some important properties of spherical harmonics are briefly discussed.

### 2.1 Potential Theory

According to Newton's universal law of gravitation, the attraction force between two masses  $m_1$  and  $m_2$  at a distance  $r = r_2 - r_1$  from each other is

$$\mathbf{F} = -Gm_1m_2 \frac{\mathbf{r}_2 - \mathbf{r}_1}{\|\mathbf{r}_2 - \mathbf{r}_1\|^3} \quad (2.1)$$

where  $G$  is the *universal gravitational constant* with the value  $(6672 \pm 4) \times 10^{-14} \text{ m}^3\text{s}^{-2}\text{kg}^{-1}$ . By combining the Equation (2.1) and Newton's second law  $F = ma$ , one can find the acceleration of the particle  $m_2$  under the attraction force by particle  $m_1$  by

$$\mathbf{a} = -Gm_1 \frac{\mathbf{r}_2 - \mathbf{r}_1}{\|\mathbf{r}_2 - \mathbf{r}_1\|^3} \quad (2.2)$$

The acceleration  $\mathbf{a}$  is called the gravitational field which is described here by  $\mathbf{g}(\mathbf{r})$ . Because gravitation is a conservative force, i.e. the work done by gravitational field from one position to another is path-independent, the gravitational force vector can be written as the gradient vector of a scalar potential function  $V$ :

$$\mathbf{g}(\mathbf{r}) = \nabla V(\mathbf{r}) \quad (2.3)$$

With a mass distribution over a body  $Q$ , the gravitational force function at point  $P$  can be obtained as an integral over the total volume  $v$  with a vector length  $\mathbf{l}$  and a continuous density function  $\rho(\mathbf{r}_Q)$ :

$$\mathbf{g}(\mathbf{r}_P) = -G \iiint_v \rho(\mathbf{r}_Q) \frac{\mathbf{l}}{l^3} dv \quad (2.4)$$

Therefore, the continuous gravitational potential  $V$  over the whole space is obtained by

$$V(\mathbf{r}) = G \iiint_v \rho(\mathbf{r}_Q) \frac{1}{l} dv \quad (2.5)$$

The formula implies that the potential at infinity gets zero value.

### 2.2 Earth's Potential in terms of Spherical Harmonics

The total force on a body at rest on the surface of the Earth is the vectorial summation of attractive gravitational force and the centrifugal force coming from the Earth's rotation. This summation is called gravity.

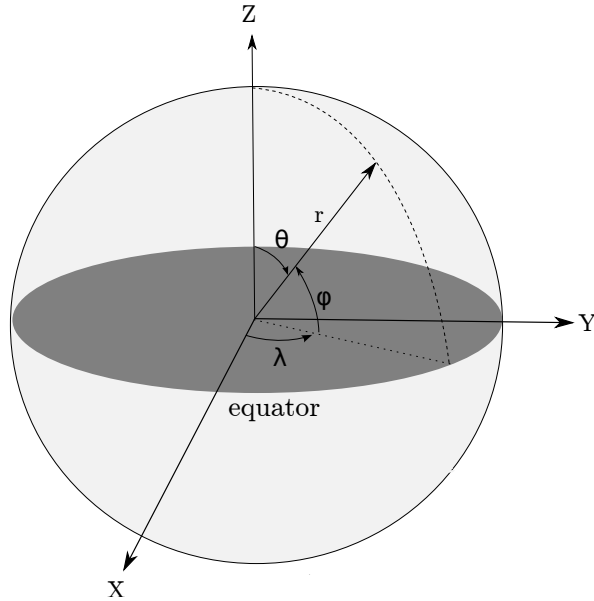


Figure 2.1: Spherical coordinates representation.

The centrifugal potential which is due to centrifugal force is not difficult to handle by an analytic function. Then, the gravitational potential,  $V$ , is the most difficult part which needs more attention. Considering this fact that the gravitational potential is a harmonic function outside an attracting mass, we can then expand the function into a series of spherical harmonics. This spectral way of representation of the potential by spherical harmonics is advantageous for many purposes in geodesy and geophysics.

The gravitational potential,  $V$ , of a point mass outside the Earth's surface is the solution to Laplace's equation (Hofmann-Wellenhop and Moritz, 2006):

$$\nabla^2 V = \frac{\partial^2 V}{\partial x^2} + \frac{\partial^2 V}{\partial y^2} + \frac{\partial^2 V}{\partial z^2} = 0 \quad (2.6)$$

The equation above is in Cartesian coordinates which is not very convenient when dealing with the Earth's potential. A more natural system of coordinates are the spherical coordinates with the following conversion to Cartesian coordinates:

$$\begin{pmatrix} x \\ y \\ z \end{pmatrix} = \begin{pmatrix} r \sin \theta \cos \lambda \\ r \sin \theta \sin \lambda \\ r \cos \theta \end{pmatrix} \quad (2.7)$$

where  $r$  is the distance between the center of mass of the Earth to the point mass,  $\theta$  is the colatitude and  $\lambda$  is the longitude of the point mass in spherical coordinates (Figure 2.1).

Therefore, the Laplace equation in the spherical coordinates is obtained as follows

$$\nabla^2 V = \frac{1}{r^2} \frac{\partial}{\partial r} \left( r^2 \frac{\partial V}{\partial r} \right) + \frac{1}{r^2 \sin \theta} \frac{\partial}{\partial \theta} \left( \sin \theta \frac{\partial V}{\partial \theta} \right) + \frac{1}{r^2 \sin^2 \theta} \frac{\partial^2 V}{\partial \lambda^2} = 0 \quad (2.8)$$

Using "separation of variables" method for solving the Laplace equation, the gravitational potential is written in the following form

$$V = R(r)\Theta(\theta)\Lambda(\lambda) \quad (2.9)$$

After many mathematical steps, the gravitational potential can be determined as

$$V(r, \theta, \lambda) = \frac{GM}{R_E} \sum_{l=0}^{\infty} \left(\frac{R_E}{r}\right)^{l+1} \sum_{m=0}^l P_{lm}(\cos \theta) (C_{lm} \cos m\lambda + S_{lm} \sin m\lambda) \quad (2.10)$$

where  $R_E$  is the Earth's radius,  $G$  is the universal gravitational constant,  $M$  is the Earth's mass,  $P_{lm}(\cos \theta)$  are the associated Legendre functions and  $C_{lm}$  and  $S_{lm}$  are the spherical harmonic coefficients with  $l$  and  $m$  degree and order of the coefficients. The dimensioning of the equation is performed by the constant factor  $GM/R_E$ .

Leaving out the radial part in (2.10) gives the potential at the surface. For reasons of compactness, the gravitational potential is usually written in terms of surface spherical harmonic  $Y_{lm}(\theta, \lambda)$  of degree  $l$  and order  $m$  as follows:

$$V(r, \theta, \lambda) = \frac{GM}{R_E} \sum_{l=0}^{\infty} \left(\frac{R_E}{r}\right)^{l+1} \sum_{m=0}^l K_{lm} Y_{lm}(\theta, \lambda) \quad (2.11)$$

where  $K_{lm}$  are spherical harmonic coefficients, corresponding to  $Y_{lm}(\theta, \lambda)$ . The surface spherical harmonic  $Y_{lm}(\theta, \lambda)$  is only a function of the angles  $\theta$  and  $\lambda$ . The radial part is, then, called solid spherical harmonics.

Surface spherical harmonics are conventionally described in different categories according to the way they divide the Earth. Cosines and sines of wave number  $m$  have  $2m$  regularly spaced zeros. On the other hand, the Legendre function  $P_{lm}(\cos \theta)$  exhibits  $(l - m)$  zero crossings in a pattern which is close to equi-angular, but not fully regular. However, the sign changes of any  $Y_{lm}(\theta, \lambda)$  in both directions tile the Earth in a checker board pattern of  $(l - m + 1) \times 2m$  pieces (Figure 2.2). The following classification is then applied (Hofmann-Wellenhof and Moritz, 2006; Sneeuw, 2006a):

- $m = 0$ : *Zonal spherical harmonics* - In the case  $m = 0$ , the sine-part is zero, that means the coefficients  $S_{l,0}$  do not exist. Furthermore, with the condition of  $m = 0$ , the cosine-part equals 1, i.e. there is no variation, but with  $P_{l,0}$  we get  $(l + 1)$  latitude bands which are called zones.
- $l = m$ : *Sectorial spherical harmonics* - With this condition,  $2l$  sign changes occur in longitude direction, but there is no change in direction of the latitudes. The Earth is divided in so-called sectors which are longitude bands.
- $l \neq m$  and  $m \neq 0$ : *Tesseral spherical harmonics* - By this condition, the Earth gets a pattern of tiles with alternative sign. These functions are called tesseral.

## 2.3 Normal Field

Geodetic observables are functions of geometry ( $r$ ) and the gravity field ( $W$ ) of the Earth:

$$f = f(r, W) \quad (2.12)$$

A Taylor series with truncation after the linear term is employed to provide a linear observation equation of (2.12). In order to perform this linearization a rotationally symmetric ellipsoid is used as a proper approximation. The *geoid* which is a representation of Earth's physical shape, deviates only less than 100 m from this ellipsoid.

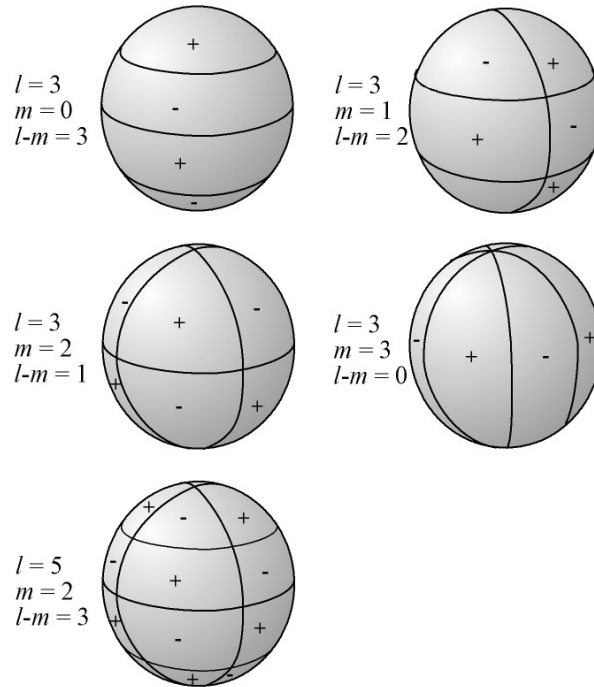


Figure 2.2: Schematic representation of some examples of surface spherical harmonics (Courtesy: Wikipedia).

The potential and the gravity field with that ellipsoid are called *normal potential* and *normal gravity* (Hofmann-Wellenhopf and Moritz, 2006). The actual gravity potential  $W$ , then, is described by the following linearization:

$$W = U + T \tag{2.13}$$

where  $W$  is the full gravity potential,  $U$  is the normal potential and  $T$  is the disturbing potential. To use a standard global normal field for everyone, International Association of Geodesy (IAG) has introduced number of commonly accepted Geodetic Reference System (GRS) over the last century. Tabel 2.1 shows the parameters of GRS30, GRS67 and the current GRS80 which has been adopted by many global and regional systems and datums. For example, the WGS84 uses the parameters from GRS80 with some small changes. In this table,  $a$  is the semi-major axis of the ellipsoid,  $f$  is ellipsoid flattening,  $GM_0$  is the Earth's gravitational constant and  $\omega$  is the Earth rotation rate. The flattening coefficient is given by

$$f = \frac{a - b}{a} \tag{2.14}$$

where  $a$  and  $b$  are respectively the semi-major (equatorial radius) and semi-minor (polar radius) axes of the ellipsoid.

The geometry of the ellipsoid is determined by the semi-major axis,  $a$ , and the flattening,  $f$ , for respectively size and shape of the ellipsoid. The physical field (here: normal gravity) is described by the geocentric gravitational constant,  $GM_0$ , and the Earth rotation rate,  $\omega$ . These 4 parameters define the normal field completely, although any other set of 4 independent parameters would do the same. For instance, GRS80 uses the dynamical form factor  $J_2$  instead of geometric factor  $f$ .

The normal potential has the following properties (Hofmann-Wellenhopf and Moritz, 2006;

Table 2.1: Basic parameters of normal fields

	GRS30	GRS67	GRS80
$a$ [m]	6378388	6378160	6378137
$f^{-1}$	297	298.247167	298.257222
$GM_0$ [ $10^{14} \text{ m}^3 \text{ s}^{-2}$ ]	3.986329	3.986030	3.986005
$\omega$ [ $10^{-5} \text{ rad s}^{-1}$ ]	7.2921151	7.2921151467	7.292115

Sneeuw, 2006a):

- it is rotationally symmetric (zonal)
- it has equatorial symmetry,
- it is constant on the ellipsoid.

The last property defines the rotating Earth ellipsoid to be an *equipotential surface* or *level surface*.

## 2.4 Geoid

The *geoid* is defined as a surface of constant gravity potential energy coinciding with the mean sea level. The geoid height,  $N$ , is then defined with respect to a reference ellipsoid (Figure 2.3). The disturbing potential,  $T$ , is defined as the difference between the actual potential on the geoid,  $W$ , and the normal potential,  $U$ , associated with the reference ellipsoid (Torge, 2001):

$$T = W - U \quad (2.15)$$

After some mathematical calculations and approximation, we obtain

$$T = \frac{GM_0}{R_E} \sum_{l=2}^{\infty} \sum_{m=0}^l \left( \frac{R_E}{r} \right)^{l+1} \bar{P}_{lm}(\cos \theta) (\bar{C}_{lm}^* \cos m\lambda + \bar{S}_{lm}^* \sin m\lambda) \quad (2.16)$$

where

$$\begin{aligned} \bar{C}_{lm}^* &= \bar{C}_{lm} - \bar{c}_{lm} \\ \bar{S}_{lm}^* &= \bar{S}_{lm} - \bar{s}_{lm} \end{aligned}$$

and  $\bar{P}_{lm}$ ,  $\bar{C}_{lm}$  and  $\bar{S}_{lm}$  are fully normalized associated Legendre functions and fully normalized potential coefficients (Torge, 2001):

$$\begin{aligned} \bar{P}_{lm}(\cos \theta) &= \left[ \frac{(2l+1)(l-m)!}{(l+m)!} \right]^{1/2} P_{lm}(\cos \theta) \\ \left\{ \begin{array}{l} \bar{C}_{lm} \\ \bar{S}_{lm} \end{array} \right\} &= \left[ \frac{(l+m)!}{(2l+1)(l-m)!} \right]^{1/2} \left\{ \begin{array}{l} C_{lm} \\ S_{lm} \end{array} \right\} \end{aligned}$$

Please note that  $\bar{c}_{lm}$  and  $\bar{s}_{lm}$  are the coefficients associated to normal potential,  $U$ , while  $\bar{C}_{lm}$  and  $\bar{S}_{lm}$  are associated to full gravity potential,  $W$ . Moreover, the Equation (2.16) assumes that the origin of the coordinate system is located at the Earth's center of mass, therefore all terms with  $l = 1$  are zero.

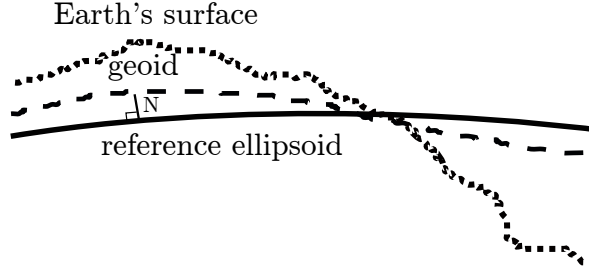


Figure 2.3: Schematic representation of reference ellipsoid and geoid, and definition of geoid height  $N$ .

The *geoid height*,  $N$ , is calculated from the disturbing potential (Torge, 2001):

$$N = \frac{T}{\gamma} \quad (2.17)$$

where  $\gamma = \frac{GM}{r^2}$ . The  $\gamma$  definition, here, uses a spherical approximation for the Earth, whereas  $\gamma$  in reality is taken from the reference ellipsoid.

Combining the equations above provides the geoid height in terms of spherical harmonics which is also a function of time  $t$ :

$$N(t) = R_E \sum_{l=2}^{\infty} \sum_{m=0}^l \bar{P}_{lm}(\cos \theta) \left( \bar{C}_{lm}^*(t) \cos m\lambda + \bar{S}_{lm}^*(t) \sin m\lambda \right) \quad (2.18)$$

The gravitational signal change in terms of geoid height (from one time epoch to another epoch) is therefore determined as follows

$$\Delta N = R_E \sum_{l=2}^{\infty} \sum_{m=0}^l \bar{P}_{lm}(\cos \theta) (\Delta \bar{C}_{lm} \cos m\lambda + \Delta \bar{S}_{lm} \sin m\lambda) \quad (2.19)$$

where  $\Delta \bar{C}_{lm}$  and  $\Delta \bar{S}_{lm}$  are the coefficients change in time, here. Since the normal field difference out from one time to the next time, its denotation has dropped. The summation to infinity is substituted by some finite maximum degree  $l_{\max}$  in practice.

## 2.5 Surface Mass Density

It is common to express the Earth's gravity field changes in terms of surface mass density. Assuming the geoid change is caused by density redistribution  $\Delta\rho(r, \theta, \lambda)$  in a layer of thickness  $H$  of Earth's surface, the surface density change,  $\Delta\sigma$ , is defined as (Wahr et al., 1998)

$$\Delta\sigma(\theta, \lambda) = \int_{\text{layer}} \Delta\rho(r, \theta, \lambda) dr \quad (2.20)$$

For a gravity satellite missions such as GRACE, this layer is on the order of 10 – 15 km, which is thick enough to include the significant mass changes in hydrological storage, ice caps, atmosphere, oceans and solid Earth.

The surface density change can be determined in terms of Legendre functions and spherical harmonics (Wahr et al., 1998)

$$\Delta\sigma(\theta, \lambda) = \frac{R_E \rho_E}{3} \sum_{l=0}^{\infty} \sum_{m=0}^l \frac{2l+1}{1+k_n} \bar{P}_{lm}(\cos \theta) (\Delta \bar{C}_{lm} \cos m\lambda + \Delta \bar{S}_{lm} \sin m\lambda) \quad (2.21)$$

where  $\rho_E$  is the Earth's average density and  $k_n$  are the elastic Love numbers as computed by Han and Wahr (1995), describing the solid Earth deformation to a load.

The Equivalent Water Height (EWH) is calculated by  $\Delta\sigma/\rho_w$  with  $\rho_w$  as the water density ( $\text{kg/m}^3$ ). Note that in (2.21), the elastic response of the Earth deformation to the load is considered. The equation also assumes that  $(l_{\max} + 2)H/R_E \ll 1$ .

## 2.6 Geoid Degree Error

The *degree variance* of the normalized potential coefficients is defined as

$$\sigma_l^2 = \sum_{m=0}^l (\bar{C}_{lm}^2 + \bar{S}_{lm}^2) \quad (2.22)$$

The *degree RMS* is then defined by

$$\sigma_l = \left( \frac{1}{2l+1} \sum_{m=0}^l (\bar{C}_{lm}^2 + \bar{S}_{lm}^2) \right)^{1/2} \quad (2.23)$$

Applying the definitions to the signal difference, the *degree difference variance* and the *degree difference RMS* are calculated as (Kim, 2000)

$$\sigma_l^2(\Delta) = \sum_{m=0}^l (\Delta\bar{C}_{lm}^2 + \Delta\bar{S}_{lm}^2) \quad (2.24)$$

$$\sigma_l(\Delta) = \left( \frac{1}{2l+1} \sum_{m=0}^l (\Delta\bar{C}_{lm}^2 + \Delta\bar{S}_{lm}^2) \right)^{1/2} \quad (2.25)$$

with

$$\begin{aligned} \Delta\bar{C}_{lm} &= (\bar{C}_{lm})_{\text{estimate}} - (\bar{C}_{lm})_{\text{truth}} \\ \Delta\bar{S}_{lm} &= (\bar{S}_{lm})_{\text{estimate}} - (\bar{S}_{lm})_{\text{truth}} \end{aligned}$$

Obviously, in the equation above, the truth can not be known in reality. However, in the frame of closed-loop simulation of this study, the input geophysical models to the simulations are considered as truth.

The *geoid degree difference variance* is given by multiplying the degree difference variance of Equation (2.24) by the square of the Earth's radius (Torge, 2001)

$$\sigma_l^2(\Delta N) = R_E^2 \sigma_l^2(\Delta) = R_E^2 \sum_{m=0}^l (\Delta\bar{C}_{lm}^2 + \Delta\bar{S}_{lm}^2) \quad (2.26)$$

The *geoid degree difference* is then defined as

$$\Delta N_l = \left( \sigma_l^2(\Delta N) \right)^{1/2} = R_E \left( \sum_{m=0}^l (\Delta\bar{C}_{lm}^2 + \Delta\bar{S}_{lm}^2) \right)^{1/2} \quad (2.27)$$

The Equation (2.27) provides the error as a function of order.



# 3 Sampling the Earth's Gravity Field from Satellite Orbit

This chapter provides the basics of satellite geodesy. The chapter contains a brief overview of reference systems, Earth rotation, Linear Perturbation Theory (LPT), Hill's Equations of satellite motion and the determination of the Earth's gravity field from satellite orbit. A trade-off between spatial and temporal resolutions by satellite missions in terms of the fundamental sampling theorems and the sub-cycle concept are briefly discussed.

## 3.1 Reference Systems

### 3.1.1 International Earth Rotation and Reference Systems Service (IERS)

The International Earth Rotation and Reference Systems Service (IERS), initiated in 1987, is concerned with the maintenance of the IERS Reference System. Different space geodetic techniques like Very Long Baseline Interferometry (VLBI), Satellite Laser Ranging (SLR), Lunar Laser Ranging (LLR) and Global Positioning System (GPS) are employed for computation of the Earth rotation parameters. In the Central Bureau, the information from different Analysis Centers and different techniques are then combined to provide the regular updates of the IERS Reference System (Seeber, 2003).

The IERS Reference System includes:

- IERS Standards, a set of models and parameters, which are used by the Analysis Centers
- the International Celestial Reference Frame (ICRF)
- the International Terrestrial Reference Frame (ITRF)

The ICRF is realized by a catalog of compact extragalactical radio sources. The ITRF is realized by a set of terrestrial station coordinates and velocities.

The definitions of Celestial and Terrestrial Reference Frames are based on realization of Celestial and Terrestrial Reference Systems.

#### Celestial Reference System

The small motions of the rotation axis of the Earth are described as the sum of following components

- astronomical precession and nutation
- polar motion

The direction of *Celestial Ephemeris Pole (CEP)* axis is computed from the theory of nutation and precession. The origin of International Celestial Reference System (ICRS) is placed at the barycenter of the solar system. The orientations of ICRS axes are then defined as the following axes at epoch J2000.0

- the CEP

### 3 Sampling the Earth's Gravity Field from Satellite Orbit

- the equinox
- perpendicular to the former two axes, completing a Cartesian coordinate system

The ICRF is a realization of the ICRS including astronomical coordinates of about 200 extragalactical radio sources at the epoch J2000.0. The transformation from the ICRF to a system with CEP as its third axis is given by the theory of nutation and precession.

#### Terrestrial Reference System

Due to the movement of CEP with respect to the surface of the Earth, it is also favorable to adopt a coordinate system which is fixed to the Earth. The International Terrestrial Reference System (ITRS) employs some definitions to set a fixed coordinate system with respect to the Earth. The *Conventional Inertial Pole (CIO)* at the epoch 1903.0 is determined by the mean direction of the rotation axis of the Earth by five International Latitude Service stations in the period 1900.0 to 1906.0. The ITRS is then defined with its origin at the Earth's geocenter. The directions of ITRS axes are defined as

- the CIO as the  $Z$ -axis
- the 1903.0 meridian of Greenwich as the  $X$ -axis
- the  $Y$ -axis perpendicular to the former two axis which completes a Cartesian coordinate system

The ITRF is then a realization of the ITRS by the Cartesian coordinates and velocities of globally distributed tracking stations.

The transformation between the ITRF and ICRF is given by the pole coordinates  $x_p, y_p$  and nutation and precession parameters  $\Delta\psi, \Delta\epsilon, \zeta, \vartheta$  and  $z$ .

#### Other Reference Systems

Several other terrestrial reference systems rather than ITRF are in use. One of the most important global systems is WGS84 which is maintained by the US Department of Defense (DoD) and is the reference system of the GPS system. The WGS84 is defined by adopting Cartesian coordinates of ten DoD GPS Monitoring Stations derived from Doppler observations on these sites. The system is realized by the ephemerides of the GPS satellites.

For many applications, ellipsoidal coordinate systems are more convenient to use than the Cartesian systems. The ellipsoidal reference systems can be divided in two main categories (i) global and (ii) local ellipsoidal reference systems which approximate the Earth respectively as a whole and a local ellipsoids.

#### 3.1.2 Rotation of the Earth

The orientation of Earth's rotation axis is changed by the gravitational torques of the Sun, Moon and the planets on the Earth's equatorial bulge. These changes are called *precession* and *nutation* and can be predicted with a very high accuracy. There is also a small change of Earth's rotation axis with respect to its crust. This small movement is called *polar motion*.

The *general precession* is a combined effect of two components

- the *Luni-solar precession* which is the circular motion of the celestial pole with a period of 25 800 years and an amplitude equal to the obliquity of the ecliptic of  $23.5^\circ$ . The Luni-solar precession causes a westerly movement of the equinox of about  $50.3''$  per year.

- the *Planetary precession* which consists of a  $0.5^\circ$  per year rotation of the ecliptic resulting in a easterly motion of the equinox by about  $12.5''$  per century and a decrease of the obliquity of the ecliptic by about  $47''$  per century.

*Nutation* is the short periodic motion of the pole, superimposed on the precession with oscillations of 1 day to the main period of 18.6 years and a maximum amplitude of  $9.2''$ .

In addition to the movement of the Earth's rotation axis in space, the rotation axis has an additional variation with respect to the Earth's crust. This motion is primarily caused by the elastic properties of the Earth and the exchange of angular momentum between the solid Earth, the oceans and the atmosphere. This variation is called polar motion and is the motion of the true celestial pole (as defined by the models of precession and nutation) relative to the  $z$ -axis of a conventionally chosen terrestrial reference system. The motion consists of a free and forced oscillations. The free oscillation is counterclockwise with a period of 430 days, which is called *Chandler period*, and an amplitude of 3 – 6 m. The forced component also consists of two parts: (i) a diurnal period part which is excited by tidal forces and has an amplitude of one order of magnitude smaller than the free oscillation, and (ii) an annual period part which is excited by the annual changes in the atmosphere and has an amplitude of about the amplitude of the free oscillation.

It should be mentioned that since the nutation and polar motion cannot be predicted by the models, space geodetic observation techniques are employed to determine them.

### 3.1.3 Transformation between Reference Frames

The transformation from the Cartesian coordinates referred to the Celestial Reference Frame at epoch  $t_i$  to the Cartesian coordinates referred to the Terrestrial Reference Frame at epoch  $t_j$  reads as (Seeber, 2003)

$$\begin{pmatrix} x \\ y \\ z \end{pmatrix}_{\text{TRF}_{t_j}} = \mathbf{S}(x_p, y_p, \text{GAST})\mathbf{N}(\epsilon, -\Delta\psi, -\epsilon - \Delta\epsilon)\mathbf{P}(-\zeta, \vartheta, -z) \begin{pmatrix} x \\ y \\ z \end{pmatrix}_{\text{CRF}_{t_i}} \quad (3.1)$$

Here, a brief discussion of the rotation matrices  $\mathbf{S}$ ,  $\mathbf{N}$  and  $\mathbf{P}$  is given.

#### Precession Transformation

The transformation between the mean celestial reference positions at epoch  $t_i$  in days since J2000.0 (1 January 2000 12:00) to the mean celestial positions at epoch  $t_j$  is performed by the following rotation matrices

$$\mathbf{P}(-\zeta, \vartheta, -z) = \mathbf{R}_z(-z)\mathbf{R}_y(\vartheta)\mathbf{R}_z(-\zeta) \quad (3.2)$$

where  $\mathbf{R}_y$  and  $\mathbf{R}_z$  are respectively the rotation matrices around  $Y$  and  $Z$  axis.

The three precession angles  $\zeta$ ,  $\vartheta$  and  $z$  read as (McCarthy and Petit, 2004)

$$\begin{aligned} \zeta &= 2.5976176'' + 2306.0809506'' T + 0.3019015'' T^2 + 0.0179663'' T^3 \\ &\quad - 0.0000327'' T^4 - 0.0000002'' T^5, \\ \vartheta &= 2004.1917476'' T - 0.4269353'' T^2 - 0.0418251'' T^3 - 0.0000601'' T^4 \\ &\quad - 0.0000001'' T^5, \\ z &= -2.5976176'' + 2306.0803226'' T + 1.094779'' T^2 + 0.0182273'' T^3 \\ &\quad + 0.000047'' T^4 - 0.0000003'' T^5 \end{aligned}$$

### 3 Sampling the Earth's Gravity Field from Satellite Orbit

where

$$T = (t_j - t_i)/365.25$$

#### Nutation Transformation

The transformation from the mean celestial reference positions at the epoch  $t$  to the instantaneous true celestial positions using the nutation matrix is as

$$\mathbf{N}(\epsilon, -\Delta\psi, -\epsilon - \Delta\epsilon) = \mathbf{R}_x(-\epsilon - \Delta\epsilon)\mathbf{R}_z(-\Delta\psi)\mathbf{R}_x(\epsilon) \quad (3.3)$$

where  $\mathbf{R}_x$ ,  $\mathbf{R}_y$  and  $\mathbf{R}_z$  are respectively the rotation matrices around  $X$ ,  $Y$  and  $Z$  axes,  $\epsilon$  is the obliquity of the ecliptic,  $\Delta\epsilon$  is the nutation in obliquity and  $\Delta\psi$  is nutation in longitude. The obliquity of ecliptic  $\epsilon$  at epoch  $t$  representing the rotation angle from the ecliptic system to the equator system is computed through

$$\epsilon = 23^\circ 26' 21.448'' - 46.815'' T - 0.00059'' T^2 + 0.001813'' T^3$$

$\Delta\psi$  and  $\Delta\epsilon$  can be computed based on the International Astronomical Union (IAU) precession-nutation model. The first terms are

$$\Delta\psi = (-17.1996'' - 0.01742'' T) \sin(\Omega) + (0.2062'' + 0.00002'' T) \sin(2\Omega) + \dots,$$

$$\Delta\epsilon = (9.2025'' + 0.00089'' T) \cos(\Omega) + (-0.0895'' + 0.00005'' T) \cos(2\Omega) + \dots$$

where  $\Omega$  is the mean ecliptic longitude of the lunar ascending node. McCarthy and Petit (2004) provides the complete series terms of  $\Delta\psi$  and  $\Delta\epsilon$ .

#### Earth Orientation Transformation

The transformation from true celestial to the conventional terrestrial system including the Earth's rotation and polar motion at same epoch is computed as

$$\mathbf{S}(x_p, y_p, \text{GAST}) = \mathbf{R}_y(-x_p)\mathbf{R}_x(-y_p)\mathbf{R}_z(\text{GAST}) \quad (3.4)$$

with GAST the Greenwich Apparent (true) Sidereal Time.

The rotation matrices for the Equation 3.4 read as

$$\mathbf{S}(x_p, y_p, \text{GAST}) = \begin{pmatrix} 1 & 0 & x_p \\ 0 & 1 & 0 \\ -x_p & 0 & 1 \end{pmatrix} \begin{pmatrix} 1 & 0 & 0 \\ 0 & 1 & -y_p \\ 0 & y_p & 1 \end{pmatrix} \begin{pmatrix} \cos(\text{GAST}) & \sin(\text{GAST}) & 0 \\ -\sin(\text{GAST}) & \cos(\text{GAST}) & 0 \\ 0 & 0 & 1 \end{pmatrix} \quad (3.5)$$

## 3.2 Theory of Satellite Motion

A satellite, revolving around a perfect sphere, would move on a perfect elliptical Kepler orbit. However, since the Earth is not spherically symmetrical and is not the only force acting on the satellite, the true satellite orbit differs from the ideal Keplerian motion. Therefore, the satellite orbit observations provide information about the satellite orbit perturbation and consequently the information over the Earth's disturbing potential. The relation between orbital perturbation and disturbing potential can be derived by different methods. Two widely used methods in celestial mechanics are respectively based on the Kaula's solution of Lagrange Planetary Equations (LPE) and the Hill's Equations (HE) (Schrama, 1989).

### 3.2.1 Lagrange Planetary Equations (LPE)

Considering only the gravitational forces on a satellite in orbit, the equation of motion with disturbing potential  $T$  in Cartesian coordinates can be expressed as

$$\ddot{\mathbf{r}} = \nabla \frac{GM}{r} + \nabla T \quad (3.6)$$

By transforming the position  $\mathbf{r}$  and velocity  $\dot{\mathbf{r}}$  of the satellite into Keplerian elements, the time derivative Keplerian elements are derived (Kaula, 1966):

$$\dot{a} = \frac{2}{na} \frac{\partial T}{\partial M} \quad (3.7a)$$

$$\dot{e} = \frac{1-e^2}{na^2e} \frac{\partial T}{\partial M} - \frac{\sqrt{1-e^2}}{na^2e} \frac{\partial T}{\partial \omega} \quad (3.7b)$$

$$\dot{I} = \frac{\cos I}{na^2\sqrt{1-e^2}\sin I} \frac{\partial T}{\partial \omega} - \frac{1}{na^2\sqrt{1-e^2}\sin I} \frac{\partial T}{\partial \Omega} \quad (3.7c)$$

$$\dot{\omega} = -\frac{\cos I}{na^2\sqrt{1-e^2}\sin I} \frac{\partial T}{\partial I} + \frac{\sqrt{1-e^2}}{na^2e} \frac{\partial T}{\partial e} \quad (3.7d)$$

$$\dot{\Omega} = \frac{1}{na^2\sqrt{1-e^2}\sin I} \frac{\partial T}{\partial I} \quad (3.7e)$$

$$\dot{M} = n - \frac{1-e^2}{na^2e} \frac{\partial T}{\partial e} - \frac{2}{na} \frac{\partial T}{\partial a} \quad (3.7f)$$

where  $n = \sqrt{GM/a^3}$  is the mean motion of the satellite and  $a$ ,  $e$ ,  $I$ ,  $\omega$ ,  $\Omega$ ,  $M$  are respectively the semi-major axis, eccentricity, inclination, argument of perigee, right ascension of ascending node and mean anomaly (see Figure 3.1). The equations of motion (3.7) are called the Lagrange Planetary Equations (LPE).

Equation (2.16) can provide an expression for the relationship between the disturbing potential and the Legendre functions and spherical harmonic coefficients in spherical coordinates of satellite positions. Kaula (1966) expresses the perturbing potential in spherical coordinates

$$\begin{aligned} T &= \sum_{l=0}^{\infty} \sum_{m=0}^l T_{lm}, \\ T_{lm} &= \frac{GM R_E^l}{a^{l+1}} \sum_{p=0}^l F_{lmp}(I) \sum_{q=-\infty}^{\infty} G_{lpq}(e) S_{lmpq}(\omega, M, \Omega, \Theta) \\ \Rightarrow T &= \sum_{l=2}^{\infty} \sum_{m=0}^l \sum_{p=0}^l \sum_{q=-\infty}^{\infty} \frac{GM R_E^l}{a^{l+1}} F_{lmp}(I) G_{lpq}(e) S_{lmpq}(\omega, M, \Omega, \Theta) \end{aligned} \quad (3.8)$$

where

$$S_{lmpq}(\omega, M, \Omega, \Theta) = \begin{bmatrix} \Delta C_{lm} \\ -\Delta S_{lm} \end{bmatrix}_{l-m: \text{ odd}}^{l-m: \text{ even}} \cos \psi_{lmpq} + \begin{bmatrix} \Delta S_{lm} \\ \Delta C_{lm} \end{bmatrix}_{l-m: \text{ odd}}^{l-m: \text{ even}} \sin \psi_{lmpq}$$

with  $\psi_{lmpq} = (l-2p)\omega + (l-2p+q)M + m(\Omega - \Theta)$ .  $F_{lmp}(I)$  and  $G_{lpq}(e)$  are respectively called inclination function and eccentricity function.  $\Theta$  is the angle between the equinox and the Greenwich meridian and is called Greenwich time GAST. Indices  $l$  and  $m$  are respectively degree and order as before, while  $p$  and  $q$  are only summation indices. Kaula (1966) provides more details of inclination and eccentricity functions.

### 3 Sampling the Earth's Gravity Field from Satellite Orbit

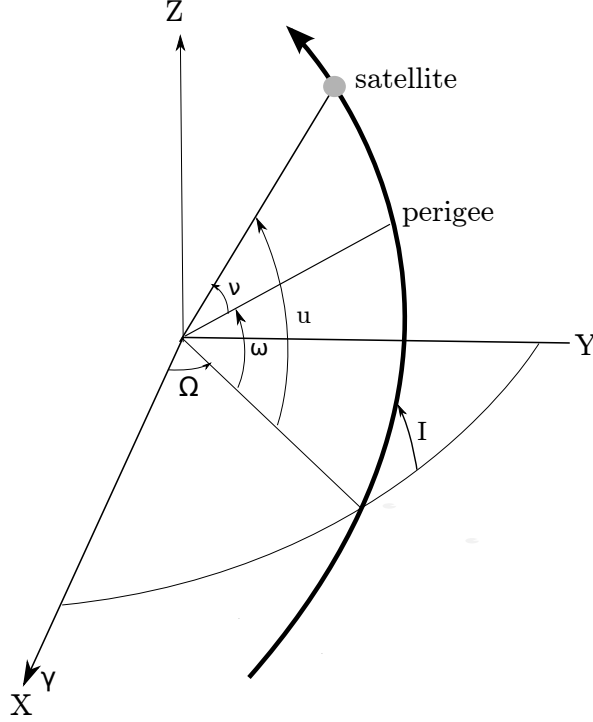


Figure 3.1: Three-dimensional geometry of Kepler orbit. The sum of angle of perigee,  $\omega$ , and true anomaly,  $\nu$ , is referred to as argument of latitude,  $u$ .

Since it is difficult to find an analytical solution of Equation (3.7), a linearization method is utilized. The linearization is (nearly) possible because  $C_{20}$  (which is responsible for parameterization of the Earth's flattening) is the biggest disturbance. The assumption for the integration is that the Keplerian elements and the Greenwich sidereal time  $\Theta$  are only linearly time dependent, i.e.  $\ddot{\omega} = \ddot{\Omega} = \ddot{M} = \ddot{\Theta} = 0$ , meaning  $\dot{\omega}$ ,  $\dot{\Omega}$ ,  $\dot{M}$  and  $\dot{\Theta}$  are constant. Therefore, the linear solution of the perturbations of Keplerian elements can be written as (Kaula, 1966; Sneeuw, 2006b)

$$\Delta a_{lmpq} = \frac{GM R_E^l}{l a^{l+2}} [2F_{lmp} G_{lpq} (l - 2p + q)] \frac{S_{lmpq}}{\dot{\psi}_{lmpq}} \quad (3.9a)$$

$$\Delta e_{lmpq} = \frac{GM R_E^l}{l a^{l+3} e} \left[ F_{lmp} G_{lpq} (1 - e^2)^{1/2} \left( (1 - e^2)^{1/2} (l - 2p + q) - (l - 2p) \right) \right] \frac{S_{lmpq}}{\dot{\psi}_{lmpq}} \quad (3.9b)$$

$$\Delta I_{lmpq} = \frac{GM R_E^l}{l a^{l+3} (1 - e^2)^{1/2} \sin I} [F_{lmp} G_{lpq} ((l - 2p) \cos I - m)] \frac{S_{lmpq}}{\dot{\psi}_{lmpq}} \quad (3.9c)$$

$$\Delta \omega_{lmpq} = \frac{GM R_E^l}{l a^{l+3}} \left[ (1 - e^2)^{1/2} e^{-1} F_{lmp} G'_{lpq} - \cot I (1 - e^2)^{-1/2} F'_{lmp} G_{lpq} \right] \frac{\bar{S}_{lmpq}}{\dot{\psi}_{lmpq}} \quad (3.9d)$$

$$\Delta \Omega_{lmpq} = \frac{GM R_E^l}{l a^{l+3} (1 - e^2)^{1/2} \sin I} \left[ F'_{lmp} G_{lpq} \right] \frac{\bar{S}_{lmpq}}{\dot{\psi}_{lmpq}} \quad (3.9e)$$

$$\Delta M_{lmpq} = \frac{GM R_E^l}{l a^{l+3}} \left[ F_{lmp} \left( -(1 - e^2) e^{-1} G'_{lpq} + 2(l + 1) G_{lpq} \right) \right] \frac{\bar{S}_{lmpq}}{\dot{\psi}_{lmpq}} \quad (3.9f)$$

where

$$\dot{\psi} = \frac{d\psi}{dt} = (l - 2p)\dot{\omega} + (l - 2p + q)\dot{M} + m(\dot{\Omega} - \dot{\Theta}) \quad (3.10a)$$

$$F'_{lmp} = \partial F / \partial I \quad (3.10b)$$

$$G'_{lpq} = \partial G / \partial e \quad (3.10c)$$

and  $\bar{S}_{lmpq}$  as

$$\bar{S}_{lmpq}(\omega, M, \Omega, \Theta) = \begin{bmatrix} \Delta C_{lm} \\ -\Delta S_{lm} \end{bmatrix}_{l-m: \text{ odd}}^{l-m: \text{ even}} \sin \psi_{lmpq} - \begin{bmatrix} \Delta S_{lm} \\ \Delta C_{lm} \end{bmatrix}_{l-m: \text{ odd}}^{l-m: \text{ even}} \cos \psi_{lmpq} \quad (3.11)$$

The  $\Delta$ 's, here, represent the perturbations to the  $J_2$  reference orbit.

The perturbations in the three main satellite directions in terms of Keplerian elements for near-circular satellite orbits were introduced by Rosborough (1986)

$$\Delta x = a(\Delta\omega + \Delta\Omega \cos I + \Delta M + 2 \sin M \Delta e + 2e \cos M \Delta M), \quad (3.12a)$$

$$\Delta y = a(\Delta I \sin(\omega + M) - \Delta\Omega \sin I \cos(\omega + M)), \quad (3.12b)$$

$$\Delta z = (\Delta a - a \Delta e \cos M + ae \Delta M \sin M) \quad (3.12c)$$

where  $\Delta x$  is perturbation in the along-track direction (in the direction of satellite velocity vector),  $\Delta y$  is the perturbation in cross-track direction and  $\Delta z$  is the perturbation in radial direction (the vector connecting the Earth's geocenter to the satellite).

Using the functions  $F_{lmp}(I)$ ,  $G_{lpq}(e)$  and  $S_{lmpq}(\omega, M, \Omega, \Theta)$ , the relation between the orbit perturbations can be written as

$$\Delta x_{lmp} = a \left( \frac{R_E}{a} \right)^l F_{lmp} \left[ \frac{2(l+1) - 3(l-2p)\gamma_{lmp}^{-1}}{\gamma_{lmp}} + \frac{4p-3l-1}{\gamma_{lmp}+1} + \frac{l-4p-1}{\gamma_{lmp}-1} \right] \bar{S}_{lmp0}, \quad (3.13a)$$

$$\begin{aligned} \Delta y_{lmp} = a \left( \frac{R_E}{a} \right)^l \frac{1}{2\gamma_{lmp}} & \left[ \left( \frac{F_{lmp}}{\sin I} ((l-2p) \cos I - m) - F'_{lmp} \right) \bar{S}_{(l+1)mp0} \right. \\ & \left. - \left( \frac{F_{lmp}}{\sin I} ((l-2p) \cos I - m) + F'_{lmp} \right) \bar{S}_{(l-1)mp0} \right] \end{aligned} \quad (3.13b)$$

$$\Delta z_{lmp} = a \left( \frac{R_E}{a} \right)^l F_{lmp} \left[ \frac{2(l-2p)}{\gamma_{lmp}} + \frac{4p-3l-1}{2(\gamma_{lmp}+1)} + \frac{4p-l+1}{2(\gamma_{lmp}-1)} \right] S_{lmp0} \quad (3.13c)$$

where

$$\gamma_{lmp} = l - 2p - m \frac{\lambda_a - \Omega + \Theta}{\omega + M} = l - 2p - m \frac{1}{\beta_d} \quad (3.14)$$

with  $\lambda_a$  is the longitude at an ascending node passage and  $\beta_d$  is the number of satellite revolutions per day.

### 3.2.2 Hill's Equations (HE)

Hill (1878) introduced an alternative set of equation of motion which is more suitable when dealing with circular orbits or orbits with small eccentricities. The approach describes the satellite motion in a reference frame which co-rotates with the satellite on a circular path (Figure 3.2). This set of equations is called Hill's Equations (HE). Schaub and Junkins (2003) provide the orbital equations referred to the orbital frame as

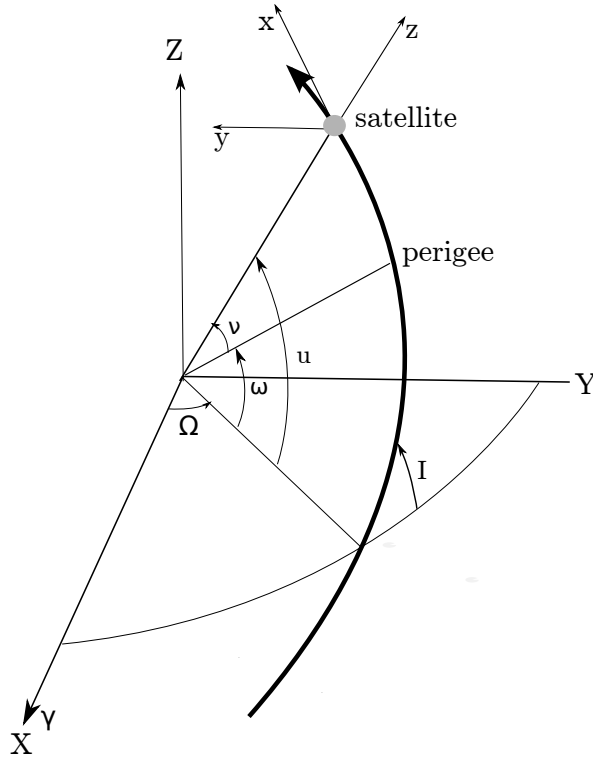


Figure 3.2: The local orbital coordinate frame:  $x$  along-track,  $y$  cross-track and  $z$  radial axis.

$$\ddot{x} + 2n\dot{z} = f_x = \frac{\partial T}{\partial x} \quad (3.15a)$$

$$\ddot{y} + n^2 y = f_y = \frac{\partial T}{\partial y} \quad (3.15b)$$

$$\ddot{z} - 2n\dot{x} - 3n^2 z = f_z = \frac{\partial T}{\partial z} \quad (3.15c)$$

with  $n$  the mean motion,  $(x, y, z)$  are the coordinates in the along-track, cross-track and radial directions and  $(f_x, f_y, f_z)$  are the components of disturbing forces along the  $(x, y, z)$  axes.

In the non-perturbed case, i.e. when  $(f_x, f_y, f_z) = (0, 0, 0)$ , the homogeneous solution of Hill's equations reads (Schrama, 1989; Sneeuw, 2006b):

$$x(t) = \frac{2}{n} \dot{z}_0 \cos nt + \left( \frac{4}{n} \dot{x}_0 + 6z_0 \right) \sin nt - (3\dot{x}_0 + 6nz_0)t + x_0 - \frac{2}{n} \dot{z}_0 \quad (3.16a)$$

$$y(t) = y_0 \cos nt + \frac{\dot{y}_0}{n} \sin nt \quad (3.16b)$$

$$z(t) = \left( -\frac{2}{n} \dot{x}_0 - 3z_0 \right) \cos nt + \frac{\dot{z}_0}{n} \sin nt + \frac{2}{n} \dot{x}_0 + 4z_0 \quad (3.16c)$$

with initial position vector of  $(x_0, y_0, z_0)$  and initial velocity vector of  $(\dot{x}_0, \dot{y}_0, \dot{z}_0)$ .

The Equation (3.16) shows that the solution of homogeneous Hill's equations mainly consists of periodic motion at the orbit frequency  $n$ . As it is seen, the  $x$ -component contains a linear term in  $t$ . Moreover, the equation shows that the  $x$ - and  $z$ -components are coupled, while the  $y$ -motion behaves as a pure oscillator, independent from the other components. The

solution of the homogeneous Hill's equations allows to analyze the motion of the GRACE-type and two alternative formations of this study in terms of the parameters in Equation (3.16) (Sharifi et al., 2007):

- Inline (GRACE-type):  $x_0 = \rho_x$ , with  $\rho_x$  as the along-track distance of two satellites and  $y_0 = z_0 = \dot{x}_0 = \dot{y}_0 = \dot{z}_0 = 0$ ;
- Pendulum:  $x_0 = \rho_x$ ,  $y_0 = \rho_y$  and  $z_0 = \dot{x}_0 = \dot{y}_0 = \dot{z}_0 = 0$ , with  $\rho_x$  the along-track distance and  $\rho_y$  the maximum cross-track distance between the satellites;
- Cartwheel (Radial wheel-type):  $z_0 = \rho_r$ ,  $\dot{x}_0 = -2nz_0$  and  $x_0 = y_0 = \dot{y}_0 = \dot{z}_0 = 0$ , with  $\rho_r$  the maximum radial distance. This type of relative motion has an ellipse shape with axis ratio 2:1.

It has to be noted that the homogeneous HE solution is no longer valid if the chief motion is not circular (as in Cartwheel formation). Small values of eccentricity can produce modelling errors comparable to those produced by  $J_2$  gravitational perturbations or atmospheric drag (Sneeuw et al., 2008). Moreover, in reality, satellites are perturbed by different disturbing forces. That is particularly caused by the Earth flattening, dominantly influences LEO satellites motion. Therefore, formation flight design would be more realistic if the  $J_2$ -field perturbation is taken into account (Sneeuw et al., 2008). The field perturbation causes a drift in the right ascension of the ascending node  $\Omega$ , the argument of perigee  $\omega$  and the mean anomaly  $M$ . A comprehensive discussion over the subject with the formulation is given in Sneeuw et al. (2008).

Supposing the satellite orbit is perturbed by a force which can be decomposed into Fourier series, the particular solution of Hill's equation is obtained. Consider the perturbation of one single frequency  $\omega$ :

$$\ddot{x} + 2n\dot{z} = f_x = A_x \cos \omega t + B_x \sin \omega t \quad (3.17a)$$

$$\ddot{y} + n^2 y = f_y = A_y \cos \omega t + B_y \sin \omega t \quad (3.17b)$$

$$\ddot{z} - 2n\dot{x} - 3n^2 z = f_z = A_z \cos \omega t + B_z \sin \omega t \quad (3.17c)$$

Then, the solution reads:

$$x(t) = \frac{(3n^2 + \omega^2)A_x + 2\omega n B_z}{\omega^2(n^2 - \omega^2)} \cos \omega t + \frac{(3n^2 + \omega^2)B_x - 2\omega n A_z}{\omega^2(n^2 - \omega^2)} \sin \omega t \quad (3.18a)$$

$$y(t) = \frac{A_y}{n^2 - \omega^2} \cos \omega t + \frac{B_y}{n^2 - \omega^2} \sin \omega t \quad (3.18b)$$

$$z(t) = \frac{\omega A_z - 2n B_x}{\omega(n^2 - \omega^2)} \cos \omega t + \frac{\omega B_z + 2n A_x}{\omega(n^2 - \omega^2)} \sin \omega t \quad (3.18c)$$

Balmino et al. (1996) show non-resonant and resonant solutions of the Hill's equations.

A more general solution of Hill's equations consist of a combination of the homogeneous and particular solutions.

### 3.3 Sampling the Earth's Gravity Field

The launch of satellite mission GRACE has generated more interest in higher temporal resolution of the mass variations within the Earth gravity field. The monthly gravity solutions of

the GRACE mission largely suffer from temporal aliasing, while the sub-monthly solutions are affected by spatial aliasing. The problem is also caused by inhomogeneous satellite coverage of the Earth system in short-time intervals. Here, the limitations by the main sampling theorems in satellite geodesy and the space-time ground-track pattern evolution are briefly discussed.

#### 3.3.1 Sampling Theorems

The aliasing problem and the spatio-temporal resolution are mainly restricted by two sampling theorems describing the space-time sampling of satellite missions:

- (i) a Heisenberg-type principle in satellite geodesy which states that the product of spatial resolution and time resolution is constant;
- (ii) the Colombo-Nyquist rule (CNR), which requires the number of satellite revolutions within the full repeat-cycle to be equal or larger than twice the maximum spherical harmonic degree to be detected.

A satellite on a  $\beta/\alpha$  repeat orbit fulfills  $\beta$  revolutions in  $\alpha$  nodal days, where  $\beta$  and  $\alpha$  are relative primes. The repeat period of such a mission is then  $T_{\text{rep}} = \alpha$  where the revolution time is  $T_{\text{rev}} = \alpha/\beta$ . Therefore, the equatorial track spacing (as a representation measure of the spatial scale) equals to  $D_{\text{space}} = 2\pi/\beta$  with  $D_{\text{time}} = \alpha$  as the temporal scale. The product between the spatial sampling and temporal sampling is thus (ESA, 2007; Reubelt et al., 2010):

$$D_{\text{space}} \times D_{\text{time}} = 2\pi\alpha/\beta = 2\pi T_{\text{rev}} \quad (3.19)$$

However, since the revolution time  $T_{\text{rev}}$  of a low-Earth orbit (LEO) varies marginally with the orbit height, the product of (3.19) can be regarded as constant. This fact is addressed by a Heisenberg-type principle as a trade-off between spatial and temporal resolution by a single satellite pair:

$$D_{\text{space}} \times D_{\text{time}} = \text{const.} \quad (3.20)$$

The term "Heisenberg-type principle in satellite geodesy" is chosen as an analogy to the Heisenberg uncertainty principle in quantum physics. That means, the better the temporal sampling is, the worse the spatial sampling becomes, and vice versa (Figure 3.3). However, the spatial resolution can be improved by additional satellite pair on interleaved ground-tracks with a  $\Delta\lambda$ -shift (longitudinal shift), whereas the temporal resolution is not changed. In a similar way, without changing the spatial resolution, adding a satellite pair on the same ground-track of the initial pair with a  $\Delta t$ -shift (time shift) improves the temporal resolution (Figure 3.3). That means, any spatio-temporal sampling requirement can be fulfilled with different repeat modes, if the time and space shifts and the number of sensors are selected adequately (Reubelt et al., 2010).

The Colombo-Nyquist rule (CNR), on the other hand, requires

$$\beta \geq 2L \text{ (or } 2M) \quad (3.21)$$

where  $\beta$  is the number of satellite revolutions in the full repeat cycle of the satellite ( $\alpha$ ). The rule states that the number of satellite revolutions in a time interval should be at least twice the maximum spherical harmonic degree ( $l$ ) and order ( $m$ ) to be detected (Colombo, 1984). This rule consequently limits the spatial resolution of the gravity recoveries. That means the spatial patterns with  $l > L_{\text{max}}$  are undersampled and alias into the solution.

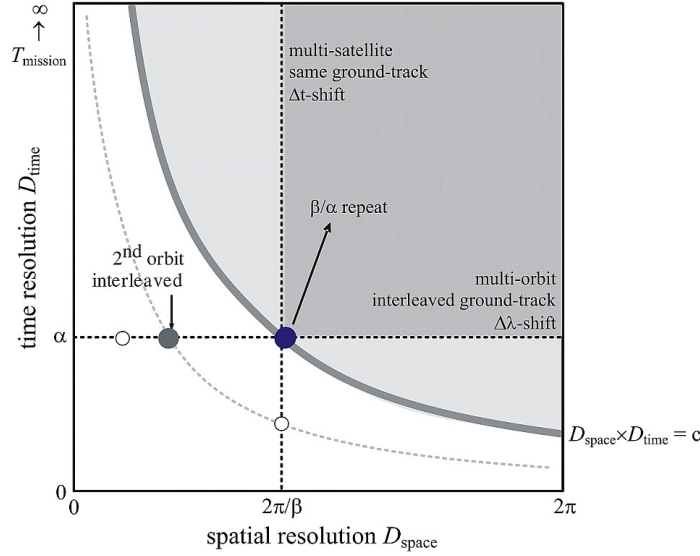


Figure 3.3: Space-time sampling of satellite configurations (ESA, 2007).

Similarly, the time-variable signals with periods  $T < 2D_{\text{time}}$  are temporally undersampled and thus alias into the solution. Equation (3.21) is generally known as the Nyquist rule-of-thumb for mapping geopotential functions. It is also referred to as the Colombo-Nyquist rule, which connects the spatial resolution with the sampling. The commensurable ratio  $\beta/\alpha$  by the satellite motion can be determined using the change rate of the Keplerian elements, particularly the true anomaly  $\nu$ , the argument of perigee  $\omega$  and the right ascension of the ascending node  $\Omega$ :

$$\frac{\beta}{\alpha} = \frac{\dot{\omega} + \dot{\nu}}{\dot{\Omega} - \omega_E} = -\frac{\dot{u}}{\dot{\Lambda}} = \frac{T_\Lambda}{T_u} \quad (3.22)$$

where  $\omega_E$  is the angular velocity of the Earth rotation, and the argument of latitude  $u$  is the sum of the true anomaly and the argument of perigee. The sum of the denominator can be considered as the change of ascending node longitude in the Earth fixed frame  $\dot{\Lambda}$ . The ratio is also associated to the revolution time of the satellite  $T_u$  and of the nodal day  $T_\Lambda$ .

In an ideal case, the sampling can be associated to a maximum resolvable frequency which is defined by the Nyquist rule for a time series, although the rule-of-thumb needs refinement for the sampling of the sphere (Weigelt et al., 2009; Visser et al., 2011). Using the Nyquist criterion, the spatial representation of the spherical harmonic development needs to be expressed as a time series (Schrama, 1990, 1991; Sneeuw, 2000). The result in a time series representation of the potential in complex notation reads as:

$$V(t) = \frac{GM}{R_E} \sum_{l=0}^L \sum_{m=-l}^l \sum_{k=-l}^l \left(\frac{R_E}{r}\right)^{l+1} \bar{K}_{lm} \bar{F}_{lmk}(I) e^{i\psi_{mk}t} \quad (3.23)$$

where  $\bar{K}_{lm}$  represents the complex-valued spherical harmonic coefficients,  $\bar{F}_{lmk}$  is the complex-valued inclination function,  $I$  is the inclination and  $i$  is the imaginary number. The summation indices are the degree  $l$ , the order  $m$  and the wave number  $k$ . The maximum degree is  $L$ . The angular variable  $\psi$  represents the spectral lines of the lumped coefficient spectrum (Sneeuw, 2000):

$$\dot{\psi}_{mk} = k\dot{u} + m\dot{\Lambda}, \text{ with } -L \leq m, k \leq L. \quad (3.24)$$

### 3 Sampling the Earth's Gravity Field from Satellite Orbit

The initial state of the angular variable  $\psi_{mk}^0$  is assumed to be zero. The avoidance of spatial aliasing requires the separation condition of two frequencies  $\dot{\psi}_{m_1, k_1} \neq \dot{\psi}_{m_2, k_2}$ . Therefore, using Equation (3.22), a transformation yields:

$$\frac{m_1 + m_2}{k_1 + k_2} \neq \frac{\beta}{\alpha} \quad (3.25)$$

From this condition, Colombo (1984) shows that in order to avoid aliasing for a given maximum degree  $L_{\max}$  at least  $\beta = 2L_{\max}$  revolutions are necessary. That means spatial patterns with  $l > L_{\max}$  are undersampled and then alias into the solution, i.e. spatial sampling (Reubelt et al., 2010). Sneeuw (2000) discusses that this is fulfilled if  $\beta \geq 2M_{\max}$  which states to be equivalent to the Nyquist rule-of-thumb used by Colombo (1984) in the conventional triangular SH domain. However, the works by Visser et al. (2011) and Weigelt et al. (2012) show that the spatial resolution can be improved, not by twice the maximum degree  $L_{\max}$  (or twice the maximum order  $M_{\max}$ ), but by  $L_{\max}$  (or  $M_{\max}$ ) itself. That means a satisfying gravity solution of the time-intervals shorter than what is required by CNR is achievable.

It should be noted that from the sampling theorem, the time-variable signals with periods  $T < 2D_{\text{time}}$  are temporally undersampled and hence alias into the solutions (Reubelt et al., 2010).

#### 3.3.2 Satellite Ground-track Distribution

It is expected that the ground-track distribution in space and time of a satellite mission scenario has influence on quality of the gravity recovery. Then, the gap evolution of the satellite mission ground-track is of great interest to be studied. If the correlation between the gap evolution, which is an indicator of homogeneity of the Earth coverage by the satellite mission scenario, and the gravity recoveries is meaningful, then one task would be to search for the mission scenarios and orbital configurations by more homogeneous coverage of the Earth. That also means for different configurations, at one point of time, the space domain is almost homogeneously sampled which is good enough for recovery of the gravity field. Then, this time interval is the temporal resolution of the gravity recovery, while the degree of homogeneity of spatial coverage of the Earth contributes to the achievable spatial resolution by the recovery. Figures 3.4 and 3.5 show the ground-track pattern of a satellite mission after specific time-intervals. The figure illustrates how the satellite ground-track fills in over time.

Assuming  $\Gamma = \beta/\alpha$  as the number of orbits (satellite revolutions),  $\beta$ , in orbital period,  $\alpha$ , the *fundamental interval* reads as  $S = 360^\circ/\Gamma$ .

$$\Gamma = \frac{\beta}{\alpha} = I + \frac{N}{\alpha} \Rightarrow \beta = I\alpha + N \quad (3.26)$$

where  $I$  is the integer part of  $\Gamma$ . The fundamental interval gives the angular space between two Ascending Node Crossing (ANX) consecutive in time. The sub-interval  $S_i$  ( $S_i = 360^\circ/\beta$ ) is therefore the sampling angle after an entire Repeat Cycle (RC) period. Hence,  $S$  can be expressed by  $S = \alpha \cdot S_i$ . Within  $S$ , the ANX of days  $n$  and  $n + 1$  are always separated by a distance of  $N$  or  $(\alpha - N)$  sub-intervals  $S_i$  (ESA, 2011).

The orbits can be classified as drifting orbits when  $N = 1$  or  $N = \alpha - 1$ , and as skipping orbits in the other cases. The sampling of the Fundamental interval of a drifting orbit is very progressive. Skipping orbits, on the other hand, feature more complex coverage pattern, that reduce the persistence of large unobserved gaps and feature a very wide range of spatial/temporal coverage patterns (ESA, 2011).

An useful graphical tool to represent the relationship between spatial and temporal sam-

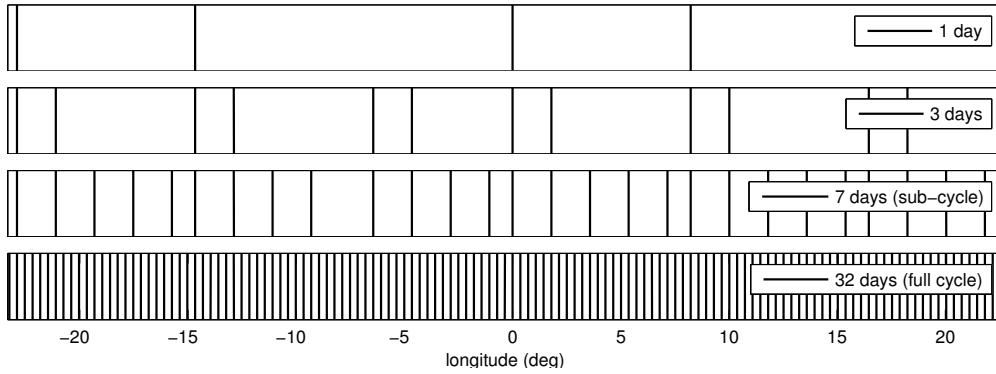


Figure 3.4: Ground-track of satellite mission scenario  $\beta/\alpha = 503/32$  (503 satellite revolutions in 32 nodal days as the orbit full repeat period) on a selected part of the Earth's equator for ascending and descending orbits, after 1, 3, 7 and 32 days.

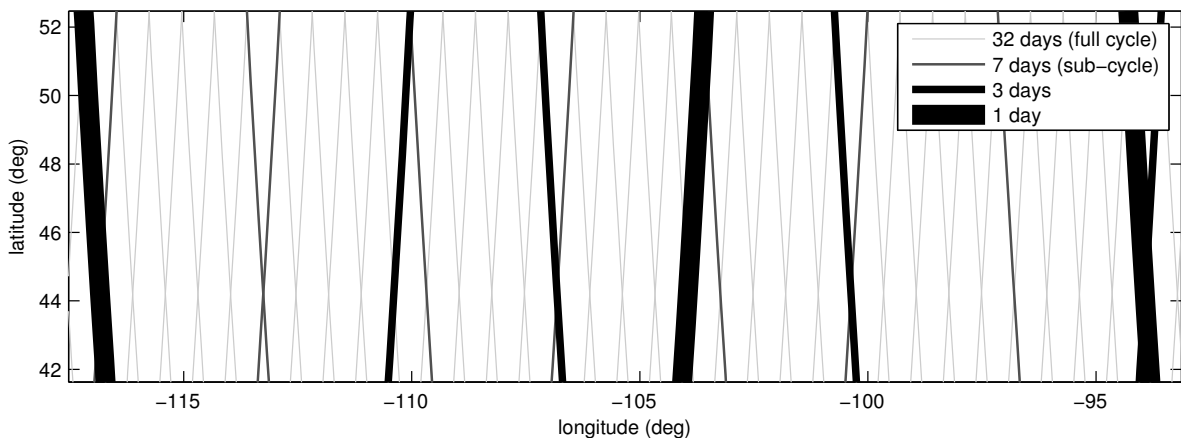


Figure 3.5: Ground-track of satellite mission scenario  $\beta/\alpha = 503/32$  (503 satellite revolutions in 32 nodal days as the orbit full repeat period) on a selected part of the Earth for ascending and descending arcs, after 1, 3, 7 and 32 days.

### 3 Sampling the Earth's Gravity Field from Satellite Orbit

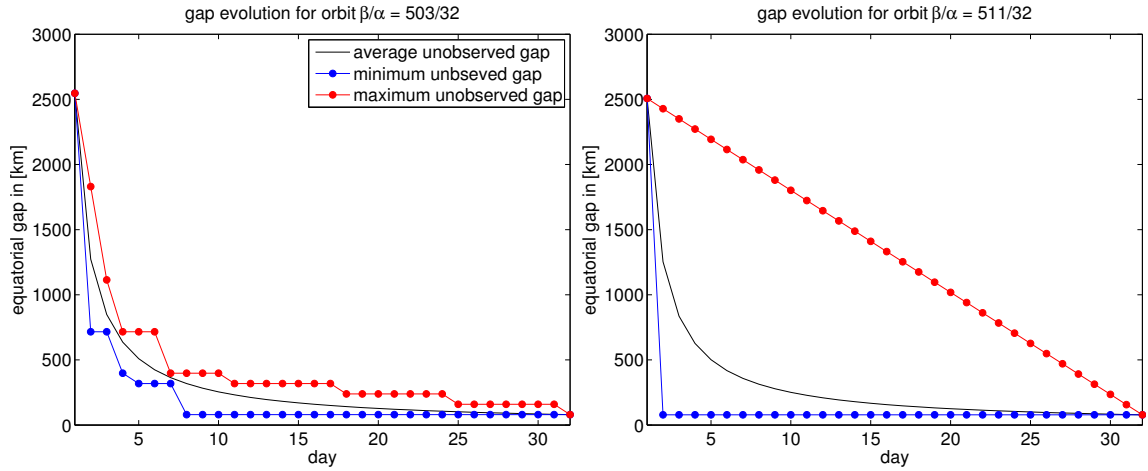


Figure 3.6: Gap evolution graphs of two repeat orbit scenarios: Rapid gap-filling (left) and slow gap-filling (right).

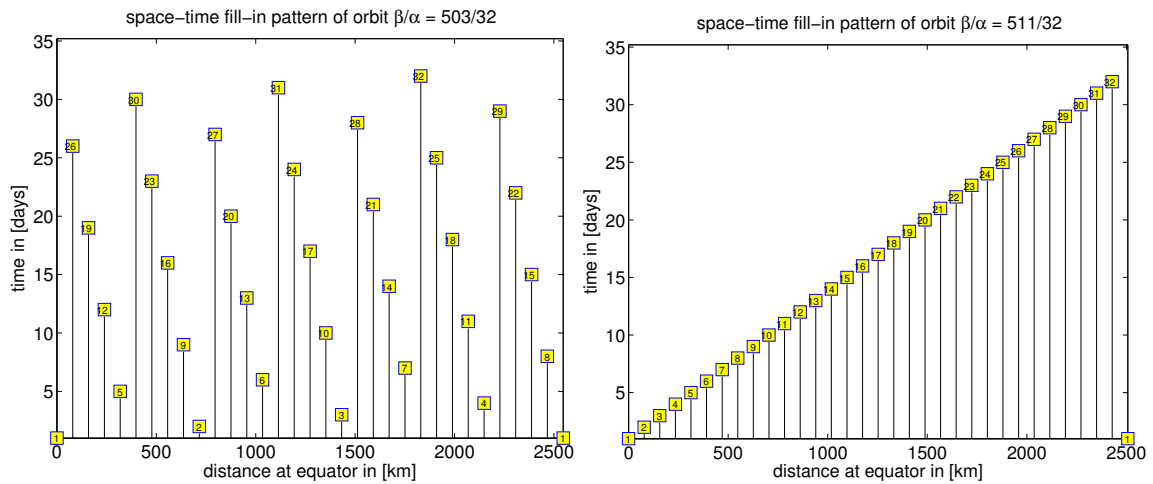


Figure 3.7: Space-time fill-in pattern graphs of the two repeat orbit scenarios of Figure 3.6.

pling is the gap evolution graph at the equator (ESA, 2011). The graphs show the minimum, the maximum and the average unobserved gaps at each day and can be employed for the study of influence of ground-track distribution on quality of the gravity solutions by different mission scenarios and time-intervals (Figure 3.6).

Another illustration tool for evolution of ground-track distribution is the space-time fill-in pattern graphs (ESA, 2011). These graphs also show how the Earth's equator is sampled in time and space (Figure 3.7). The  $X$ -axis represents the fundamental interval at the equator, while the  $Y$ -axis represents the duration of satellite orbit. Each square shows an ANX which represents when it occurs and where it falls within the Fundamental Interval (ESA, 2011).

**Sub-cycle:** The concept of sub-cycle can be also employed for studying the effect of space-time ground-track distribution on the quality of gravity recoveries.

A sub-cycle (SC) is the smallest number of days after which an ANX falls at  $1 \times S_i$  or  $(\alpha - 1) \times S_i$  from the first ANX (ESA, 2011). At the sub-cycle time-interval the minimum gap falls down to its final value. That happens after which the maximum and the minimum gaps get close to each other. The sub-cycle of a drifting orbit is obviously one day.

### 3.3 Sampling the Earth's Gravity Field

The sub-cycle is an interesting parameter to measure how fast an orbit is in reducing the largest unobserved gap. Some orbits feature additionally one or more secondary SC which are also interesting in terms of temporal sampling. Figures 3.6 and 3.7 show examples of the skipping and drifting orbits by gap evolution and space-time fill-in pattern graphs. Being the drifting orbit  $\beta/\alpha = 511/32$  (right panel of the figures), its maximum gap width is reduced as slowly as possible from  $S$  to  $S_i$  and the minimum gap is immediately as wide as  $S_i$ . The evolution of the gap width for the skipping orbit  $\beta/\alpha = 503/32$  (left panel of the figures) is clearly faster. Figures 3.4 and 3.5 illustrate the ground-track of satellite mission scenario  $\beta/\alpha = 503/32$  on a selected parts of the Earth for ascending and descending orbits, after 1, 3, 7 (sub-cycle) and 32 days (full repeat cycle) and the gap evolution of the satellite ground-track over time. The sub-cycle time-interval of Figures 3.4 and 3.5 (7 days) indicates an almost good homogeneity of the Earth coverage by the satellite mission.



## 4 Simulation Procedure

This chapter starts with an overview of gravitational forces acting on a satellite and the time-variable gravity field models used in this study. The important non-gravitational forces are also briefly mentioned. Two tools, an orbit integration software and a quick-look simulation tool, which are employed for simulating the orbits of satellite mission scenarios in the time-variable Earth's gravity forces are introduced. A comparison of the results by the orbit simulation softwares is then given. Moreover, a regularization method in data inversion for gravity solution is introduced in this chapter. The chapter also provides a mathematical overview of Empirical Orthogonal Functions (EOF) analysis together with Kolmogorov-Smirnov test (KS-Test) as a post-processing tool for dealing with white noise. Furthermore, a brief discussion over the use of EOF as a correlation analysis tool for comparison of the input and output of the closed loop simulation of this study is provided. A flowchart of the research approach and main simulation procedures of the following two chapters is shown in Figure 4.1.

### 4.1 Time-variable Gravity Field

The geophysical processes inside the Earth's system lead to the variations of the Earth's gravitational field. Besides these changes, the non-gravitational forces such as atmospheric drag, Sun radiation pressure, Earth albedo, etc. act on the satellite. In this study, the influence of some of the most important gravitational forces caused by mass transports inside the Earth's system is investigated. The main geophysical processes and the important non-gravitational forces, the gravity force by third body (Sun, Moon and planets) and the relativistic effects are discussed here.

#### 4.1.1 Gravitational Forces by Mass Transport inside the Earth's System

In this study, the dominant mass variations of atmosphere, ocean, hydrology, ice and solid Earth (AOHIS) in the Earth system are modeled for the forward simulation environment. The models were compiled at 6 hours intervals (ESA, 2008; Gruber et al., 2011). However, the contributions from the atmosphere, oceans, and tides are tried to be removed from the data using a set of models, leaving all other signals in the gravity solution. Therefore, hydrology, ice and solid Earth signals are the main geophysical signals which alias into the gravity solutions, whereas the aliasing errors from the atmosphere, oceans, and tides are mitigated by the modelling. Here, the combined ocean and atmosphere models (AO) is considered. The combined model is mainly responsible for the so-called *inverted barometer* effect, a terminology used by Doodson (1924) for the first time. Indeed, the mass variation contributions from the atmosphere and the oceans can not be regarded separately. That is because of the dynamic response of the oceans to atmospheric mass changes, where the atmospheric loading is mainly compensated for by the resulting flow in the ocean as it responds to this loading. A low barometer will allow the sea level to rise and a high barometer will tend to depress. Moreover, to estimate ocean tide model error, the difference between two tide models EOT08a (Savcenko and Bosch, 2008) and ocean tide model GOT4.7 (Ray, 2008) is used. The ocean tide error, as a dealiasing product, is considered as the difference between these two ocean tide models (Table 4.1). The error can be also considered as an example of

#### 4 Simulation Procedure

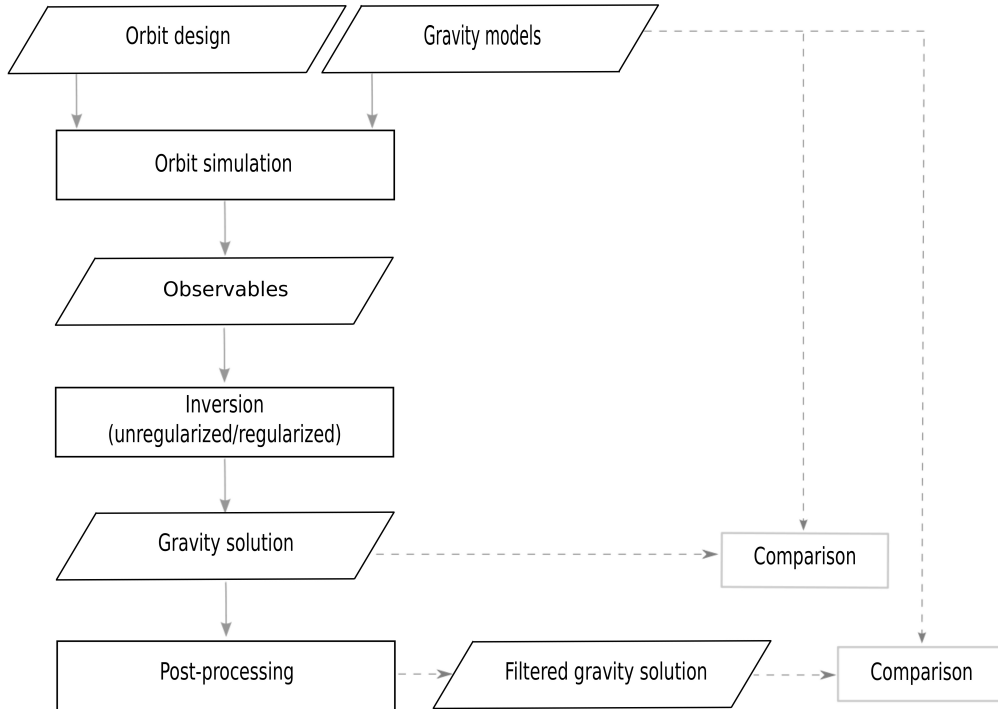


Figure 4.1: Flowchart of simulation procedures of the thesis.

Table 4.1: Model definition AOHIS (Gruber et al., 2011), ocean tide model EOT08a (Savcenko and Bosch, 2008), and ocean tide model GOT4.7 (Ray, 2008) for 1995–2006.

	model
Solid Earth	DEOS Delft University of Technology
Atmosphere	ECMWF ERA-40 re-analysis and ECMWF operational analysis
Ocean	OMCT
Hydrology	PCR-GLOBWB driven with ECMWF meteorological data
Ice	ECMWF Operational Analysis
Ocean Tide error	EOT08a – GOT4.7

colored noise source in the simulation tools.

Figure 4.2 illustrates the magnitude of the individual models and the combination of them (AOHIS) in terms of geoid height rms. For the accuracy estimate of a GRACE-like mission, the rms of geoid height error (here, error: difference between monthly gravity solution and mean of input models) of a reference simulation of a GRACE-like satellite (with altitude of 460 km and microwave K-band intersatellite link) is provided in the figure as well. That shows how a GRACE-like mission deals with the main geophysical signals. For example, the AOHIS combined signal is above the GRACE-like mission accuracy up to around degree 35, while that is around degree 18 for the solid Earth. The figure also shows the dominance of hydrological signals in the models summation (AOHIS). It is important to notice again that the combined ocean and atmosphere models (AO), as the inverse barometer effect, is considered. The effect is indeed responsible for the small magnitude of the signal.

Here, the geophysical models of this study are briefly discussed (ESA, 2008; Gruber et al., 2011).

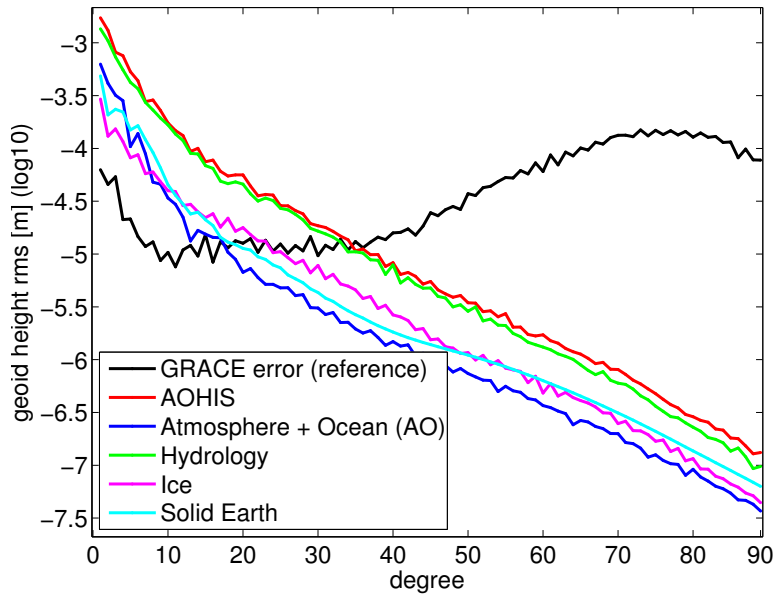


Figure 4.2: Geoid height rms of geophysical signals of Table 4.1. The geoid height error rms of a reference simulation of a GRACE-type mission is shown for comparison.

### Solid Earth

The following three solid Earth contributions to the time-variable gravity field have been provided:

- **Post-Glacial Rebound (PGR) trend coefficients:** One-year time linear change of the Stokes coefficients due to Post-Glacial Rebound is considered in the model. For each coefficient, the linear model is considered as

$$C = C_0 + \dot{C}_{\text{PGR}}(t - t_0)$$

where  $C_0$  is the initial value of the Stokes coefficients (from a priori static gravity field model),  $\dot{C}_{\text{PGR}}$  are the values in PGR-trend coefficient,  $t_0$  is the reference time for the static field and  $t$  is the time of estimation.

- **Sumatra coseismic coefficients:** The change of Stokes coefficients due to the Sumatra earthquake (on 26 December 2004) is considered to be a step function as

$$\begin{aligned} \text{Before earthquake: } C &= C_0 \\ \text{After earthquake: } C &= C_0 + C_{\text{co}} \end{aligned}$$

where  $C_{\text{co}}$  is the coseismic coefficients.

- **Sumatra post-seismic coefficients:** The Stokes coefficients changes over and after a one-year period following the Sumatra earthquake are represented by

$$\begin{aligned} \text{Before the earthquake: } C &= C_0 \\ \text{Till 1 year after the earthquake: } C &= C_0 + \dot{C}_{\text{post}}(t - t_e) \end{aligned}$$

## 4 Simulation Procedure

From 1 year after the earthquake  $C = C_0 + C_{\text{post}}$

where  $C_{\text{post}}$  is the post-seismic coefficients and  $t_e$  is the time of the Sumatra earthquake.  $\dot{C}_{\text{post}}$  is then the coefficients change over time. The post-seismic relaxation is considered to be negligible after one year after the earthquake.

Obviously, the total effect includes all solid Earth contributions from Post-Glacial Rebound, coseismic and post-seismic coefficients.

### Atmosphere

The European Centre for Medium-Range Weather Forecasts (ECMWF) and the US National Centre for Environmental Prediction (NCEP) provide required parameters for modelling atmospheric masses and mass variability such as surface pressure, geopotential height, multi-level temperature and specific humidity on a 6-hourly basis. However, some significant differences between the surface-pressure by both models are reported (ESA, 2008). The ECMWF ERA-40 re-analysis and ECMWF operational analysis without further processing are used as atmospheric raw data sets.

### Ocean

Oceanic mass distributions are represented by ocean bottom pressure which consist of the oceanic and atmospheric column above the observation point at ocean bottom. The ocean model and its underlying physical parameterization is of importance for the gravity solution. In order to determine long-term ocean mass anomalies caused by transient ocean dynamic, the global baroclinic Ocean Model for Circulation and Tides (OMCT) has been used in GRACE data processing as it is also employed in this thesis research for future gravity missions (Thomas, 2002). In the period relevant for this study, the oceanic model has been simulated using the operational ECMWF atmospheric data together with daily discharges from continental hydrology (University of Utrecht), daily discharges from the Greenland ice-sheet by Bristol Glaciology Centre (BGC) and annual ice discharges from Antarctica BGC (ESA, 2008).

### Hydrology

The forward modelling of hydrology with the large-scale PCRaster GLOBal Water Balance model (PCR-GLOBWB, Van Beek and Bierkens (2008)) provides daily fields of terrestrial freshwater storage with a resolution of  $0.5^\circ$  for the period 1957–2006. The water storage in the model is expressed as volume including the following stores of the terrestrial part of the hydrological cycle

- Open freshwater bodies (river stretches and active volumes of lakes and reservoirs)
- Active groundwater storage
- Snow cover
- Interception storage
- Soil moisture

The ground ice, fossil groundwater bodies and inactive lake volumes and salt water intrusions into estuaries or permeable coastal reservoirs or any anthropogenic abstractions or diversions of freshwater are not considered in the model. The model, then, was driven with ECMWF meteorological data for precipitation, air temperature and actual evapotranspiration (ESA, 2008).

## Ice

In cryosphere, models for mass transport should include two main processes (i) surface mass balance (precipitation, melting, refreezing and runoff) and (ii) ice dynamical changes (mainly speed up or slow down of glaciers or ice streams). The Antarctic and Greenland ice sheets store the vast majority of mass in the cryosphere. Here, the output from a high-resolution atmosphere model (Van de Berg et al., 2005) was employed for the calculation of Antarctic surface mass balance, forced at the lateral boundaries by the ERA-40 reanalysis data. For the ice sheets, a time series of mass fluxes has been calculated using ECMWF Operational Analysis for the period of this study. The data are provided on a 5 km polar stereographic grid with 6-hourly time steps and daily time steps respectively for Greenland and Antarctica. Using regional climate models forced by the re-analysis data, the Surface Mass Balance (SMB), comprising accumulation-ablation is calculated. The secular trends in ice dynamics, representing changes which are known from ice height change ( $dh/dt$ ) and Interferometric Synthetic Aperture Radar (InSAR) observations, are then superimposed on the SMB. The ice from non ice-sheet land was treated separately, within the hydrological model (ESA, 2008).

## Ocean Tide

Ocean tides are modeled on a global or regional basis. The recent global tide models include FES2004 (Lyard et al., 2006), GOT00.2 (Ray, 1999), TPXO6.2 (Egbert and Erofeeva, 2002), CSR4 (Eanes, 1994) and NAO.99b (Matsumoto et al., 2000). FES2004 is provided on a 1/8 degree grid, TPXO6.2 on a 1/4 degree grid and the others on 1/2 degree grids. On the other hand, regional models may have resolutions down to 5 km. Each of these models assimilate much of the available tidal data from tide gauges, bottom pressure records and satellite altimetry. Using onshore gravimetric (Bos et al., 2002) and GPS data (Allinson, 2004; Schenewerk et al., 2001), independent assessments of relative and absolute model accuracy have been performed to determine variations due to ocean tide loading. Due to the spatially extensive permanent GPS network in operation, GPS is a particularly promising approach (Thomas et al., 2007).

For the eight major constituents of tide models, K1, K2, M2, N2, O1, P1, Q1 and S2, the ocean tide models are provided as spherical harmonic expansions of amplitudes and phases. Schrama et al. (2007) provides methods to convert these amplitudes to geopotential time varying Stokes coefficients and a time averaged estimate for the power in terms of geoid (ESA, 2008).

Indeed, with perfect models for ocean tides, the temporal aliasing problem in space-borne gravimetry is largely reduced. However, the improvement of tidal models is the subject of future research (Savcenko and Bosch, 2008). It is expected that the tidal aliasing effects will be reduced with the improvement of the tidal models. However, practical considerations require other solutions. With the availability of high-precision satellite radar altimeter observations in the past, it will be a challenge to improve tidal models in the near future to such an extent that the associated gravity field recovery error level is below the recovery error based on the predicted observation precision for future ll-SST ranging systems (Visser et al., 2010). This study employs the ocean tidal error as the difference of two ocean tide models, EOT08a (Savcenko and Bosch, 2008) and GOT4.7 (Ray, 2008), up to spherical harmonic degree and order 50 for its largest effects. The difference is introduced as a dealiasing product where the aim is to investigate the effect of tidal aliasing error as one of the most important error sources in the gravity recovery by satellite missions. The error can be also considered as an example of colored noise source in the simulation tools.

### 4.1.2 Gravitational Forces by Third Body

In addition to the Earth's gravitational force, the satellite orbit is affected by third-body tidal forces (mainly from the Sun, the Moon, and the other planets). The tidal forces on the satellite orbit by the third bodies can be calculated from the positions of the third bodies, given in the ephemerides DE 405 by NASA-JPL (Standish, 1998). The effect of direct tidal forces on the satellite orbit is not included in this study.

### 4.1.3 Non-gravitational Forces

In addition to the gravitational forces due to the Earth and direct tidal forces by the third bodies, the non-gravitational forces influence the LEO satellite. The non-gravitational forces must be modeled for precise orbit determination. Although the effects of non-gravitational forces are not included in the closed loop simulation procedure of this study, they are listed and briefly discussed here.

#### Atmospheric Drag

Atmospheric drag is the most dominant non-gravitational perturbation for the low-orbiting satellites. The perturbation force is caused by the interaction between surface of the satellite and the atmosphere particles. The force depends on (i) satellite geometry, (ii) satellite velocity, (iii) satellite orientation with respect to the flow, and (iv) the density, temperature and composition of the atmospheric gases (Seeber, 2003). Clearly, the effect of atmosphere drag decreases rapidly with increasing height. The perturbing forces on the satellite may cause accelerations varying between  $10^{-3}$  and  $10^{-9}$  m/s<sup>2</sup> (Seeber, 2003).

#### Solar Radiation Pressure

The solar particle radiation is proportional to the effective satellite surface area, the reflectivity of the satellite surface and the solar flux. It is also inversely proportional to the square of the distance between the satellite and the Sun. The direct radiation pressure is mainly effective in the direction of the satellite along-track motion. The acceleration can reach in the order of  $10^{-7}$  m/s<sup>2</sup> (Seeber, 2003).

#### Earth Albedo

The Earth albedo is the ratio between the reflected radiation by the Earth and the incoming radiation to the Earth. The Earth albedo makes a small pressure on the satellite. Due to varying distribution of land, sea and clouds, the effect is very difficult to model, but in most cases it is less than 10% of the direct radiation pressure by the Sun (Seeber, 2003). Obviously, the effect largely depends on the altitude of the satellite. For example, for the GPS satellites, the radiation pressure is very small and can be neglected, while for near-Earth satellites, the force should be considered (Seeber, 2003).

#### Other Forces

Some other non-gravitational perturbation forces are (Seeber, 2003)

- friction caused by charged particles in the upper atmosphere,
- thermal radiation of the satellite,
- heating effects at shadow boundaries,

- electromagnetic interaction in the geomagnetic field,
- the inter-planetary dust effect

Due to the very small effects of these forces on the satellite, they are usually considered for very precise orbital analysis only.

#### 4.1.4 Relativistic Effects

If the satellite travels at a speed that is a substantial fraction of the speed of light, relativistic effects (provided by Albert Einstein as special relativity theory) must also be considered. The effects are, however, very small and usually taken in consideration for very precise orbit determination only (Grafarend, 1991). The relativistic effects include the mass increase, length contraction and time dilation. McCarthy and Petit (2004) provides the relativistic correction to the acceleration of a satellite. However, the effect is not considered in the satellite orbit and gravity recovery simulations of this study.

## 4.2 Orbit Simulation

The gravity field seen by different satellite orbit configurations and formations can be estimated via a variety of methods while each method has its own advantages and disadvantages. In this study, a quick-look simulation software has been employed as a gravity recovery simulation tool. The tool avoids the orbit integration method for the determination of satellite orbits and therefore provides a fast approach for comparing the results of different formation scenarios. Instead, the quick-look tool assumes a nominal orbit during the satellite mission journey, i.e. the gravity field is evaluated along a constant repeat orbit. As a result of the assumption, the gravity field solutions are only approximations of recovered solutions from more accurate approaches. Nevertheless, this research study shows that the approximations by the quick-look tool provide gravity solutions which are in very high agreement with the results from the satellite orbit integration approach where the influence of the gravity field on the orbit is considered. The satellite orbit integration approach evaluates the gravity field along an orbit which is consistent with the gravity field. This approach, therefore, provides a more realistic approximation of gravity recovery when it is compared with the results of quick-look simulation tool. However, the orbit integration method requires much longer computation time which is a drawback for implementing a multitude of satellite orbit scenarios. In the following sections, these two orbit simulation tools are briefly discussed. The recovery of gravity field from a satellite mission scenario by these two simulation tools are also compared.

Satellite orbit integration can be performed either analytically or numerically. However, some problems such as the algebraic complexity of the perturbation forces and the deficiency of their modelling make the analytical methods difficult to implement (Seeber, 2003). The numerical method, on the other hand, is characterized by its relative simplicity. It determines the orbit by calculating the state of the satellite (position and velocity vectors) for different epochs. Seeber (2003) gives the solution of the equation of motion including all perturbations for a step-wise integration. The perturbed satellite motion is formulated through the following equation

$$\ddot{\mathbf{r}} = -\frac{GM}{r^3}\mathbf{r} + \mathbf{F}_s \quad (4.3)$$

where  $\mathbf{r}$  is the inertial position vector,  $\ddot{\mathbf{r}}$  is the inertial acceleration vector, and  $\mathbf{F}_s$  are the disturbing forces per mass acting on the satellite.

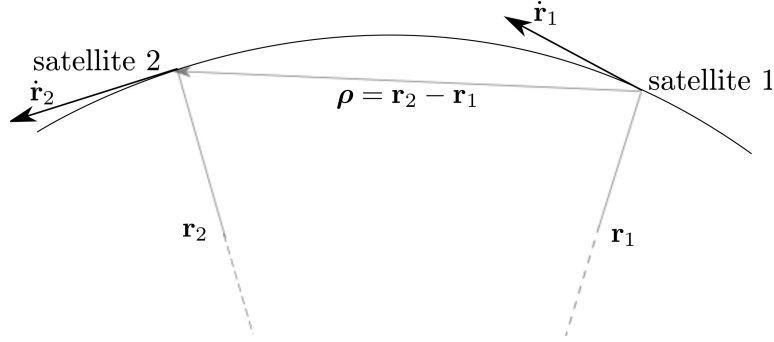


Figure 4.3: Baseline vector  $\boldsymbol{\rho}$  between two satellites.

Equation (4.3) can be re-written in the form of two first order differential equations (Seeber, 2003)

$$\dot{\mathbf{r}} = \mathbf{v}, \quad \dot{\mathbf{v}} = \mathbf{F}_s - \frac{GM}{r^3} \mathbf{r} \quad (4.4)$$

with vector components of

$$\begin{aligned} \dot{x} &= v_x, & \dot{v}_x &= F_{sx} - \frac{GM}{r^3} x \\ \dot{y} &= v_y, & \dot{v}_y &= F_{sy} - \frac{GM}{r^3} y \\ \dot{z} &= v_z, & \dot{v}_z &= F_{sz} - \frac{GM}{r^3} z \end{aligned}$$

**Satellite to Satellite Tracking** For the Satellite to Satellite Tracking (SST) formation flights and through the calculated values of positions and velocities of each satellite at different epochs by the orbit integration method, the range,  $\rho$ , and range rate,  $\dot{\rho}$ , between two satellites can be computed. The baseline vector between two satellites is calculated by  $\boldsymbol{\rho} = \mathbf{r}_2 - \mathbf{r}_1$  (Figure 4.3). Then, the baseline unit vector between the satellites  $\mathbf{e}_{12}$  is

$$\mathbf{e}_{12} = \frac{\boldsymbol{\rho}}{\rho} \quad (4.5)$$

The baseline vector is the scalar range times the unit vector in the direction of the baseline:

$$\boldsymbol{\rho} = \rho \mathbf{e}_{12} \Rightarrow \rho = \boldsymbol{\rho} \cdot \mathbf{e}_{12} \quad (4.6)$$

The range rate is therefore computed by derivation of the vectorial range:

$$\left. \begin{aligned} \dot{\boldsymbol{\rho}} &= \dot{\rho} \mathbf{e}_{12} + \rho \dot{\mathbf{e}}_{12} \\ \mathbf{e}_{12} \cdot \mathbf{e}_{12} &= 1 \Rightarrow \mathbf{e}_{12} \cdot \dot{\mathbf{e}}_{12} = 0 \end{aligned} \right\} \Rightarrow \dot{\rho} = \dot{\boldsymbol{\rho}} \cdot \mathbf{e}_{12} \quad (4.7)$$

Finally, the range acceleration can be computed by further time differentiation

$$\begin{aligned} \ddot{\rho} &= \ddot{\boldsymbol{\rho}} \cdot \mathbf{e}_{12} + \dot{\boldsymbol{\rho}} \cdot \dot{\mathbf{e}}_{12} \\ &= \ddot{\boldsymbol{\rho}} \cdot \mathbf{e}_{12} + \dot{\boldsymbol{\rho}} \cdot \frac{1}{\rho} (\dot{\boldsymbol{\rho}} - \dot{\rho} \mathbf{e}_{12}) \\ &= \ddot{\boldsymbol{\rho}} \cdot \mathbf{e}_{12} + \frac{1}{\rho} (\dot{\boldsymbol{\rho}} \cdot \dot{\boldsymbol{\rho}} - \dot{\rho}^2) \end{aligned} \quad (4.8)$$

Inserting Newton's equations of motion in differential mode in terms of gradient of Earth's

potential at the positions of satellites 1 and 2 at time epoch  $t$ , i.e.  $\ddot{\boldsymbol{\rho}} = \ddot{\mathbf{r}}_2 - \ddot{\mathbf{r}}_1 = \nabla V(\mathbf{r}_2(t)) - \nabla V(\mathbf{r}_1(t))$ , into the Equation (4.8), the range acceleration,  $\ddot{\rho}$ , between two satellites is therefore calculated from the following equation (Seeber, 2003)

$$\ddot{\rho} = \mathbf{e}_{12} \cdot (\nabla V(\mathbf{r}_2) - \nabla V(\mathbf{r}_1)) + \frac{1}{\rho} (\dot{\boldsymbol{\rho}} \cdot \dot{\boldsymbol{\rho}} - \dot{\rho}^2) \quad (4.9)$$

Finally, the observation equation is built up by rearranging the Equation (4.9)

$$\ddot{\rho} - \frac{1}{\rho} (\dot{\boldsymbol{\rho}} \cdot \dot{\boldsymbol{\rho}} - \dot{\rho}^2) = \mathbf{e}_{12} \cdot (\nabla V(\mathbf{r}_2) - \nabla V(\mathbf{r}_1)) \quad (4.10)$$

### 4.2.1 Realistic Orbit

The positions,  $\mathbf{r}$ , and velocities,  $\mathbf{v}$ , of the satellite at desired epochs can be calculated by suitable methods of numerical orbit integration in the closed loop simulation. Concerning the numerical method, Seeber (2003) provides several approaches for orbit integration. Depending on the applied algorithm, the approaches can be divided into two main categories (i) *single-step* and (ii) *multi-step* methods. The methods depend on the number of points which are used by proceeding to the next point. A well-known single-step numerical method is the *Runge-Kutta method* which employs a Taylor series of a certain order as an extrapolation function. In this procedure, only the last integration step is used. That means the knowledge of the history of the function is neglected. On the other hand, the multi-step methods (also called *predictor-corrector methods*) use the history knowledge of the function which is aimed to be integrated. The multi-step methods are more often used in satellite geodesy. In this method, first the satellite position is predicted with a certain algorithm and then will be corrected. A predicted value  $X_{n+1}$  is calculated from  $X_n$  and  $X_{n-i}$  with  $i = 1, 2, \dots, n$ . The value is then substituted in the differential equation of the process which provides a corrected value of  $X_{n+1}$  with  $\check{X}_{n+1}$ . The process, then, is iterated until the result does not change (Seeber, 2003). Among many multi-step integration methods, a variable order *Adams-Bashforth-Moulton* procedure, implemented as MATLAB function *ode113*, has been employed in this study. A description of the method can be found in Shampine and Gordon (1975).

The left side of the Equation (4.10) gives the simulation observables at the epoch  $t$  and can be computed through the calculation of range, range rate and range acceleration values, yielded from the orbit integration. In this thesis, the range and range rate values are directly calculated from the positions and velocities of the two satellites, while the range acceleration values come from the calculation of gradient of Earth's potential at the positions of the satellite in the realistic orbit over time. It is also important to mention that in the orbit integration approach, the initial values of satellites positions and velocities, indicated by the Keplerian elements, are transferred to osculating elements, i.e. the effect of the Earth's flattening is considered for adjusting the initial satellite states. The osculating orbit means an unperturbed Keplerian orbit with initial parameters (position and velocity vectors) coincide with the true perturbed state vectors at a certain epoch. Therefore, the true satellite orbit can be considered as successive osculating orbits with osculating orbital parameters. Schaub and Junkins (2003) provide a discussion over this subject and bring a set of formulas for the transformation.

In order to investigate the time-variable gravity recovery, the static field is subtracted from the total retrieved field. The result, therefore, includes the spatial aliasing of the static field by the particular sampling of the formation flight. A flowchart of the realistic orbit approach is shown in Figure 4.4.

## 4 Simulation Procedure

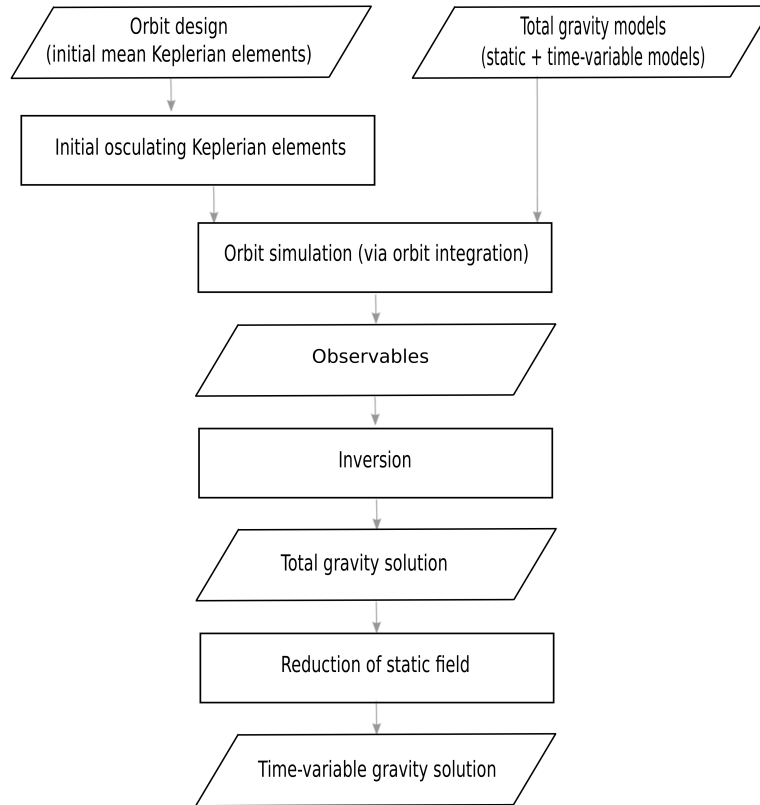


Figure 4.4: Flowchart of the realistic orbit approach of this thesis.

### 4.2.2 Nominal Orbit

The quick-look simulation software of this thesis has been developed at Institute of Geodesy, University of Stuttgart. The tool is employed for time-variable gravity field aliasing analysis from ll-SST missions and assumes a constant inclination angle and repeat mode  $\beta/\alpha$  nominal orbit of the satellite formations within the time interval of the gravity recoveries (i.e. only  $J_2$  effect consideration). The software makes use of the observation equation for range acceleration of Equation (4.10). The nominal relative motion of both satellites within the formation is described by means of the homogeneous solution of the Hill's equations (3.16), where the formations are obtained by different initial values for the satellites' relative state vectors  $(\rho_0, \dot{\rho}_0)$  (Sharifi et al., 2007).

The right side of Equation (4.10) is calculated at the positions of both satellites in the nominal orbit for the time interval of interest. The time-variable potential of the Earth at the positions of the satellites is calculated by the provided time-variable gravity field models at those epochs. The calculated values for the right side of the equation are set to the left side as the observables at those epochs. Then, the gravitational potential in terms of spherical harmonics coefficients is estimated through the system of equations for that time interval (gravity solution). Although the assumption of keeping the satellites in a perfect nominal orbit is not realistic, the tool provides a quick comparison of gravity recoveries of different formations. That is because the quick-look tool avoids orbit integration which is a time-consuming process. Obviously, a more precise and realistic study of the gravity recoveries can be later performed in more detail by more realistic tools where the observations can be rather generated directly from the orbit by evaluating the left side of Equation (4.10).

Figure 4.5 illustrates a flowchart of the orbit simulation and gravity recovery by the nominal orbit approach.

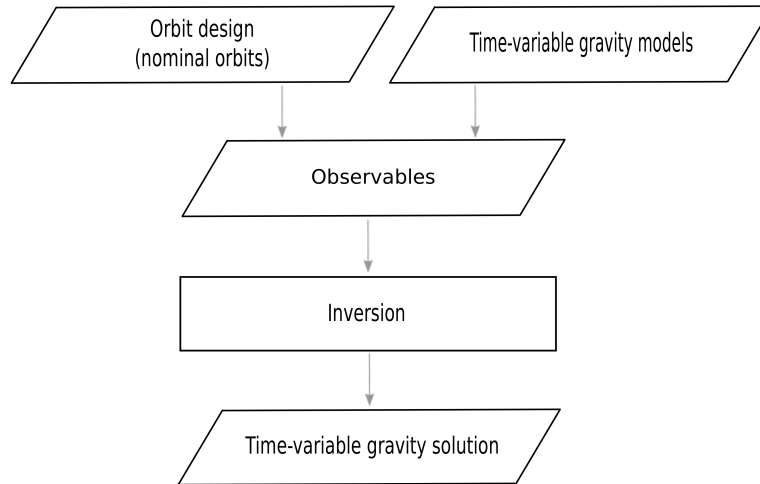


Figure 4.5: Flowchart of the nominal orbit approach by quick-look simulation tool of this thesis.

### 4.2.3 Validation

In this study, the quick-look tool is utilized for assessing the quality of the recoveries of different orbit configurations and formation flights. However, the validation of the results from the quick-look simulation tool by the results from a more realistic tool is a crucial issue. For this reason, the time-variable gravity solutions of the nominal orbit approach with its quick-look tool for orbit design (Figure 4.5) and the realistic orbit approach with orbit integration tool (Figure 4.4) are compared. From the comparison analysis of some examples, and despite the methodological differences between the two procedures, very strong correlation between the results of two approaches has been seen. Figures 4.6 and 4.7 illustrate two examples (7 and 32 days gravity solutions) of a near-polar GRACE-like mission at the altitude of 333.8 km. The figures imply that the effect of satellite orbit fluctuations in the Earth's time-variable gravity field of the orbit integration approach is not significant.

## 4.3 Gravity Field Estimation

### 4.3.1 Least Squares Estimation

To recover the time-variable gravitational field of the Earth, the satellite missions' observations should be associated to the unknown parameters of the gravity field. The observables of the ll-SST orbit simulation tools are set to the fundamental least squares estimation (Koch, 1999; Grafarend, 2012)

$$E\{y\} = Ax, \quad D\{y\} = \sigma^2 Q = P^{-1} \quad (4.11)$$

where

$y$  is  $m \times 1$  vector of observations

$A$  is  $m \times n$  design matrix

$x$  is  $n \times 1$  vector of unknowns

$\sigma^2$  is the scalar variance component

$Q$  is  $m \times m$  covariance matrix of observations

#### 4 Simulation Procedure

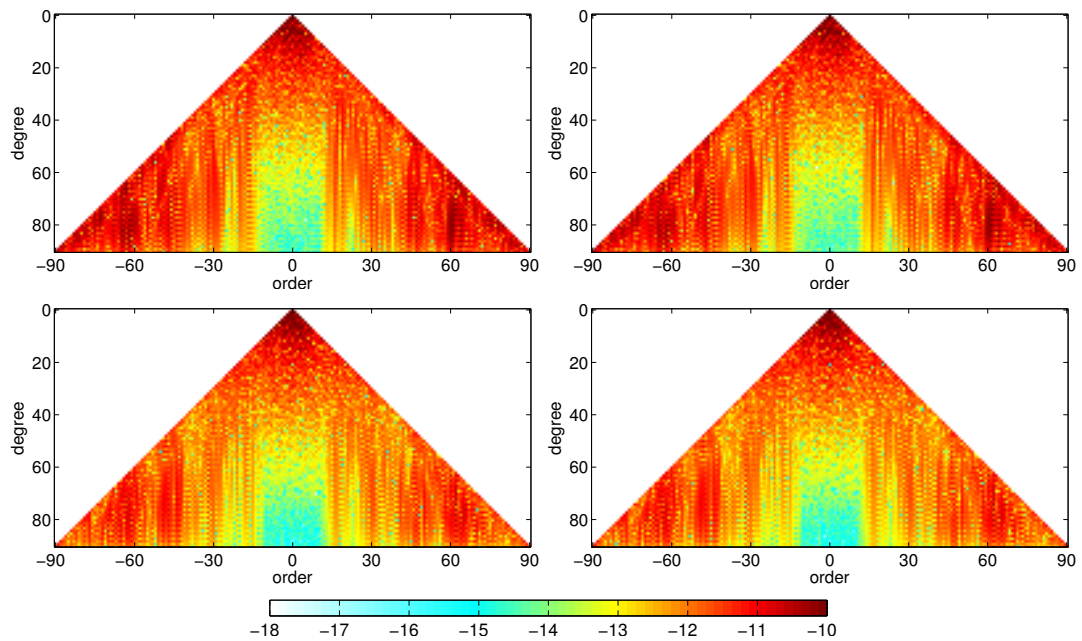


Figure 4.6: Logarithmic scale triangle plots of spherical harmonics of recovered gravity field by orbit integration approach (left) and quick-look tool (right) for 7-day (top) and 32-day (bottom) recoveries of near-polar GRACE-like mission at the altitude of 333.8 km.

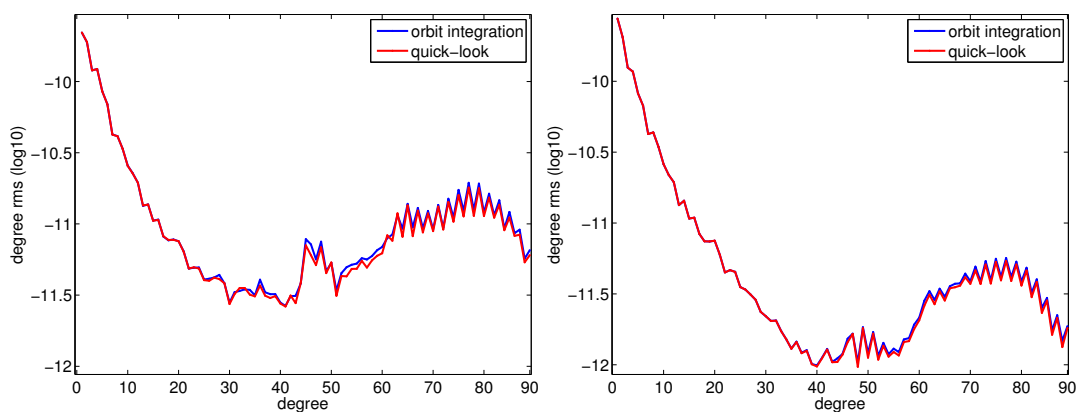


Figure 4.7: Degree rms plots of recovered gravity field by orbit integration approach and quick-look tool for 7-day (left) and 32-day (right) recoveries of near-polar GRACE-like mission at the altitude of 333.8 km.

The Equation (4.11) is usually written as an observation equation

$$y + e = Ax \quad (4.12)$$

with  $E\{e\} = 0$ ,  $D\{e\} = D\{y\} = \sigma^2 Q = P^{-1}$ . The vector  $e$  is the  $m \times 1$  observation errors vector. The vector of unknowns is then estimated by minimizing the squared residuals

$$x : \min \|Ax - y\|_P^2 \quad (4.13)$$

which is obtained by the unbiased least squares estimator

$$\hat{x} = (A^T P A)^{-1} A^T P y \quad (4.14)$$

Then, the covariance matrix of unknowns reads

$$Q_{\hat{x}} = (A^T P A)^{-1} \quad (4.15)$$

### 4.3.2 Regularization

In order to stabilize an ill-posed system of normal equations, Koch and Kusche (2002) introduces a Bayesian-type regularization by adding prior stochastic information (e.g from the geophysical models) about the unknown parameters as constraint. The prior information is usually stored in a positive definite diagonal matrix.

The regularization methods use the existing information from some measurement sources as stochastic constraints to deal with both the white and colored noise. Since the launch of gravity satellite missions, several publications have discussed the regularization methods (e.g. Xu, 1992; Bouman and Koop, 1998; Koch and Kusche, 2002; Kusche, 2007). The regularization methods, indeed, consider the errors of the signal or use information about correlations in the spectral domain in order to reduce the noise level in the output signal. The filtering process is mainly performed by constraining the noisy signal to tend to a desired output signal, which can be done in the spatial or spectral domain. Here, a brief discussion over one method is introduced.

#### A Kaula-type Rule for Constraining the Coefficients from Gravity Satellite Missions

Many geodetic problems, especially the estimation of gravity field, are ill-posed problems (Xu, 1992; Bouman and Koop, 1998). That is due to a bad condition of the normal matrix

$$N = A^T P A \quad (4.16)$$

The following characteristics of gravity data from satellite missions can cause bad conditioning of the normal matrix

- irregular data distribution due to polar gaps or non-continuous data tracking
- insufficient information about the gravity field in the observable itself
- downward continuation
- bad condition due to stochastic model (e.g. the instrument is unable to measure in the whole spectral domain)

An ill-conditioned matrix prevents a stable solution of the minimization problem, i.e. the normal matrix has not enough information for inversion. Bouman and Koop (1998), Xu

#### 4 Simulation Procedure

(1992) and Koch and Kusche (2002) introduce a method to regularize the ill-posed system of normal equations by adding prior information about the unknown parameters. Such data has then the expectation and dispersion of

$$E\{x_0\} = x, \quad D\{x_0\} = \sigma_K^2 K = P_K^{-1} \quad (4.17)$$

where  $x_0$  is a vector with prior information,  $K$  is appropriate covariance and  $\sigma_K$  is unknown variance component. Therefore, the minimization problem changes to

$$x : \min \|Ax - y\|_P^2 + \lambda \|x - x_0\|_{P_K}^2 \quad (4.18)$$

with  $\lambda$  as a positive real number, the ratio between the variance components of the observation groups

$$\lambda = \frac{\sigma^2}{\sigma_K^2} \quad (4.19)$$

The unknown parameters are estimated under the constraint that the squared residual between the *a priori* values and the estimated parameters is minimal. The observations  $x_0$  are commonly assumed to be zero with their appropriate weight matrix  $P_K$  to be a positive definite diagonal matrix. The elements of such weight matrix are inversely proportional to a degree variance model (Koch and Kusche, 2002). Finally, considering this degree variance model as independent observation, the estimates of unknown parameters would be

$$\hat{x} = \left( A^T P A + \lambda P_K \right)^{-1} \left( A^T P y + I^T P_K x_0 \right) \quad (4.20)$$

and covariance matrix of unknowns is

$$Q_{\hat{x}} = \left( A^T P A + \lambda P_K \right)^{-1} = N^{-1} \quad (4.21)$$

Kaula (1966) provides a method to improve the condition for static gravity field determinations by using Kaula rule as a priori degree variance model. The Kaula rule constrains the coefficients to attenuate with increasing degree according to a power law

$$\sigma_l^2 = \frac{10^{-10}}{l^4} (2l + 1) \quad (4.22)$$

Therefore, the regularization matrix (a prior variance matrix)  $K$  is filled with elements from the signal variance model by Kaula's rule, although Sneeuw (2000) shows that the approach may lead to a too optimistic error estimate, where the rule is also defined for the static gravity field only. However, the power law behavior of the Kaula's rule allows a simple estimation of a fitting power law, i.e. a degree variance model, for other kinds of spherical harmonic coefficients. The basic equation for such a power law reads as (Lorenz, 2009)

$$\sigma_l^2 = 10^a l^b \quad (4.23)$$

with  $\sigma_l^2$  as the signal degree variance and  $a$  and  $b$  the unknown parameters of power law. In a log-log-graph, the power law is transformed into

$$\log(\sigma_l^2) = a + b \log(l) \quad (4.24)$$

The Equation (4.24) shows a straight line in a log-log-graph and can be employed to fit a

power law to the time-variable gravity field. The unknown parameters  $a$  and  $b$  of the power law are estimated by a least squares estimation

$$y = Ax + e \quad (4.25)$$

with

vector of observations  $y = \log(\sigma_l^2)$ ,

design matrix  $A = [A_l] = [1 \ \log(l)]$ ,  $l = 2, \dots, L_{\max}$ ,

unknown parameters of the power law  $x = [a \ b]$ , and

residuals  $e$

Therefore, the unknown parameters of the power law are obtained by

$$\hat{x} = (A^T A)^{-1} A^T y \quad (4.26)$$

In this study, the signal variance of the combined input model AOHIS (see Figure 4.2) is utilized to estimate the unknown parameters,  $a$  and  $b$ , of the power law equation (4.24), where they are used for filling the regularization matrix  $K$  (Lorenz, 2009).

## 4.4 Empirical Orthogonal Functions (EOF)

Several studies (e.g. Rangelova et al., 2007; Wouters and Schrama, 2007) have employed *Principal Component Analysis (PCA)* technique, or alternatively EOF analysis technique, to analyze data from GRACE mission. Generally, EOF analysis is used for capturing the dominant modes of a time series of data in spatial and temporal domains. Furthermore, the EOF analysis technique together with a white noise test can be employed for filtering white noise. The technique can also be utilized as a correlation analysis tool when a comparison between different fields or data sources is of interest.

### 4.4.1 Basic EOF Theory

In general, EOF analysis is a technique to study the spatial and temporal variability of datasets which separates the directions of the largest variances from each other. The technique uses the principal directions to transform the multi-directional dataset to a reduced subspace with a lower number of dimensions, while the loss of information by this transformation is minimal.

The EOFs and PCs of a general real-valued, scalar and homogeneously dimensioned dataset  $Z$  can be obtained by *Singular Value Decomposition (SVD)* as a convenient procedure

$$Z = UDV^T \quad (4.27a)$$

$$z(t, x) = \sum_{j=1}^{\rho} u_j(t) \lambda_j v_j(x) \quad (4.27b)$$

The dataset  $Z$  with elements  $z(t, x) : x = 1, \dots, p; t = 1, \dots, n$  ( $n$  observations of  $p$  variables) has a set of dominant directions of variance in Euclidean space. The dataset can be a function

#### 4 Simulation Procedure

of any two variables, e.g. space, time, pressure, temperature, SH coefficients, etc., arranged in rows and columns of a data matrix. In many literatures, the column vectors of matrix  $U$  are called Principal Components (PCs) and the column vectors of matrix  $V$  are called Empirical Orthogonal Functions (EOFs). The diagonal matrix  $D$  contains the singular values, where the square root of the eigenvalues  $\lambda_j$  of the covariance matrix  $Z^T Z$  are the elements of the matrix. The matrix  $D$  represents the scatter of the dataset  $Z$  along the associated eigenvector  $v_j$ . The energy percentage of each mode of the total variance can be shown as

$$\frac{\text{Variance of the } j\text{-th mode}}{\text{Total variance}} = \frac{\lambda_j}{\sum_{j=1}^{\rho} \lambda_j} = \frac{D_{jj}^2}{\sum_{j=1}^{\rho} D_{jj}^2} \quad (4.28)$$

Generally, the first few modes contribute to the most power in the dataset.

In Preisendorfer (1988), the dominant directions of variance is determined by finding the eigenvectors  $e_j$  of the covariance matrix of the dataset  $Z^T Z$  which form an orthonormal basis for the data space

$$Z = AE^T \quad (4.29a)$$

$$z(t, x) = \sum_{j=1}^{\rho} a_j(t) e_j(x) \quad (4.29b)$$

where  $a_j(t)$  is a temporal weight to the contribution of the eigenvector  $e_j$ . The weights,  $a_j(t)$ , are uncorrelated, and variance of the weights is equal to the variance of the data along the direction of the associated eigenvector  $e_j$ . The variables  $a_j$  and  $e_j$  respectively refer to the  $j$ th principal component and EOF mode. The maximum number of modes is denoted as  $\rho$  and equals  $\min[n, p]$ .

#### 4.4.2 Selection Rules

Several selection rules have been introduced to chose the modes for the reconstruction of data. Two of the most used selection rules are *Rule N* and *Kolmogorov-Smirnov Test (KS-Test)* (Preisendorfer, 1988). Rule N method selects the dominant leading modes by keeping the modes with an associated variance larger than a certain threshold in the data reconstruction. The KS-Test method is based on the temporal evolution of the principal components. The test is briefly discussed here.

#### Kolmogorov-Smirnov Test (KS-Test)

In statistics, the Kolmogorov-Smirnov Test (KS-Test) is a nonparametric test for the equality of continuous, one-dimensional probability distributions that can be used to compare a sample with a reference probability distribution in one-sample KS-Test or to compare two samples in two-sample KS-Test (Massey, 1951; Boes et al., 1974).

In this thesis, the KS-Test has been used as a tool of white noise detection by analysis of temporal evolution and property of principal components. The test uses this property by retaining or rejecting the EOF modes in the data reconstruction (Preisendorfer, 1988). The power spectral density (PSD) of each principal component  $u_j(t)$  is calculated through the Fourier transform, and is then tested for white noise spectrum. The KS-Test compares the cumulative distribution function (CDF) of the PSD of the principal components with the CDF of the spectrum of a random white noise process. If the maximum value  $D_{\max}$  of

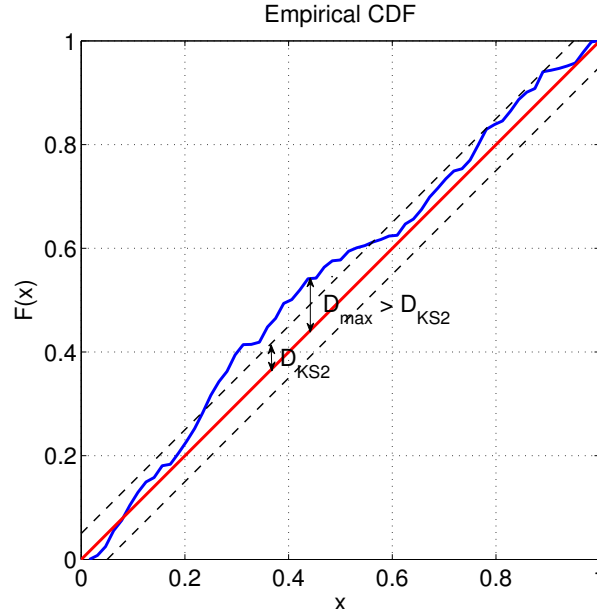


Figure 4.8: Principle of Rule KS2: If the maximum difference  $D_{\max}$  between the cumulative distribution function (CDF) of the power spectrum of the principal component  $a_j$  (blue) and a random white noise (red) is larger than a critical value  $D_{KS2}$ , the principal component is assumed as a signal and kept for data reconstruction.

the absolute difference between these two CDFs is less than a critical value  $D_{KS2}$  (depends on the significance level  $\alpha$  and the number of samples), the test hypothesis is accepted, i.e. the principal component  $u_j$  is considered as a white noise and thrown away. Otherwise, the hypothesis is rejected. That means that the principal component is kept for the data reconstruction (see Preisendorfer, 1988). Figure 4.8 shows the principle of the KS-Test rule.

#### 4.4.3 EOF Analysis + KS-Test as a White Noise Filtering Tool

Dealing with noise is one of the most challenging issue when we look for higher quality of gravity recovery. The noise can have different sources. Two of the most important noise sources are (i) sampling error which is caused by formations architecture (for example the North-South stripes in GRACE recovery) and (ii) the sensor noise. Several filter strategies have been suggested to deal with these noise. Wouters and Schrama (2007) proposes a filter based on EOF analysis in combination with KS-Test in the spectral domain (spherical harmonics) for white noise filtering. Furthermore, Iran Pour and Sneeuw (2012) introduce a filter operator based on the work by Wouters and Schrama (2007).

In Iran Pour and Sneeuw (2012), the EOF reconstruction plus KS-Test filtering is substituted by its equivalent formula  $Z' = ULDV^T$ , where  $L$  is a diagonal matrix with 0 diagonal elements when the modes pass the KS-Test (noise) and 1 when they do not (signals). Inserting  $U^T U = I$  (identity matrix), the formula can be rewritten as

$$Z' = ULU^T UDV^T \quad (4.30)$$

Therefore, the filtered data matrix  $Z'$  is defined as

$$Z' = ULU^T Z = F_u Z \quad (4.31)$$

#### 4 Simulation Procedure

where  $F_u$  is called *left filter operator*

$$F_u = U L U^\top \quad (4.32)$$

In a similar way, the *right filter operator*  $F_v = V L V^\top$  can be employed for data filtering purpose as  $Z' = Z F_v$ .

Consequently, through the model for left filter operator, the filtered degree rms can be calculated by error propagation as

$$Q_{Z'} = F_u Q_Z F_u^\top \quad (4.33)$$

In Wouters and Schrama (2007), data are sorted in an order-wise way to remove the correlation between the spherical harmonics as a function of degree (Swenson and Wahr, 2006). This means that the order of each data matrix is kept fixed. Then, the EOF analysis is separately done on  $C_{lm}$  and  $S_{lm}$  coefficients matrices as the data matrices. As an example, the following matrix shows the time series of the  $C_{lm}$  coefficients for the specific order of  $m$ , with SH degrees  $l = m, \dots, l_{\max}$  for a time series of  $t = [t_1, \dots, t_n]$ .

$$C_m = \begin{pmatrix} C_{mm}(t_1) & C_{mm}(t_2) & \cdots & C_{mm}(t_n) \\ C_{m+1,m}(t_1) & C_{m+1,m}(t_2) & \cdots & C_{m+1,m}(t_n) \\ \vdots & \vdots & \ddots & \vdots \\ C_{l_{\max}m}(t_1) & C_{l_{\max}m}(t_2) & \cdots & C_{l_{\max}m}(t_n) \end{pmatrix} \quad (4.34)$$

#### 4.4.4 EOF Analysis as a Correlation Analysis Tool

EOF analysis can be employed as a correlation analysis tool when two datasets are compared. For example, the analysis can be used for a closed loop simulation, when the quality of the simulation output versus the simulation input models is investigated.

Considering two sets of data  $Z_1$  and  $Z_2$ , the SVD decomposition for the datasets would be

$$Z_1 = U_1 D_1 V_1^\top \quad (4.35a)$$

$$Z_2 = U_2 D_2 V_2^\top \quad (4.35b)$$

Therefore, the correlation analysis can be done by the investigation of correlation between every principal component (temporal mode) of one field and the principal components of the other field through

$$K_{\text{corr}} = U_1^\top U_2 \quad (4.36)$$

This thesis research uses the correlation analysis tool for investigation of correlation between temporal modes of simulation input combined model (AOHIS) and the temporal modes of gravity solutions from different satellite configurations. The tool can be employed as a measure for investigating how satellite configurations recover the input gravity field, in particular for specific geophysical features such as seasonal signature.

# 5 Orbit Design and Formation Flight Mission Scenarios

This chapter provides a short discussion over satellite orbit design for future satellite mission scenarios. The Earth coverage by satellite ground-tracks of different single pair inline missions and the scheme design of alternative formations and dual pairs scenarios are briefly discussed.

## 5.1 Mission Scenarios' Design Concerns

In theory, one can think of every orbit configuration and formation flight with different number of satellites for future gravity satellite mission. However, the technical challenges and financial issues with their implementation limit the search space for finding the optimal missions. The limitation includes the number of satellites in a mission, mission altitude, tracking technology, mission stability, etc.. These factors are considered in the mission search space definition of this thesis.

It is expected that the homogeneity level of ground-track pattern of a satellite mission has influence on quality of the gravity recovery. Moreover, the sensitivity to short wavelength phenomena in gravity field is largely affected by mission height. Therefore, the effect of an orbit configuration, defined by number of satellite mission revolutions ( $\beta$ ) in its repeat period ( $\alpha$ ) and its altitude ( $h$ ) is of great interest for investigation. The influence of the ground-track evolution pattern on the gravity recovery can also be described by the *sub-cycle* concept which is an indicator of minimum gap size reduction and homogeneity of the Earth coverage by the mission. If the correlation between the gap evolution of satellite coverage (evolution of ground-track pattern) and the gravity recoveries is meaningful, then one task would be to search for the orbit configurations by more homogeneous coverage of the Earth. It can also mean that for different configurations, at one point of time (in nodal days), the space domain is quite homogeneously sampled which is good enough for recovery of the gravity field. This time interval then establishes the temporal resolution of the recovery, whereas the level of homogeneity defines the spatial resolution.

The orbit design of this study includes (i) near-polar inline (GRACE-like) missions of different repeat orbits ( $\beta/\alpha$ ) for the global coverage, (ii) alternative formation types and (iii) two pairs of inline missions with different inclination angles. The quality of gravity solutions of those mission scenarios is investigated in this thesis. Here, the design principles of the three aforementioned categories of mission scenarios are discussed.

## 5.2 Inline (GRACE-like) Missions

The effects of satellite repeat orbit, mission height and its ground-track gap evolution for near-polar inline missions are investigated among different orbit configurations (Table 5.1). All the formations are assumed to be near polar (with inclination of  $89.5^\circ$ ). An inline GRACE-like formation with repeat orbit of  $\beta/\alpha = 503/32$  (altitude of 333.8 km) is assumed as the arbitrary reference configuration for the investigation.

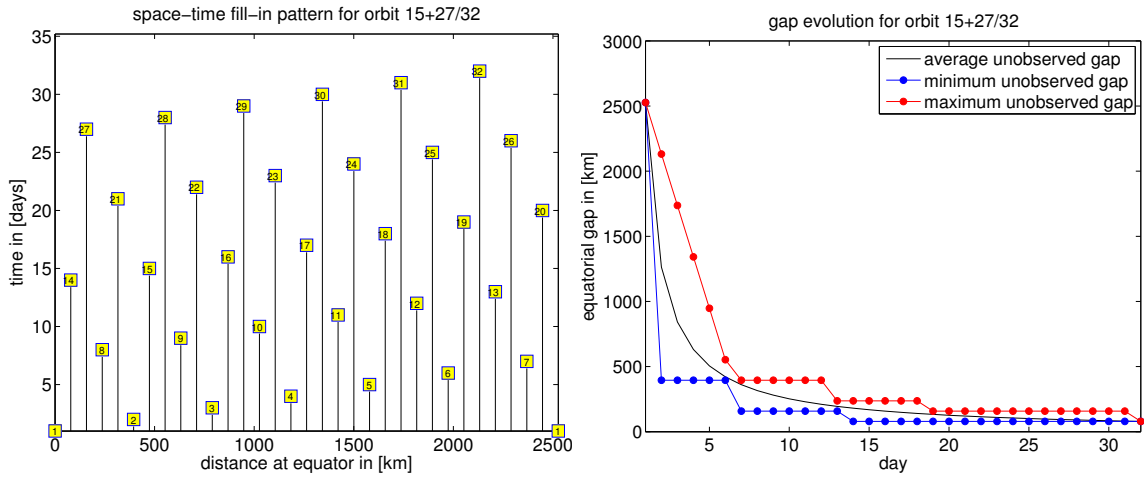
One important orbit design parameter is the satellite altitude. Due to the significant

Table 5.1: Orbit architectures of the single inline near-polar satellite missions

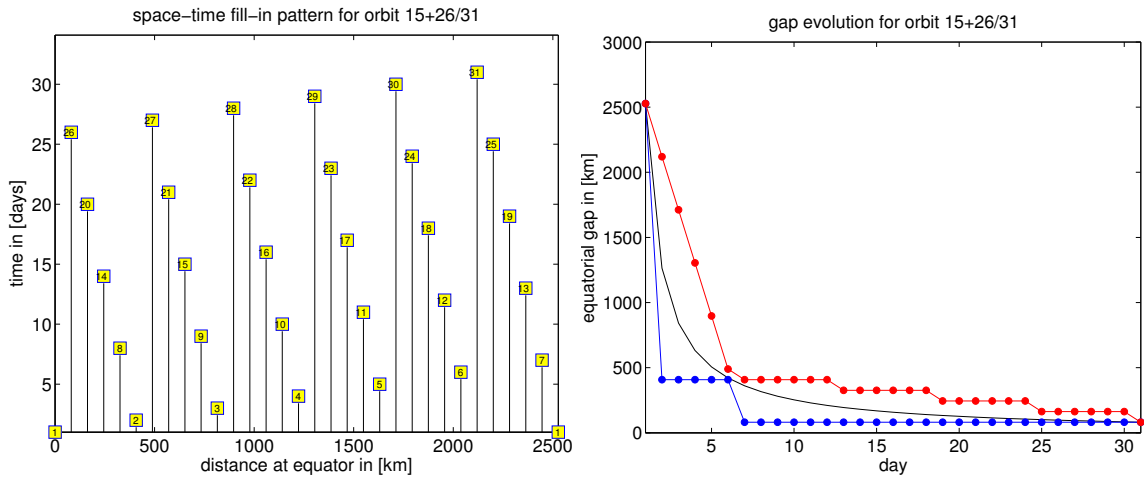
scenario	$\beta$ [rev.]	$\alpha$ [days]	altitude [km]	sub-cycle [days]
1.1	507	32	298.4	13
1.2	491	31	299.8	6
1.3	396	25	299.4	6
1.4	364	23	303.3	6
1.5	317	20	296.6	7
1.6	206	13	297.6	6
1.7	95	6	301.3	1
1.8	503	32	333.8	7
1.9	485	31	354.9	14
1.10	391	25	356.4	11
1.11	125	8	360.7	3
1.12	205	13	319.4	4
1.13	142	9	317.0	4
1.14	497	32	387.9	15
1.15	501	32	351.7	3
1.16	509	32	280.8	11
1.17	511	32	263.4	1
1.18	490	31	308.9	5
1.19	488	31	327.2	4
1.20	493	31	281.7	10
1.21	110	7	335.1	3
1.22	495	31	263.7	1

increase of atmospheric drag force by decreasing the altitude, implementation of satellite missions with the altitudes lower than 300 km is technically challenging (St Rock et al., 2006; Wiese et al., 2011b). However, in order to investigate the effect of satellite height on the recovery, a range of satellite altitudes between 260 and 400 km is considered in the framework of this study.

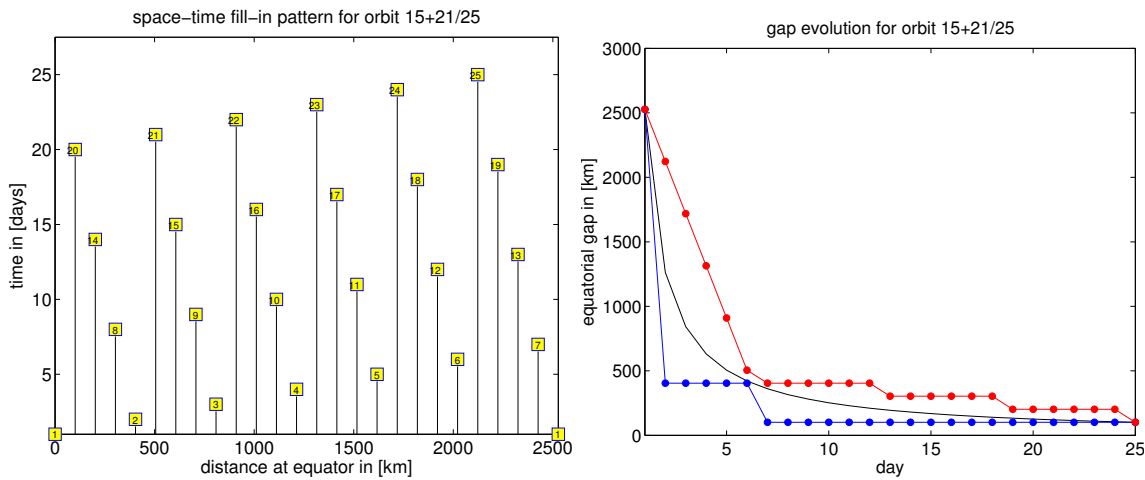
The effect of repeat orbits of the configurations on the recovery quality is also of great interest. It is tried to consider a range of repeat orbit within the altitude of 260 to 400 km. Moreover, the sub-cycles of these configurations are chosen to cover a range of time intervals, from 1 day (drifting orbit) to long time interval (15 days). The evolution of satellite ground-track pattern can be therefore studied through the sub-cycles and gap evolution figures. Figure 5.1 shows the space-time fill-in pattern and ground-track gap evolution graphs of the configurations of Table 5.1. The space-time fill-in pattern of the figure represents the fundamental interval ( $S$ ) at the equator ( $X$ -axis) and the duration of a repeat cycle ( $Y$ -axis). Each square in the individual figure represents an ANX and shows when it occurs (number of the nodal days) and where it falls within  $S$ . In the gap evolution graphs, the minimum, maximum and average unobserved gaps for each day are illustrated (respectively by blue, red and black curves). The graphs include a range from slow gap-filling ground-tracks, as in drifting orbits with one day sub-cycles (scenarios 1.7, 1.17 and 1.22), to fast gap-filling ground-tracks like the ones in missions 1.1, 1.9, 1.10, 1.11 (as examples for different type of fast gap-filling scenarios).



(i) Scenario 1.1:  $\beta/\alpha = 507/32$ ,  $sc = 13$  days

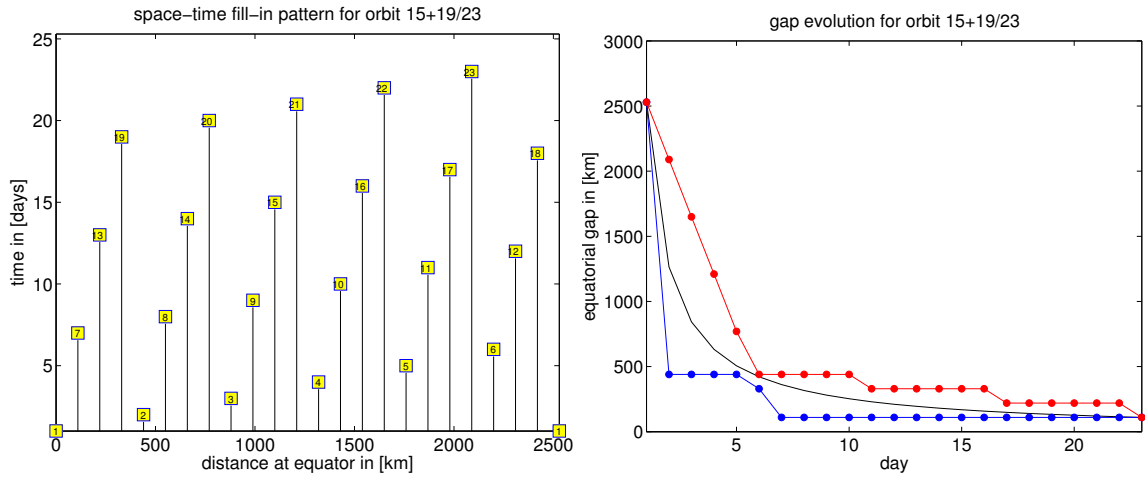


(ii) Scenario 1.2:  $\beta/\alpha = 491/31$ ,  $sc = 6$  days

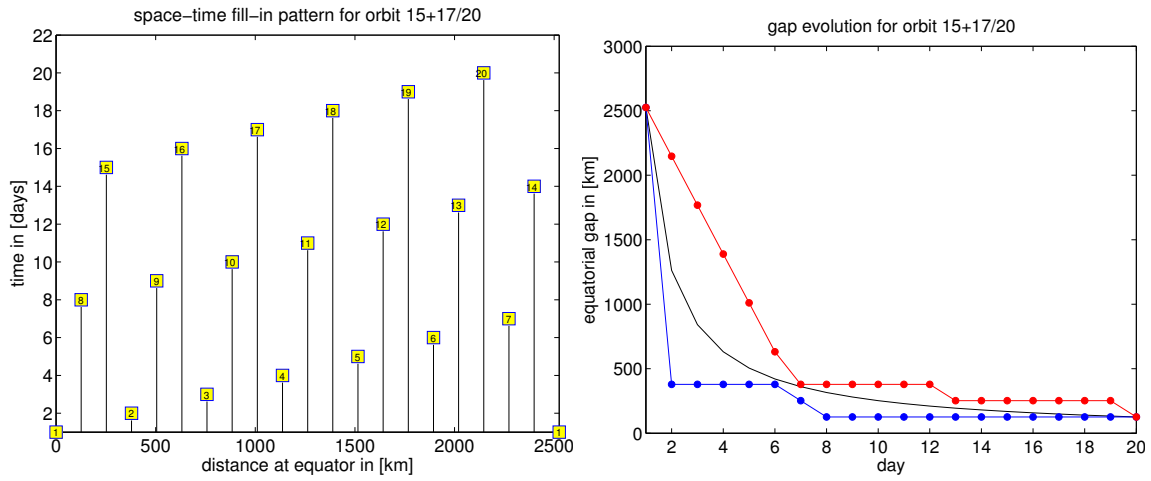


(iii) Scenario 1.3:  $\beta/\alpha = 396/25$ ,  $sc = 6$  days

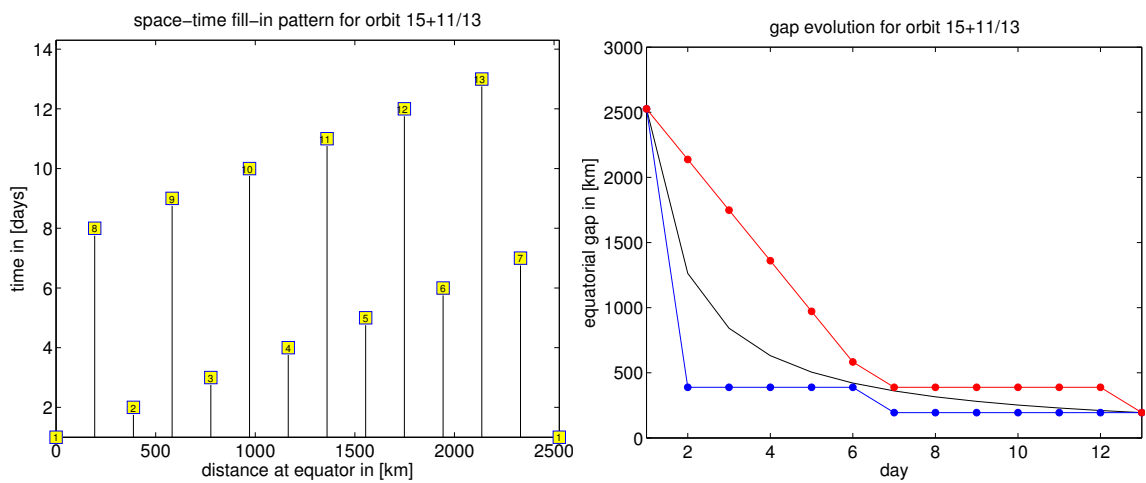
## 5 Orbit Design and Formation Flight Mission Scenarios



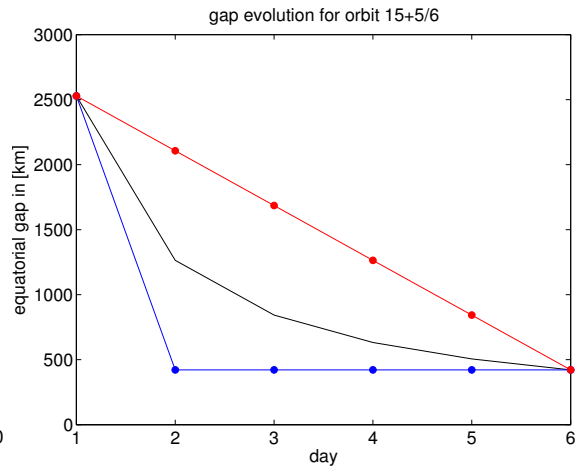
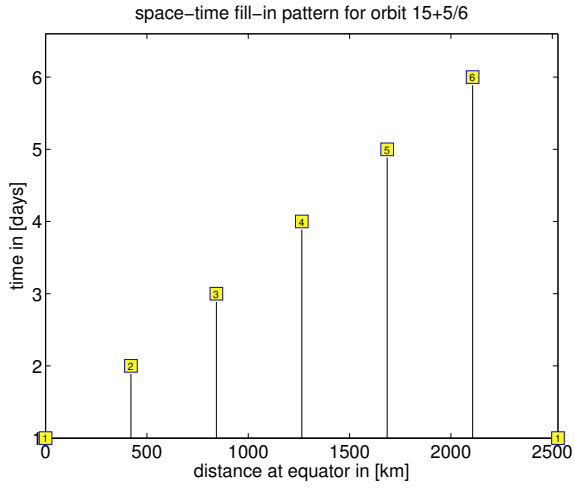
(iv) Scenario 1.4:  $\beta/\alpha = 364/23$ ,  $sc = 6$  days



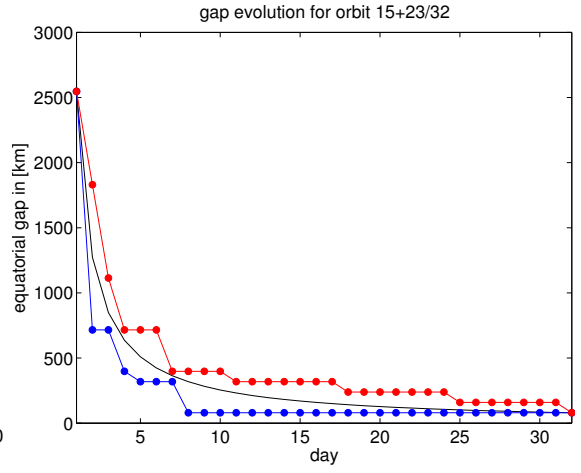
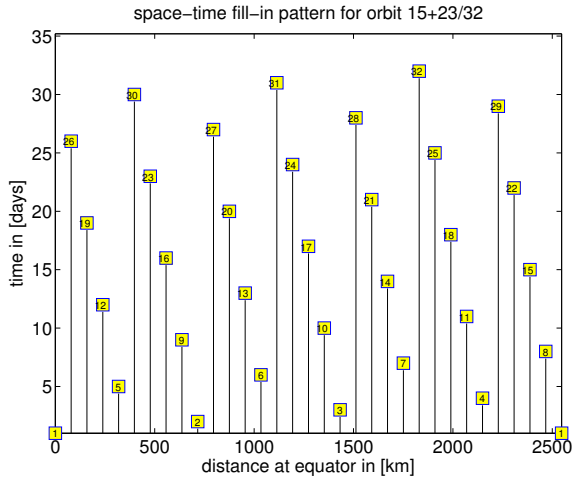
(v) Scenario 1.5:  $\beta/\alpha = 317/20$ ,  $sc = 7$  days



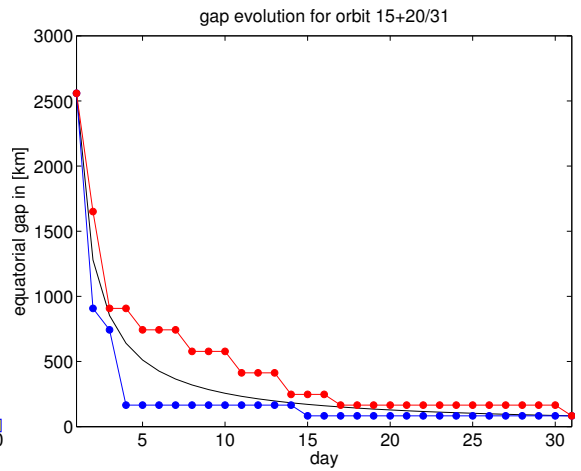
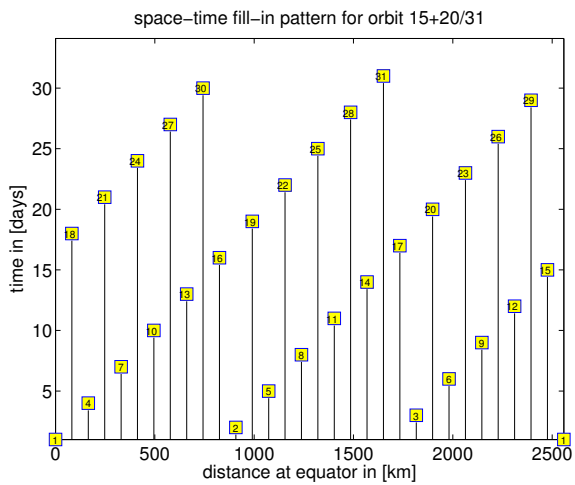
(vi) Scenario 1.6:  $\beta/\alpha = 206/13$ ,  $sc = 6$  days



(vii) Scenario 1.7:  $\beta/\alpha = 95/6$ ,  $sc = 1$  day

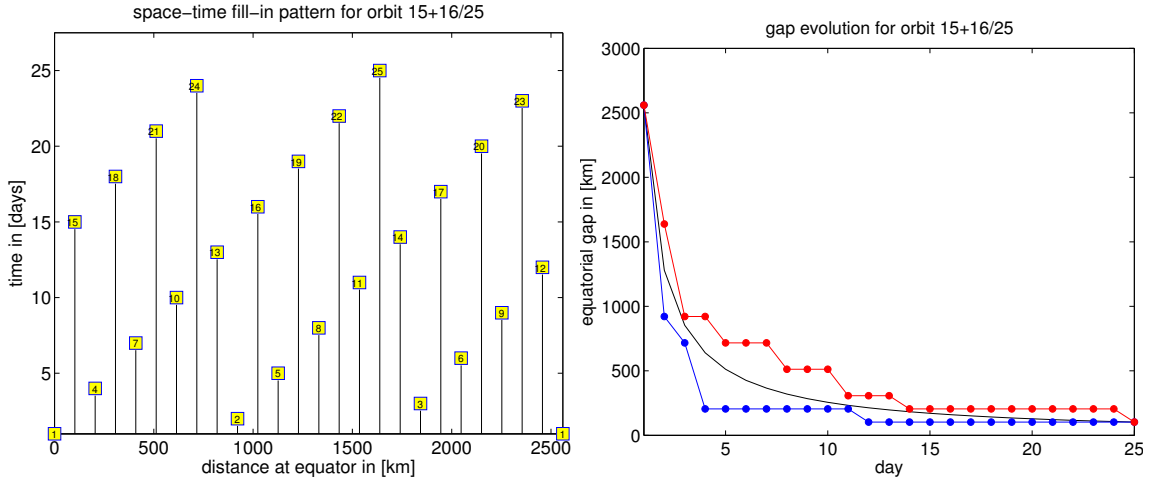


(viii) Scenario 1.8:  $\beta/\alpha = 503/32$ ,  $sc = 7$  days

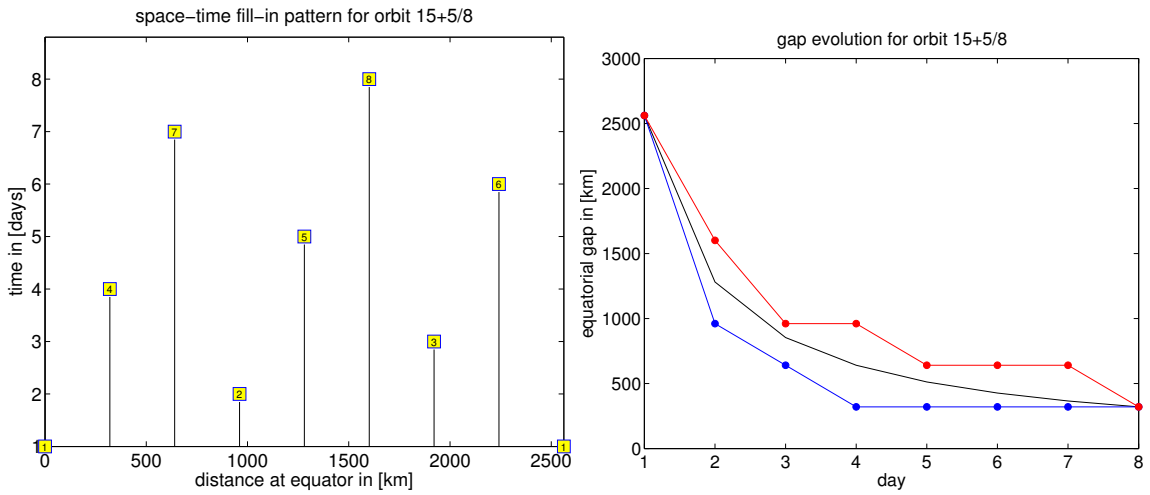


(ix) Scenario 1.9:  $\beta/\alpha = 485/31$ ,  $sc = 14$  days

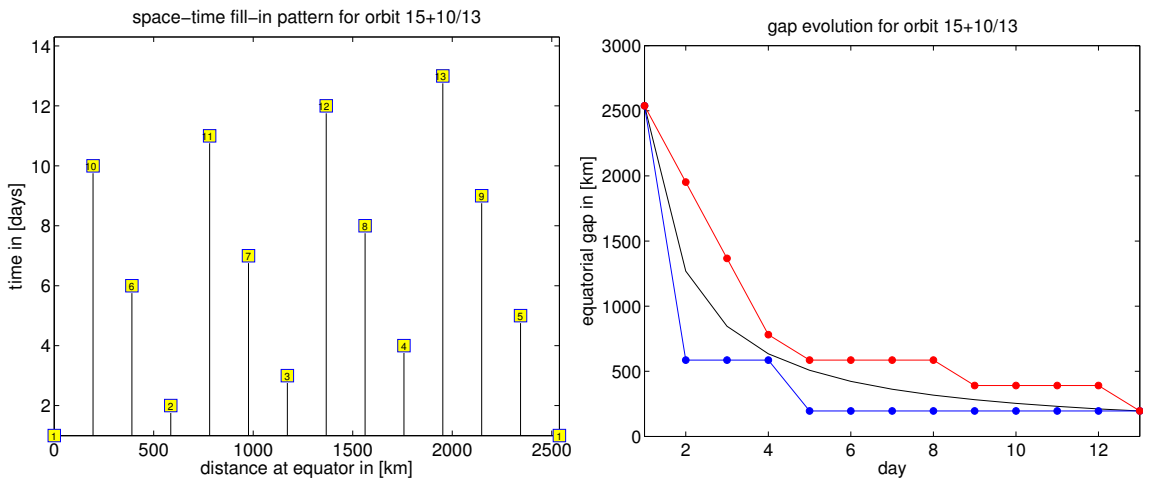
## 5 Orbit Design and Formation Flight Mission Scenarios



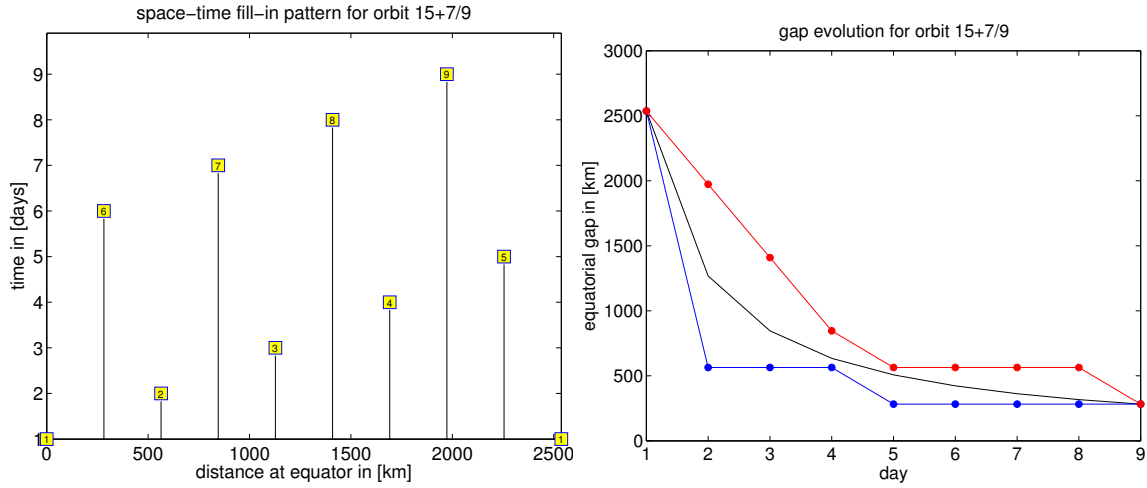
(x) Scenario 1.10:  $\beta/\alpha = 391/25$ ,  $sc = 11$  days



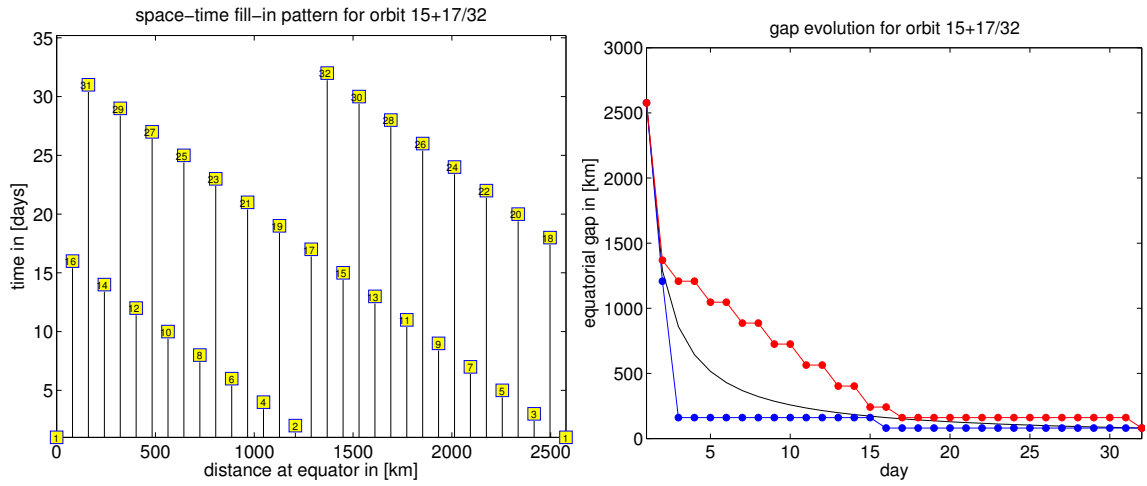
(xi) Scenario 1.11:  $\beta/\alpha = 125/8$ ,  $sc = 3$  days



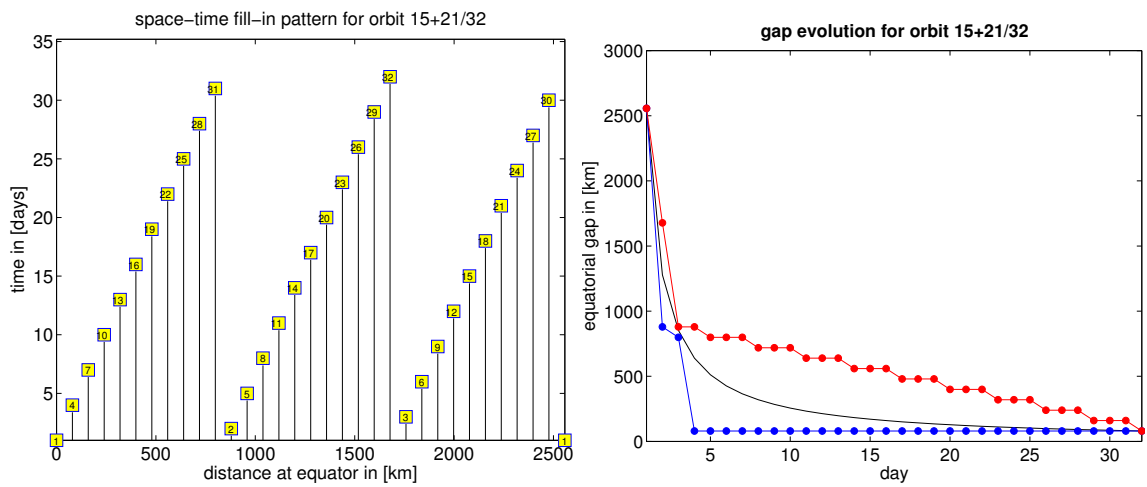
(xii) Scenario 1.12:  $\beta/\alpha = 205/13$ ,  $sc = 4$  days



(xiii) Scenario 1.13:  $\beta/\alpha = 142/9$ ,  $sc = 4$  days

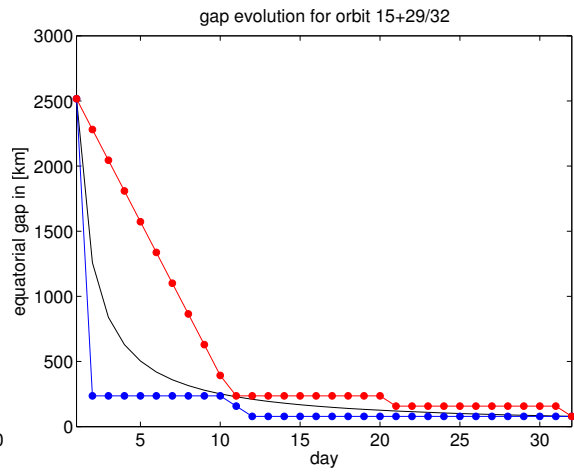
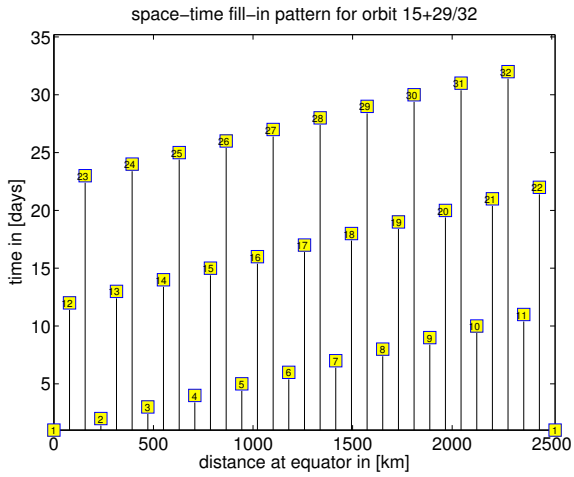


(xiv) Scenario 1.14:  $\beta/\alpha = 497/32$ ,  $sc = 15$  days

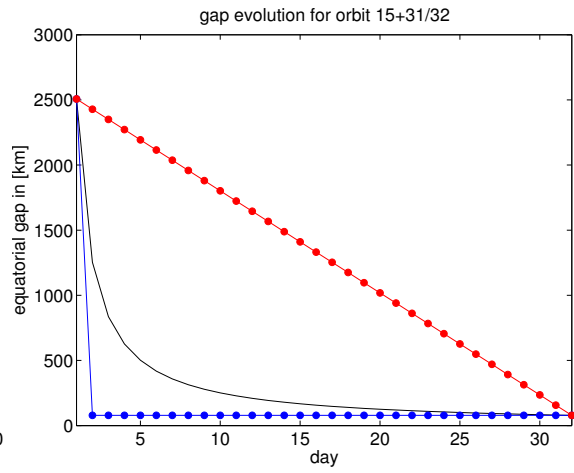
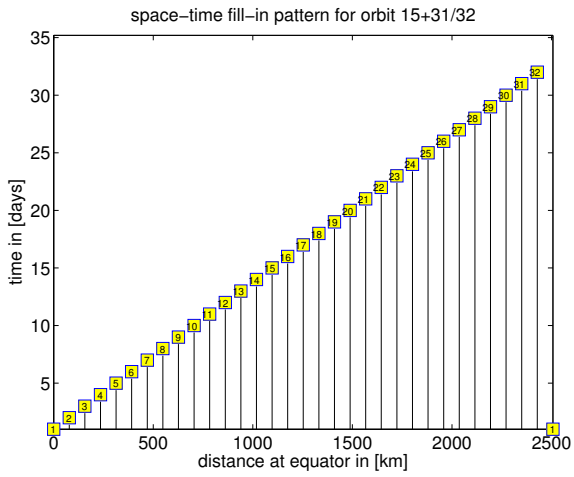


(xv) Scenario 1.15:  $\beta/\alpha = 501/32$ ,  $sc = 3$  days

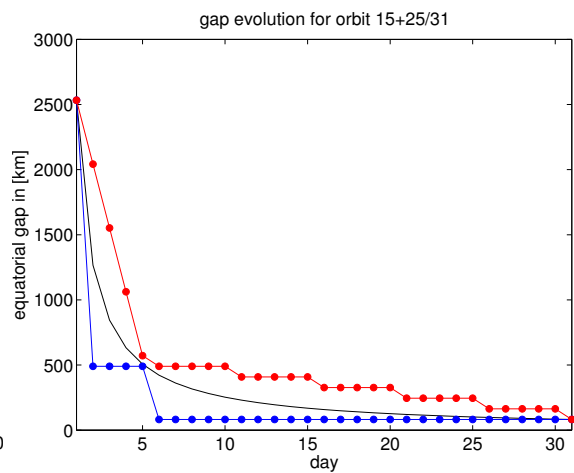
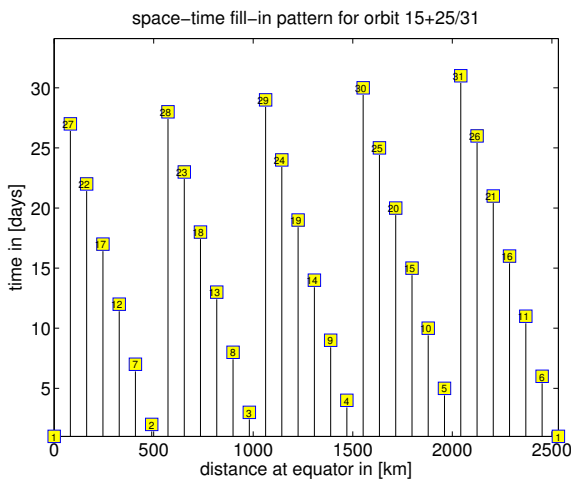
## 5 Orbit Design and Formation Flight Mission Scenarios



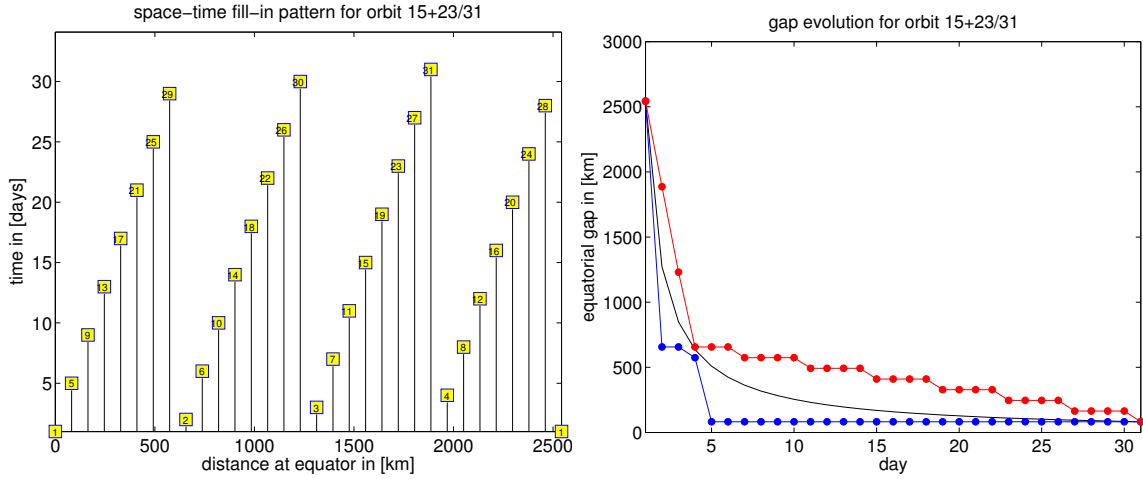
(xvi) Scenario 1.16:  $\beta/\alpha = 509/32$ ,  $sc = 11$  days



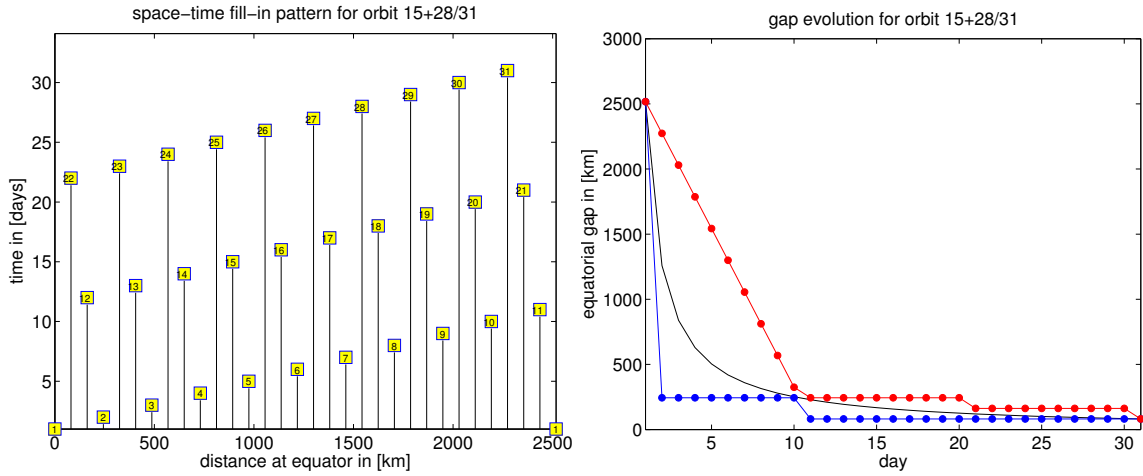
(xvii) Scenario 1.17:  $\beta/\alpha = 511/32$ ,  $sc = 1$  day



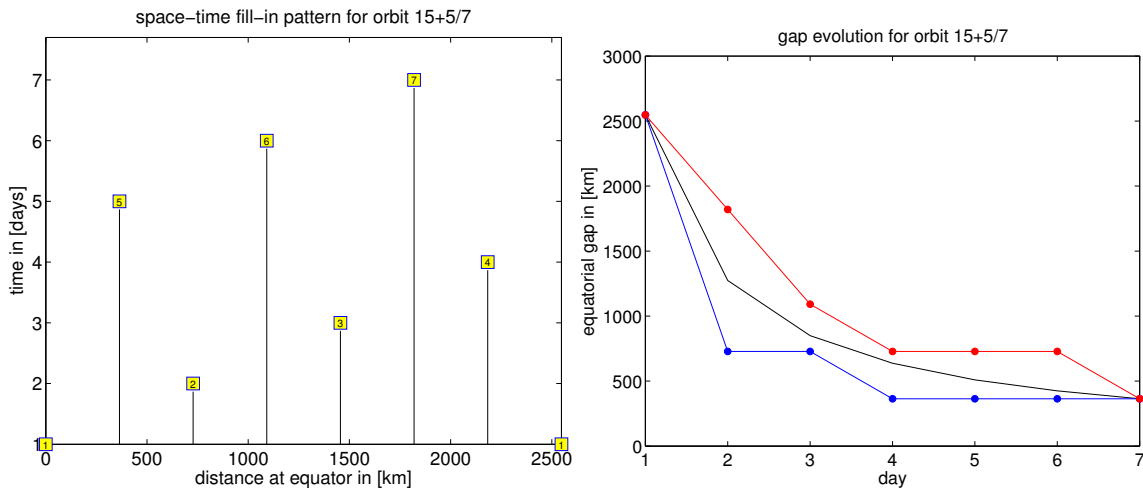
(xviii) Scenario 1.18:  $\beta/\alpha = 490/31$ ,  $sc = 5$  days



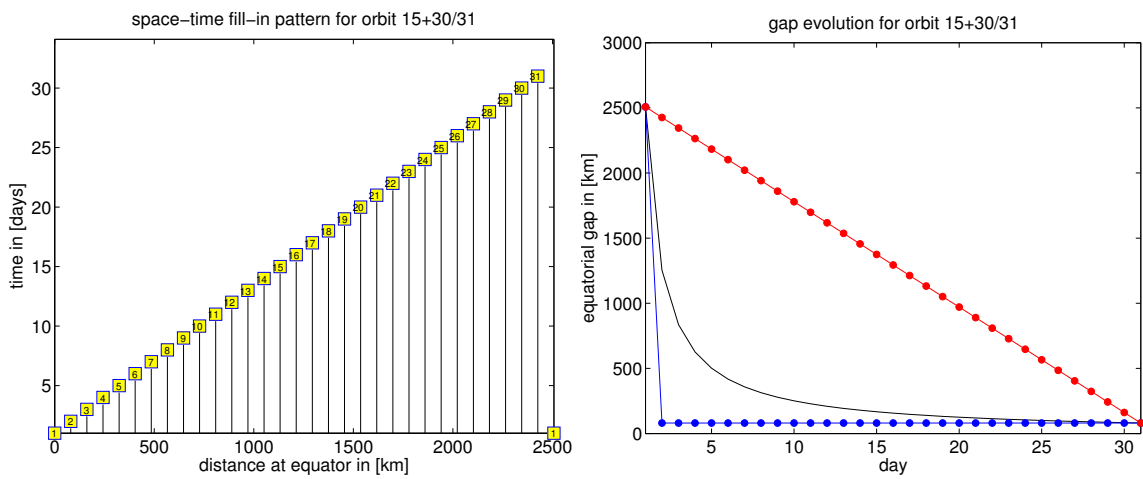
(xix) Scenario 1.19:  $\beta/\alpha = 488/31$ ,  $sc = 4$  days



(xx) Scenario 1.20:  $\beta/\alpha = 493/31$ ,  $sc = 10$  days



(xxi) Scenario 1.21:  $\beta/\alpha = 110/7$ ,  $sc = 3$  days



(xxii) Scenario 1.22:  $\beta/\alpha = 495/31$ ,  $sc = 1$  day

Figure 5.1: Space-time fill-in pattern (left) and gap evolution graphs (right) of repeat orbits configurations of Table 5.1.

Table 5.2: Inline and alternative formation flights for the assumed reference orbit:  $\beta/\alpha = 503/32$  (altitude of 333.8 km)

formation	$\rho_x$ [km]	$\rho_y$ [km]	$\rho_z$ [km]
Inline (GRACE-like)	100	0	0
GFO (GRACE Follow-on)	100	10	0
Pendulum	96	43	0
Cartwheel (polar-radial)	100	0	50
Cartwheel (equatorial-radial)	100	0	50

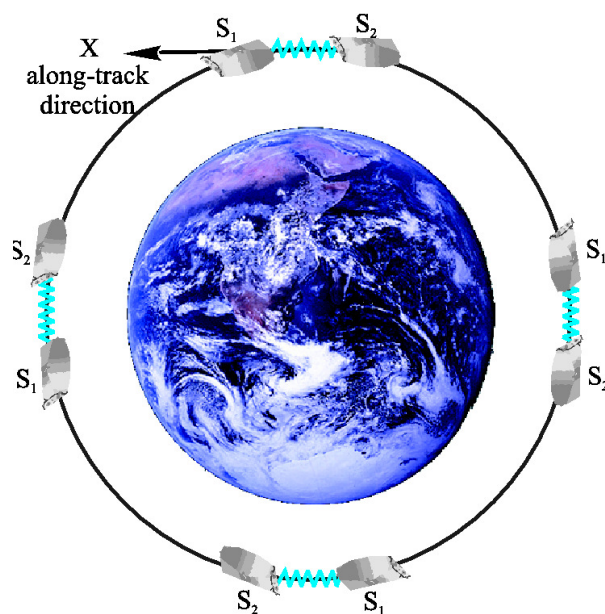
### 5.3 Alternative Formations

Previous studies such as (Sharifi et al., 2007), (Wiese et al., 2009), (Elsaka, 2010) and (ESA, 2011) show that the use of alternative formations, in which the relative motion contains more components than only the GRACE-type inline observable, improve the quality of the gravity recovery. Here, the following formation types are investigated:

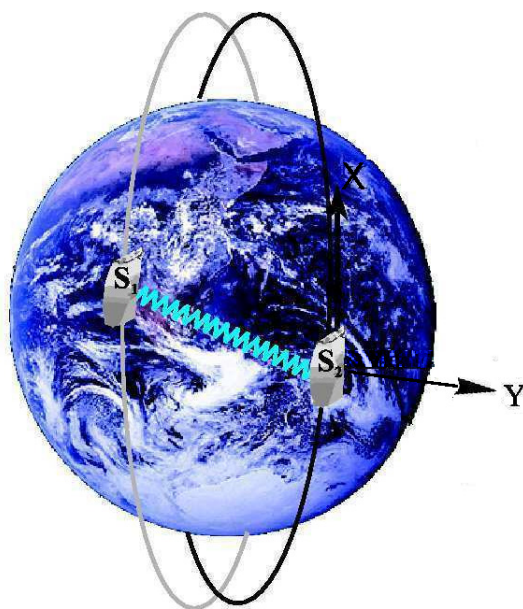
- (i) Inline (GRACE-like)
- (ii) GFO (conservative pendulum formation)
- (iii) Pendulum
- (iv) Cartwheel (polar-radial)
- (v) Cartwheel (equatorial-radial)

The nominal repeat orbit  $\beta/\alpha = 503/32$  is chosen as an arbitrary reference orbit among the scenarios with near-homogeneous ground-track pattern. The intersatellite distances of the formations are shown in Table 5.2. The quality improvement by alternative formations GFO (GRACE Follow-on as a conservative pendulum formation), Pendulum, polar-radial Cartwheel and equatorial-radial Cartwheel with  $\beta/\alpha = 503/32$  (altitude of 333.8 km), compared to the reference inline mission, is investigated. Here, the along-track distance in the inline mission is set to 100 km (Wiese et al., 2011b). The GFO scenario is considered as a conservative Pendulum with a small opening angle around  $5^\circ$  (i.e.  $\rho_y/\rho_x \approx 10\%$ , where  $\rho_x$  is the along-track satellite distance and  $\rho_y$  is the maximum cross-track distance). The Cartwheel formation makes use of two satellites with one at apogee of its orbit while the other is at perigee of its orbit. The polar-radial Cartwheel has a radial line of sight vector above the poles, while the equatorial-radial Cartwheel shows a radial line of sight above the equator. That means, for the polar-radial Cartwheel, the observable has only a radial component above the poles and an inline component above the equator, whereas it is vice-versa for the equatorial-radial Cartwheel. It has to be noted that the orientation of near-polar Cartwheel formations changes due to perigee drift, caused by the oblateness of the Earth (Sneeuw et al., 2008). That means these two different scenarios of Cartwheel formation are not stable, where the latitudes of pure radial or pure along-track components (at pole or equator) change over time. The perigee drift by  $J_2$  (the dominant Earth gravitational perturbation by Earth's flattening) is approximately  $4^\circ$  per day ( $\dot{\omega} = 4^\circ/\text{day}$ ) which is responsible for around  $120^\circ$  perigee drift in a month (Sneeuw et al., 2008).

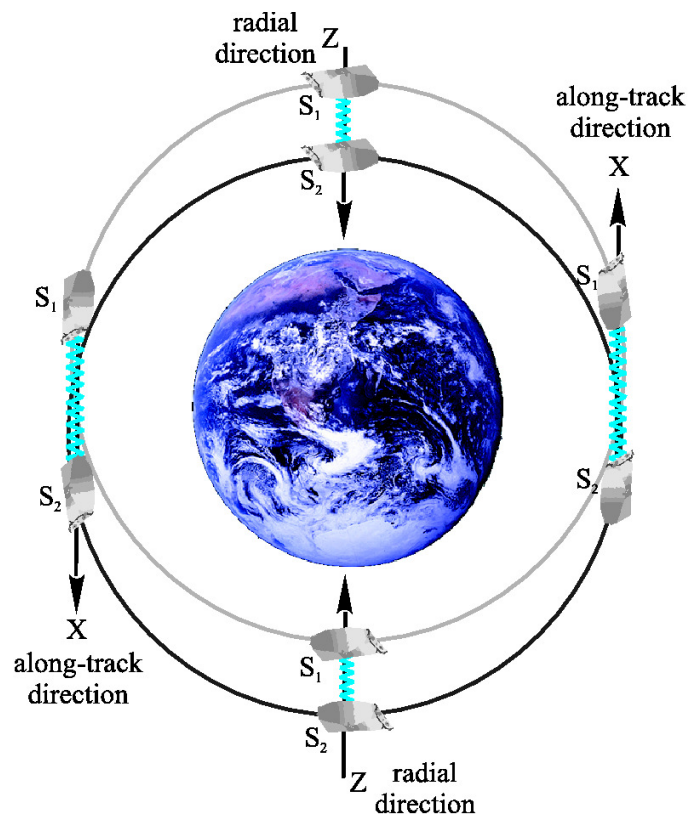
The schematic views of GRACE-like and those alternative (advanced) formation flights are represented in Figures 5.2.



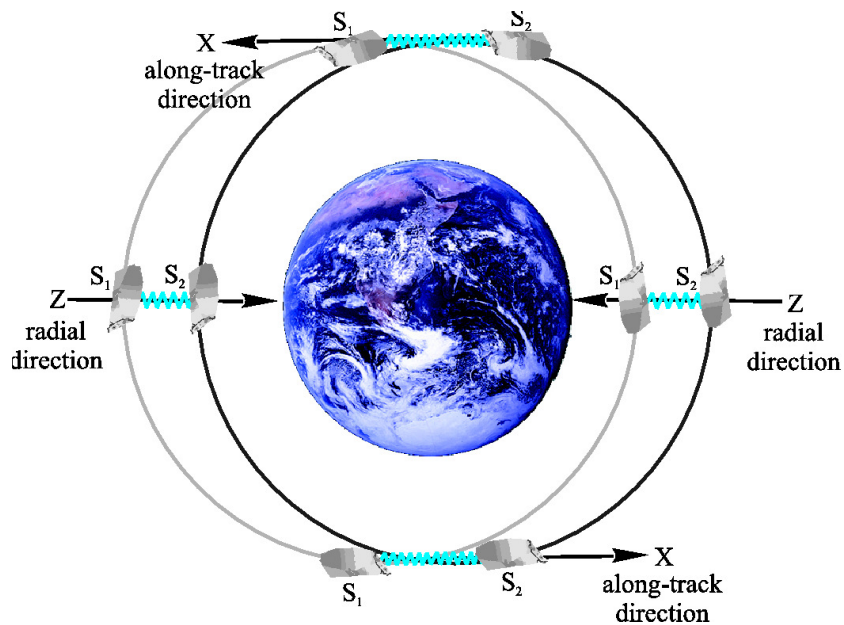
(i) Inline (GRACE-like) with along-track measurement component



(ii) Pendulum with along-track and cross-track measurement components



(iii) Cartwheel (polar-radial) with along-track and radial measurement components



(iv) Cartwheel (equatorial-radial) with along-track and radial measurement components

Figure 5.2: Schematic views of inline and alternative formation flights (Elsaka, 2010).

## 5.4 Double Pair Missions

Bender et al. (2008) show that the spatial-temporal resolution of the gravity recoveries for time-variable gravity field can be improved by employing two pairs of inline formations, when one is in a near-polar orbit and the other is in a lower inclined orbit. Figure 5.3 illustrates a schematic view of such configuration, while Figure 5.4 illustrates the ground-tracks pattern distribution of such scenario on Earth's latitude.

In this study, different scenarios for dual satellite missions are investigated (Table 5.3). Except for the big polar gap scenario 2.10, the inclination of the second pair of satellites is set to  $72^\circ$ . That inclination angle is taken from a discussion by Wiese et al. (2011b) which show that the optimal inclination of the second pair is between  $70^\circ$  and  $75^\circ$ , when the first pair is in near polar orbit. Although the work by (Wiese et al., 2011b) holds for full-repeat period recoveries, they are also assumed to be good choices for shorter time-interval solutions. The first four scenarios of Table 5.3 consist of two inline missions, one near-polar ( $89.5^\circ$ ) and the other inclined ( $72^\circ$ ) by application of

- (i) two long-repeat period missions,
- (ii) short-repeat period and long-repeat period,
- (iii) long-repeat period and short-repeat period, and
- (iv) two short-repeat period orbits.

The next four missions are designed based on the same repeat period scenarios of the first four missions, but here, it is tried to keep the satellite altitudes at around 300 km. The slow and fast repeat orbits (long and short repeat periods) of the main four scenarios are chosen to depict the different sampling scenarios of near-polar and inclined missions. The effect of missions' altitude is then investigated by the comparison of the results of first and second categories of aforementioned main four mission scenarios. The ninth scenario, suggested by Wiese et al. (2011b) as the optimal scenario, has approximately the same altitude as the previous four ones, but the repeat periods of the missions are in between of those two previous categories (13 days). Finally, scenarios 2.10 and 2.11 have polar gaps of  $15^\circ$  and  $7^\circ$ . The idea with these two scenarios is to investigate the effect of more samples of the gravity field in the lower latitudes on the quality of the gravity recoveries of those latitudes.

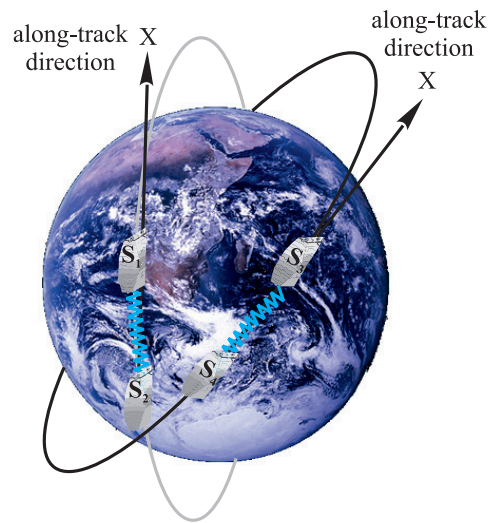


Figure 5.3: Two pairs inline configurations with different inclination angles (Elsaka, 2010).

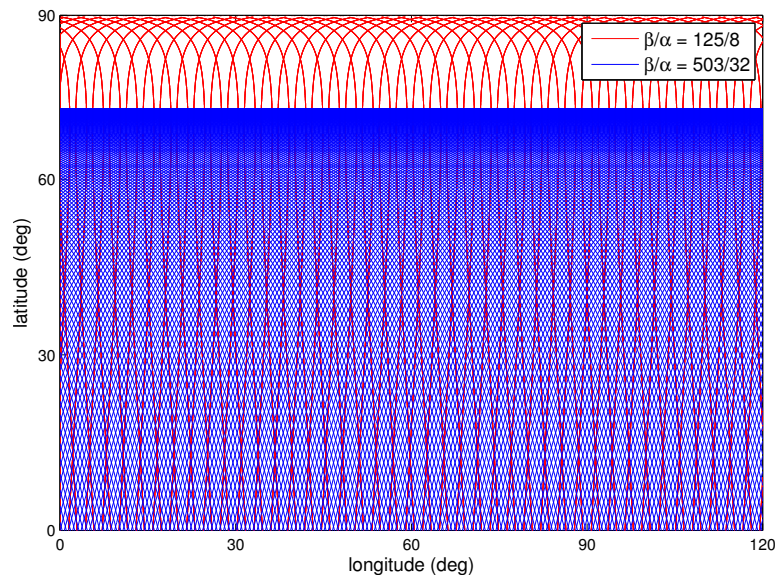


Figure 5.4: An example of ground-track pattern of a dual pair inline configuration with different inclination angles (scenario 2.2 of Table 5.3) after 32 days.

Table 5.3: Orbit architectures of two pairs of satellite missions ( $\Delta\Omega = 180^\circ$ )

scenario	formation	inclination [deg.]	$\beta$ [rev.]	$\alpha$ [days]	altitude [km]
2.1	Inline	89.5	503	32	333.8
	Inline	72	503	32	305.0
2.2	Inline	89.5	125	8	360.7
	Inline	72	503	32	305.0
2.3	Inline	89.5	503	32	333.8
	Inline	72	125	8	332.1
2.4	Inline	89.5	125	8	360.7
	Inline	72	125	8	332.1
2.5	Inline	89.5	507	32	298.4
	Inline	72	488	31	298.3
2.6	Inline	89.5	142	9	317.0
	Inline	72	488	31	298.3
2.7	Inline	89.5	507	32	298.4
	Inline	72	110	7	306.2
2.8	Inline	89.5	142	9	317.0
	Inline	72	110	7	306.2
2.9	Inline	89.5	206	13	297.6
	Inline	72	205	13	290.4
2.10	Inline	75	205	13	295.0
	Inline	105	206	13	327.3
2.11	Inline	97	206	13	311.7
	Inline	72	205	13	290.4

# 6 Quality Assessment of Sub-Nyquist Recovery from Future Gravity Satellite Missions

This chapter deals with assessment of quality of sub-Nyquist gravity field recovery of different satellite orbit configurations and formation flights. Here, the quality of gravity solutions of the time-intervals with the number of satellite revolutions below the required number by Colombo-Nyquist rule is investigated. Furthermore, three satellite mission scenarios with near-optimal gravity solutions in terms of spatial and temporal resolutions are chosen and then subjected to the post-processing tools.

## 6.1 Quality of the Gravity Field Recoveries

Based on a simplified version of the ll-SST acceleration approach using nominal orbits (quick-look tool) and Hill's equations (Chapters 3 and 4), simulations for different repeat orbits of a single inline satellite pair, alternative formation flights and double satellite pair missions of Chapter 5 have been conducted. As input, all relevant time-variable gravity fields of atmosphere, ocean, hydrology, ice and solid Earth (AOHIS) and the difference of two ocean tide models of the year 2005 have been adopted (Table 4.1). The measurements are simulated at  $\Delta t = 5$  s sampling interval. The error is represented as the difference between the gravity recovery (output) and the mean of the time-variable gravity models (input) for the same time interval:

$$\text{error} = \text{gravity solution (output)} - \text{mean of the time-variable gravity models (input)}$$

It is important to mention that all geophysical models of this study are smoothed by 220 km Gaussian filter to avoid ringing effects caused by truncation error. Moreover, the coefficients' error  $\Delta C_{00}$ ,  $\Delta C_{10}$ ,  $\Delta C_{11}$  and  $\Delta S_{11}$  are neglected due to the insensitivity of ll-SST measurement concepts for these coefficients. Indeed, the degree zero term drops out of the simulations because the total mass in the surface layer is considered constant. For degree one, there can not be  $l = 1$  gravitational potential for the Earth system when the coordinate origin is defined as the center of mass, therefore the degree one error has been set to zero, as well. Furthermore,  $\Delta C_{20}$  is ignored in the error simulations. The assumption is taken from some discussions over the poor determination of  $C_{20}$  by ll-SST measurements, particularly by GRACE (see Chen et al., 2005).

As discussed before, the Earth coverage by a specific satellite mission scenario, presented by the gap evolution of the satellite mission ground-tracks, may influence the quality of the gravity recovery. Therefore, it will be of a great interest to investigate the correlation between the gap evolutions by different orbit configurations (as an indicator of gaps' sizes and the homogeneity of the Earth coverage by the mission scenarios) and their gravity solutions. Consequently, one task of this study is to search for orbital configurations and formation flights with optimal homogeneous coverage of the Earth. It is also expected that for each configuration, at one point of time, the space domain is almost homogeneously sampled.

Therefore, one may expect a significant quality improvement of the gravity recovery at that time point. This time interval then stands for the temporal resolution of the solution. The spatial resolution of such configuration is then determined by the Earth coverage pattern by that satellite mission.

Here, the validity of Colombo-Nyquist rule in satellite geodesy is investigated. The quality of the gravity recoveries of different orbit configurations and formations for the time-intervals with less number of satellite revolutions than what is required by Colombo-Nyquist rule is investigated.

### 6.1.1 Recovery Quality from Different Satellite Configurations and Formations

#### Single Pair Inline Configurations

The GRACE-like configurations of Table 5.1 with inter-satellite distance of  $\rho = 100$  km are simulated through the quick-look tool. Figure 6.1 illustrates the global (accumulated) geoid height error rms of 3 to 32-day recoveries for maximum spherical harmonics degree of 45 and 90 by those orbital configurations. Although the solution quality differs from one configuration to the other, it is important to note that a significant error drop occurs at the third day for estimated  $L_{\max} = 45$  and the sixth day for estimated  $L_{\max} = 90$  for all the repeat orbits. Figure 6.2 shows a close-up of the Figure 6.1. Moreover, Table 6.1 summarizes the errors for 5, 6, 7 and 32-days recoveries of Table 5.1 repeat orbits for maximum degree and order 90. From the table, it can be seen that for the scenarios with error less than 1 cm for 6-day recovery, the improvement from the fifth to the sixth day is more than 1000 times, whereas from the sixth to the seventh day is less than 2 times. For the other scenarios, the improvement from 6-day recovery to 7-day recovery is also not larger than 4.1 times. This fact confirms that at 6-day gravity solutions, a very significant improvement of spatial resolution is obtained. Indeed, the problem is caused by the poor conditioning of the normal matrices of less than 6-day gravity solutions. Figure 6.3 shows the condition numbers of normal matrices of different gravity solutions, where the condition number (the ratio between the maximal and the minimal singular values) measures the sensitivity of the solution of a system of linear equations to errors in the data and provides an indication of the accuracy of the results from matrix inversion and the linear equation solution.

Figure 6.2 also indicates that for short time solutions, the drifting orbits (with one day sub-cycle) with similar mission altitudes result in the poorest quality among all the scenarios. Obviously, scenario 1.7 is excepted, since 6-day is the full repeat period of the orbit. Moreover, Figure 6.1 and Table 5.1 show that the quality of the recoveries depends on both the altitude of the satellite and the repeat orbit ( $\beta/\alpha$ ). The altitude seems to have a more important influence, if the very large unobserved gaps (as in drifting orbit) are avoided.

**Investigation of Colombo-Nyquist rule** To detect the maximum spherical harmonic degree and order ( $L_{\max}$  and  $M_{\max}$ ) by a gravity satellite mission, the Colombo-Nyquist Rule (CNR) requires number of satellite revolutions of  $2L_{\max}$

$$\beta \geq 2L_{\max} \text{ or } \beta \geq 2M_{\max} \quad (6.1)$$

where  $\beta$  is the number of satellite revolutions in repeat cycle of  $\alpha$  nodal days. Therefore, as an example, to detect maximum degree 90 (i.e. spatial resolution up to degree 90), CNR states that there is a need of at least 180 revolutions in repeat period of the satellite mission. Similarly, according to CNR, to have a spatial resolution of degree 45, at least 90 satellite revolutions in the repeat orbit of the mission are needed. However Figure 6.1 and Table 6.1 show that the quality of recoveries is significantly improved around the time interval when

Table 6.1: Global geoid height error rms for 5, 6, 7 and 32-days recoveries of inline near-polar configurations of Table 5.1 scenarios for maximum degree 90.

scenario	$\beta/\alpha$	altitude km	sub-cycle [days]	error [mm]			
				5-day	6-day	7-day	32-day
1.1	507/32	298.4	13	10526	5.4	3.8	0.8
1.2	491/31	299.8	6	21076	6.5	4.2	0.8
1.3	396/25	299.4	6	19404	6.3	3.9	0.7
1.4	364/23	303.3	6	13718	5.6	4.2	1.0
1.5	317/20	296.6	7	23258	5.9	3.8	0.8
1.6	206/13	297.6	6	14925	5.6	3.8	0.7
1.7	95/6	301.3	1	25460	6.5	6.2	2.8
1.8	503/32	333.8	7	28836	6.9	5.5	1.7
1.9	485/31	354.9	14	9569	26.0	10.7	1.8
1.10	391/25	356.4	11	9750	16.6	8.4	1.7
1.11	125/8	360.7	3	73007	10.6	9.7	3.9
1.12	205/13	319.4	4	53682	7.7	5.7	1.7
1.13	142/9	317.0	4	20909	7.1	5.5	2.0
1.14	497/32	387.9	15	1813900	22.2	10.3	3.4
1.15	501/32	351.7	3	24951	53.5	25.4	2.1
1.16	509/32	280.8	11	928719	2.7	1.9	0.8
1.17	511/32	263.4	1	4826000	139.7	34.8	1.4
1.18	490/31	308.9	5	11977	7.6	6.4	1.4
1.19	488/31	327.2	4	59051	14.7	8.7	3.2
1.20	493/31	281.7	10	629115	3.3	2.0	0.8
1.21	110/7	335.1	3	19792	7.2	6.5	2.8
1.22	495/31	263.7	1	3021400	114.2	29.0	1.4

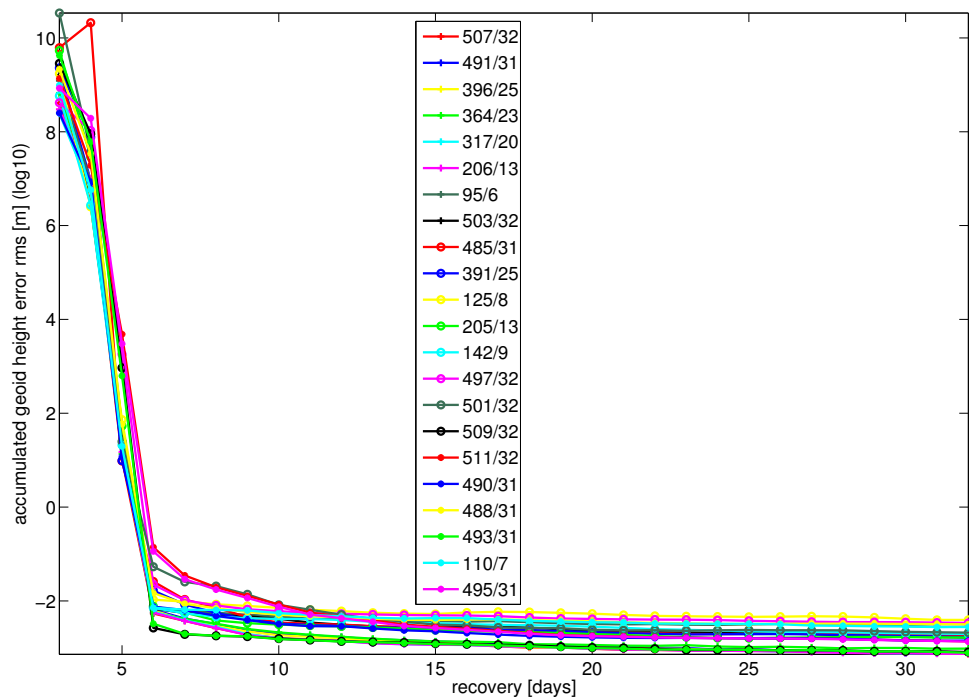
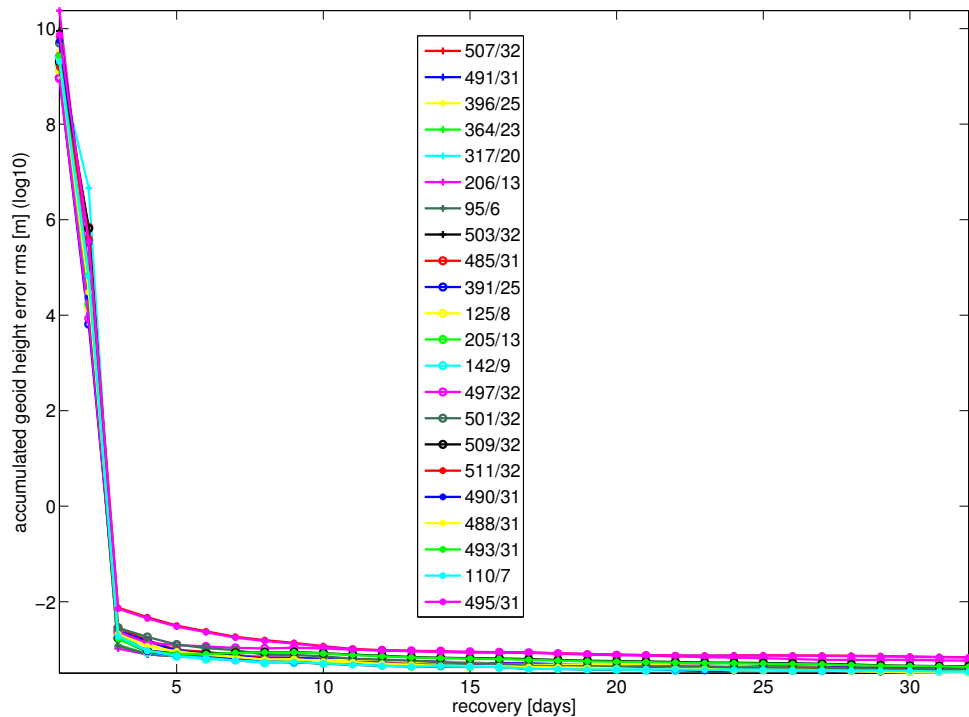


Figure 6.1: Global geoid height error rms of GRACE-like configurations of Table 5.1 for recoveries up to maximum degree 45 (top) and 90 (bottom).

## 6.1 Quality of the Gravity Field Recoveries

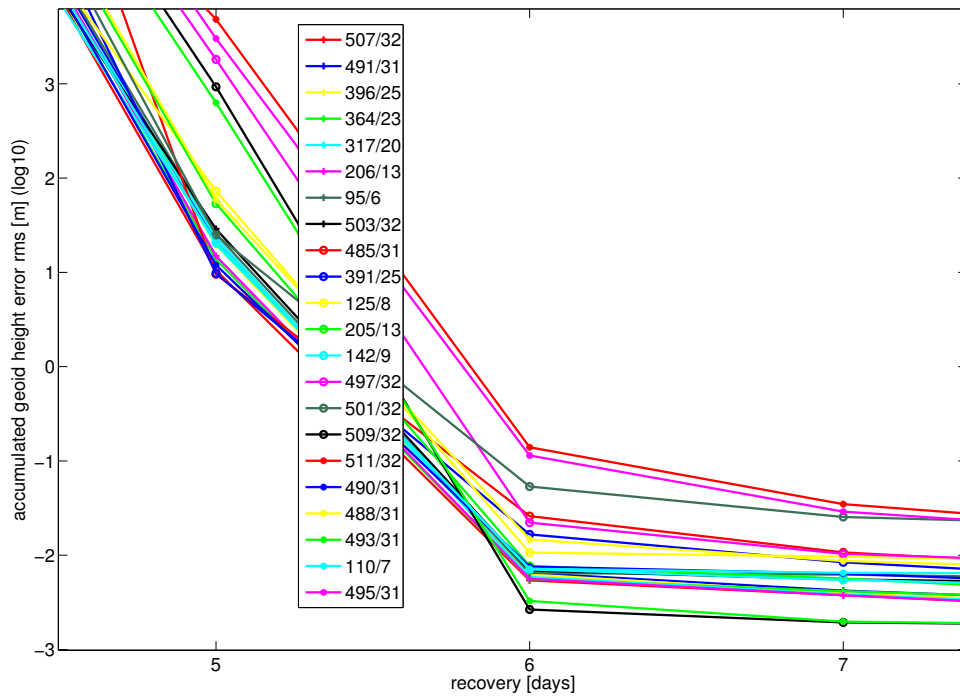
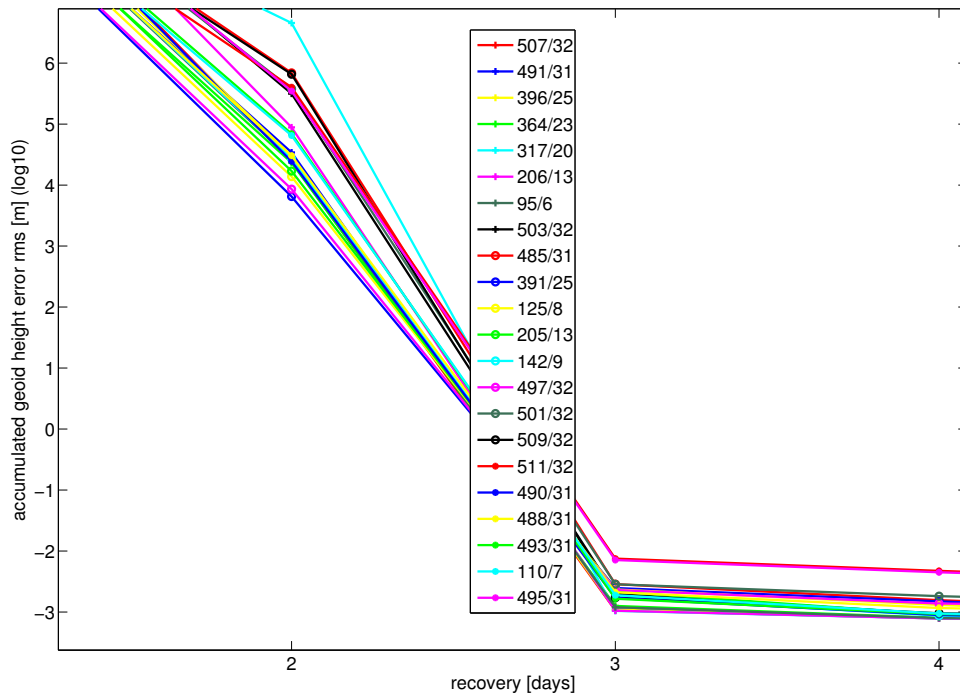


Figure 6.2: Close ups of Figure 6.1.

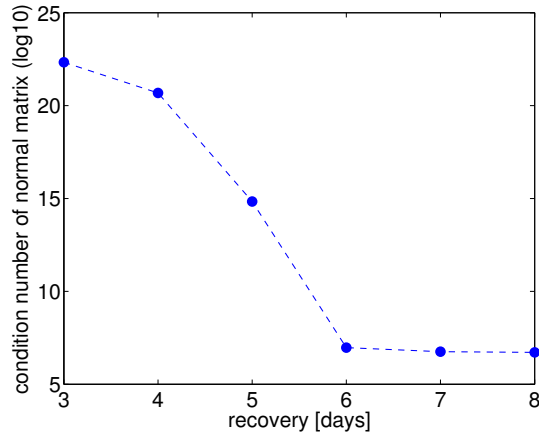


Figure 6.3: Condition number of the normal matrices of 3, 4, 5, 6, 7 and 8-days recoveries of maximum degree 90 for  $\beta/\alpha = 503/32$  repeat orbit (1 s sampling interval).

the number of satellite revolutions equals the maximum spherical harmonics degree and order which is aimed to be detected:

$$B \approx L_{\max} \text{ or } B \approx M_{\max} \quad (6.2)$$

Here,  $B$  is the number of satellite revolutions in a time interval of  $t$ . This phenomenon was already described in Weigelt et al. (2012), denoted as a modification to Colombo-Nyquist rule with the condition that the number of revolutions in repeat period of mission is larger than the required number of revolutions:

$$\beta \geq B \quad (6.3)$$

The condition guarantees that the satellite mission does not repeat itself when the required revolution number ( $B$ ) has not been reached.

For the previous examples, this means that for a gravity recovery up to  $L_{\max} = 90$  about  $B = 90$  satellite revolutions are needed for a significant error improvement if  $\beta \geq 90$ . This is achieved after 6 days for a LEO with approximately 15 revolutions per day. For the recovery up to  $L_{\max} = 45$  that is 3 days when  $\beta \geq 45$ .

**Gap evolution effect and quality investigation of sub-cycle recoveries** The expectation for dependency of the quality of gravity recovery on satellite ground-tracks gap evolution was discussed in the previous chapter. As it was also mentioned, the sub-cycle (SC) is the smallest number of days after which an ANX falls at  $1 \times S_i$  or  $(\alpha - 1) \times S_i$  from the first ANX (ESA, 2011). That is after when a homogeneous Earth coverage by satellite at sub-repeat interval happens, i.e. when the minimum and maximum unobserved gaps by satellite on the Earth get close to each other. From the description of ground-track gap evolution and the definition of sub-cycle, a noticeable drop in gravity recovery error is expected for the time with the minimum gap size and an almost homogeneous ground-track patterns, especially those at the sub-cycle time intervals. However no significant signature at sub-cycle recoveries for different repeat orbit configurations of Figure 6.1 is seen, but, as it was mentioned before, the most significant drop for the repeat orbits happens at the third day for recoveries up to maximum degree 45 and at the sixth day for recoveries up to maximum degree 90. Figure 6.4 illustrates the global geoid height error rms for these two cases, while the corresponding sub-cycle time intervals are shown by vertical lines. The figure does not show any meaningful association between recovery quality and sub-cycle concept. It only seems that the avoidance of large

unobserved gap in drifting orbit plays an important role in recovery quality. This fact can be seen from Figure 6.1 and Table 6.1. That is, in particular, clear for the drifting orbits of scenarios 1.17 and 1.22 with one day sub-cycles (a very slow ground-track gap-filling patterns). The 6-day recovery of the drifting orbit of scenario 1.7 is obviously an exception. Indeed, 6-day is a full repeat orbit of this scenario which means that after 6-day the ground-track patterns get its most homogeneous distribution.

It is also interesting to investigate a possible correlation between the scenarios with less homogeneous gap-filling patterns (large difference between maximum and minimum gap or large unobserved gap by satellite ground-track coverage) and the quality of recoveries. Scenarios 1.9, 1.10, 1.14, 1.15, 1.16, 1.17, 1.19, 1.20 and 1.22 of Figure 5.1 almost show these cases at the 6th day. Looking at Table 6.1, large error values can be seen for those scenarios at 6-day recoveries. The exceptions are the scenarios 1.16 and 1.20 where the 6-day recovery error is the minimum among all configurations. The reason for these small errors, most probably, comes from the low altitude of the mission which is around 280 km. However, for the very low altitude orbits of scenarios 1.17 and 1.22, the errors are very large. These large error values are expected by the drifting orbit or very slow gap-filling ground-track (most inhomogeneous) pattern of these configurations. Considering the effect of mission height as a source for error reduction, the other scenarios with large error values are mostly associated with inhomogeneous ground-tracks coverage at the sixth day (Figure 5.1).

For the long time interval recoveries (32-day), it seems that the effect of mission height is more prominent, although the short repeat period orbits with large unobserved gaps (as in scenario 1.7, 1.11, 1.13 and 1.21 with respectively 6, 8, 9 and 7 full repeat periods) show low recovery quality compared to the missions with similar altitudes (Table 6.1). Other factors may also contribute to the quality of gravity recoveries. The investigation of those factors should be considered for future work. One interesting example is scenario 1.19 ( $\beta/\alpha = 488/31$ ) with an almost large error at 32-day gravity solution. The large global error is caused by the considerable and sudden increase of degree rms error of the configuration around degree 60, even when the tidal error is not considered in the simulation (Figure 6.5). The reason for this sudden increase has not been realized in recovery error budget of this research thesis. Obviously, it is of great interest to investigate the cause in the future work.

**Quality assessment of the recoveries of different orbit configurations** In summary, it can be concluded from the discussion above that the fulfillment of the modified Colombo-Nyquist rule, the mission altitude and avoidance of large unobserved gaps by satellite ground-tracks pattern are the most important factors for the quality of the gravity recoveries, while the sub-cycle concept, apparently, plays no important role for the quality. The focus of this research is on the sub-Nyquist recoveries which fulfill the modified Colombo-Nyquist rule. That is the time with significant improvement in spatial resolution of the recoveries, while the high time resolution can be also achieved. Figure 6.6 shows some examples with different repeat orbit configurations for 6-day gravity recovery. The figure shows that the quality for the drifting orbit  $\beta/\alpha = 511/32$  is the worst among the solutions, although it benefits from the lowest mission altitude. For the other repeat orbits, the degree rms of the errors and geoid height error rms per latitude are almost similar. However, some small quality improvements can be seen for scenario 1.20 (repeat orbit  $\beta/\alpha = 493/31$ ) for high degrees and low latitudes (between  $45^\circ\text{S}$  and  $45^\circ\text{N}$ ) which is most likely caused by the lower altitude of the satellite mission ( $\approx 282$  km).

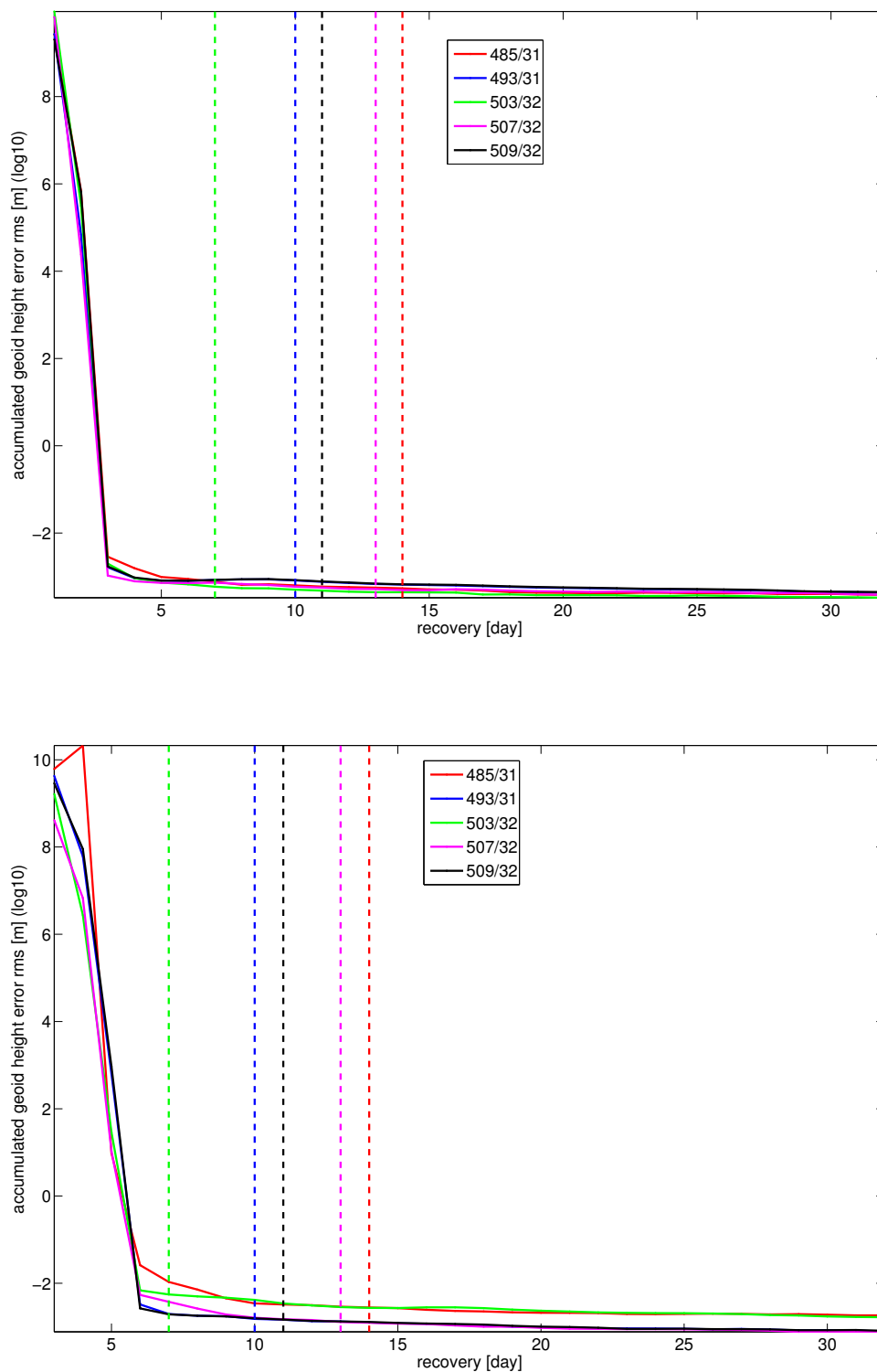


Figure 6.4: Global geoid height error rms by some GRACE-like configurations from Table 5.1 for recoveries of maximum degree and order 45 (top) and 90 (bottom). The vertical dash lines show the corresponding sub-cycle time intervals of the configurations.

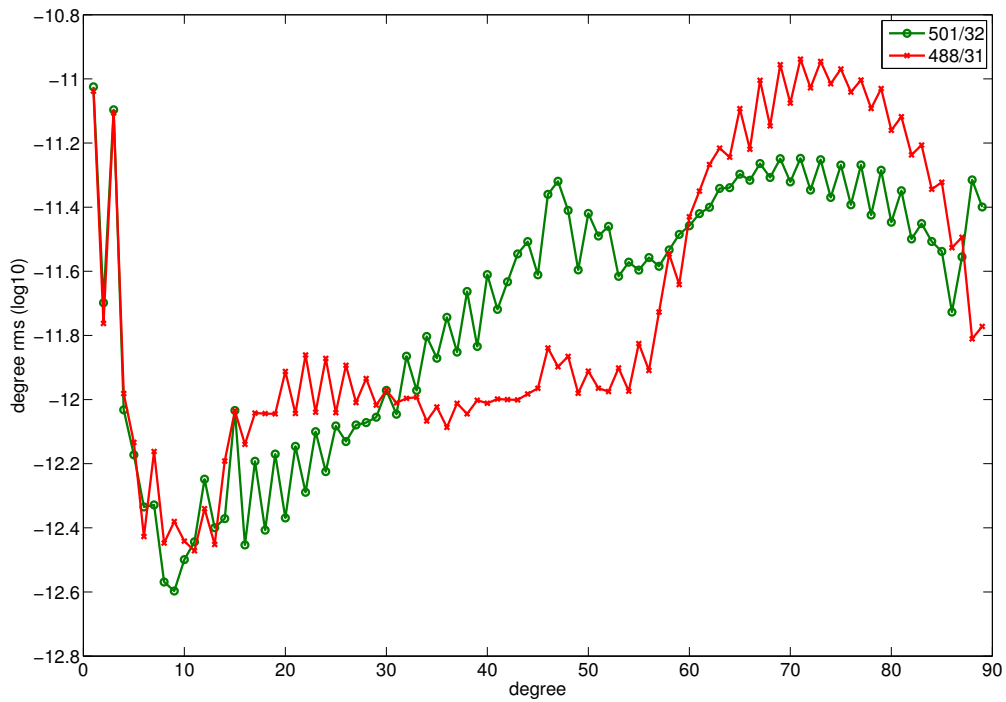


Figure 6.5: Degree rms of the error for scenario 1.19 ( $\beta/\alpha = 488/31$ ), compared to another orbit configuration with almost similar gap evolution pattern (scenario 1.15) for 32-day recovery of maximum degree 90. No tidal error is considered for the simulation.

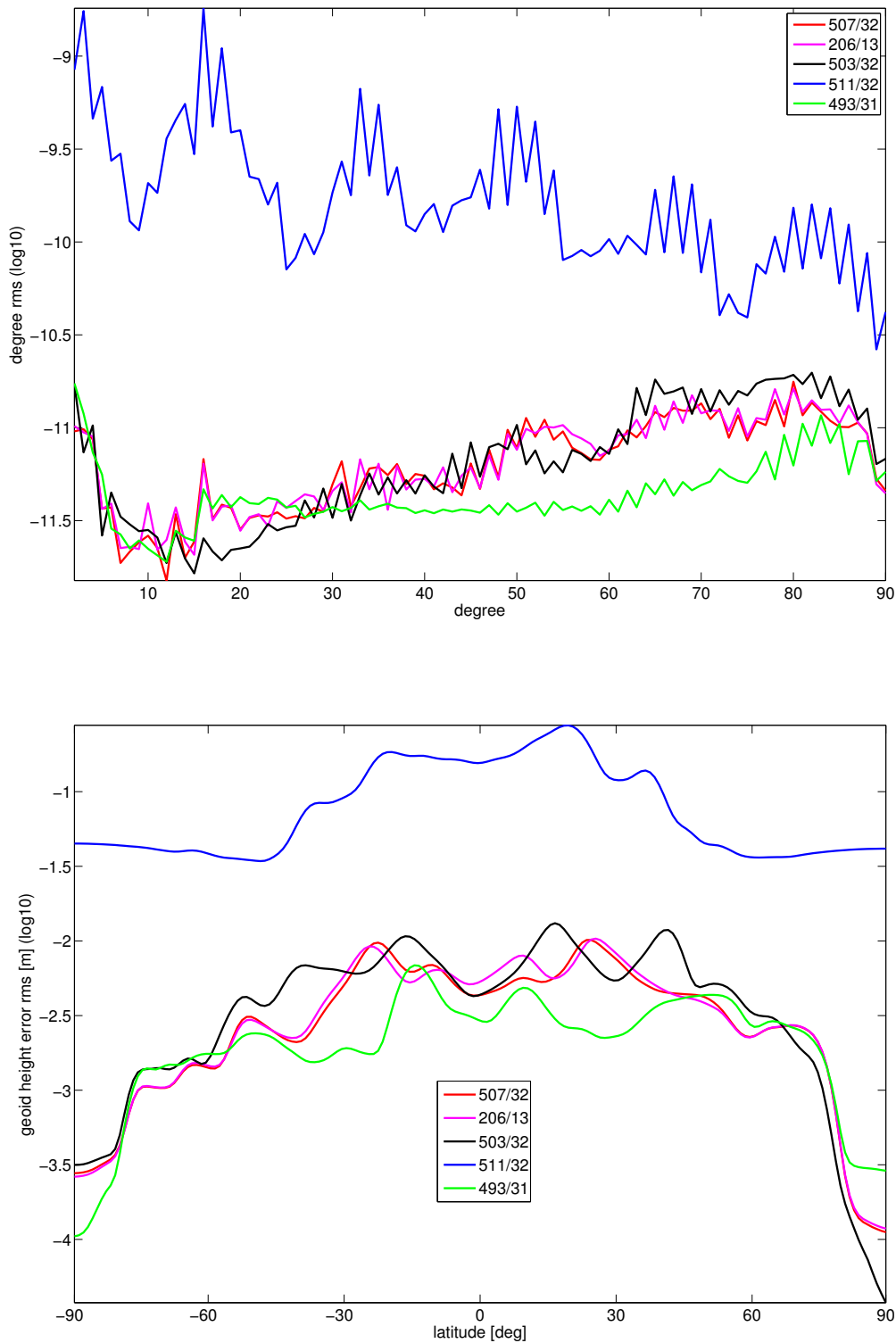


Figure 6.6: Degree rms of the errors (top) and geoid height error rms per latitude (bottom) of the 6-day recoveries by some GRACE-like configurations from Table 5.1. The recoveries are solved for maximum degree 90.

Table 6.2: Global geoid height error rms for 6 and 32-days recoveries of GRACE-like and alternative formation flights of Table 5.2 for maximum degree 90.

scenario	error [mm]	
	6-day	32-day
GRACE-like	6.9	1.7
GFO	3.0	1.3
Pendulum	0.9	0.5
Cartwheel (polar-radial)	1.8	0.4
Cartwheel (equatorial-radial)	0.9	0.3

### Alternative Formation Flights

Several previous studies (e.g. Sharifi et al., 2007; Wiese et al., 2009; Elsaka, 2010; ESA, 2011) show that quality of the gravity recovery by alternative formations which also measure other components than only the along-track GRACE measurement is improved. Table 6.2 shows the improvements of global geoid height error rms for 6-day and 32-day solutions by alternative formation flights of the assumed reference orbit  $\beta/\alpha = 503/32$  of Table 5.2. It can be also seen that the improvement is significant for the 6-day recoveries, where the GRACE Follow-on (GFO) conservative pendulum formation with a small opening angle improves the quality of gravity recovery by more than a factor of two (Table 6.2). That means for the short time gravity solutions, with smaller number of samples, the additional measurement component (rather than the only along-track component of the GRACE-like formation) gets a more important role in the recovery quality. Moreover, Figure 6.7 implies noticeable improvements for 6-day recovery by Pendulum and equatorial-radial Cartwheel for lower latitudes, while the polar-radial Cartwheel shows some improvement for higher latitudes between approximately  $40^\circ$  and  $80^\circ$ . For the 32-day recovery, the performances of polar-radial and equatorial-radial Cartwheel formations are almost the same (Figure 6.8). The improvement for equatorial-radial Cartwheel over the polar-radial Cartwheel for 6-day solution is expected, since the more sensitive radial component get samples over the large equator area. That should be compared with small polar region with dense satellite sampling. However, for 32-day solution, this improvement is not significant. That is because the latitudes of pure radial or pure along-track components (at pole or equator) change over time (perigee drift of approximately  $4^\circ$ ).

### Double Inline Satellite Missions

Bender et al. (2008) show that the spatial-temporal resolution of the gravity recoveries for time-variable gravity field can be improved by employing two pairs of inline formations, when one is in a near-polar orbit and the other in a lower inclined orbit.

One should also think of a revised Colombo-Nyquist rule for two pairs of satellite missions, if the number of revolutions by both satellite pairs is taken into account. That means the number of satellite pairs' revolutions are summed up to result in the total number of scenario revolutions in specific time interval:

$$B = B_1 + B_2 \approx L_{\max} \text{ or } B = B_1 + B_2 \approx M_{\max} \quad (6.4)$$

where  $B_1$  and  $B_2$  stand for the number of revolutions of satellite pairs 1 and 2.

Figure 6.9 shows a significant error drop for all scenarios of Table 5.3 for 3-day recoveries of maximum SH degree 90. Moreover, comparing the errors of 3-day recoveries of two pairs of satellite missions of Table 6.3 with 6-day recoveries of the single inline satellite configurations

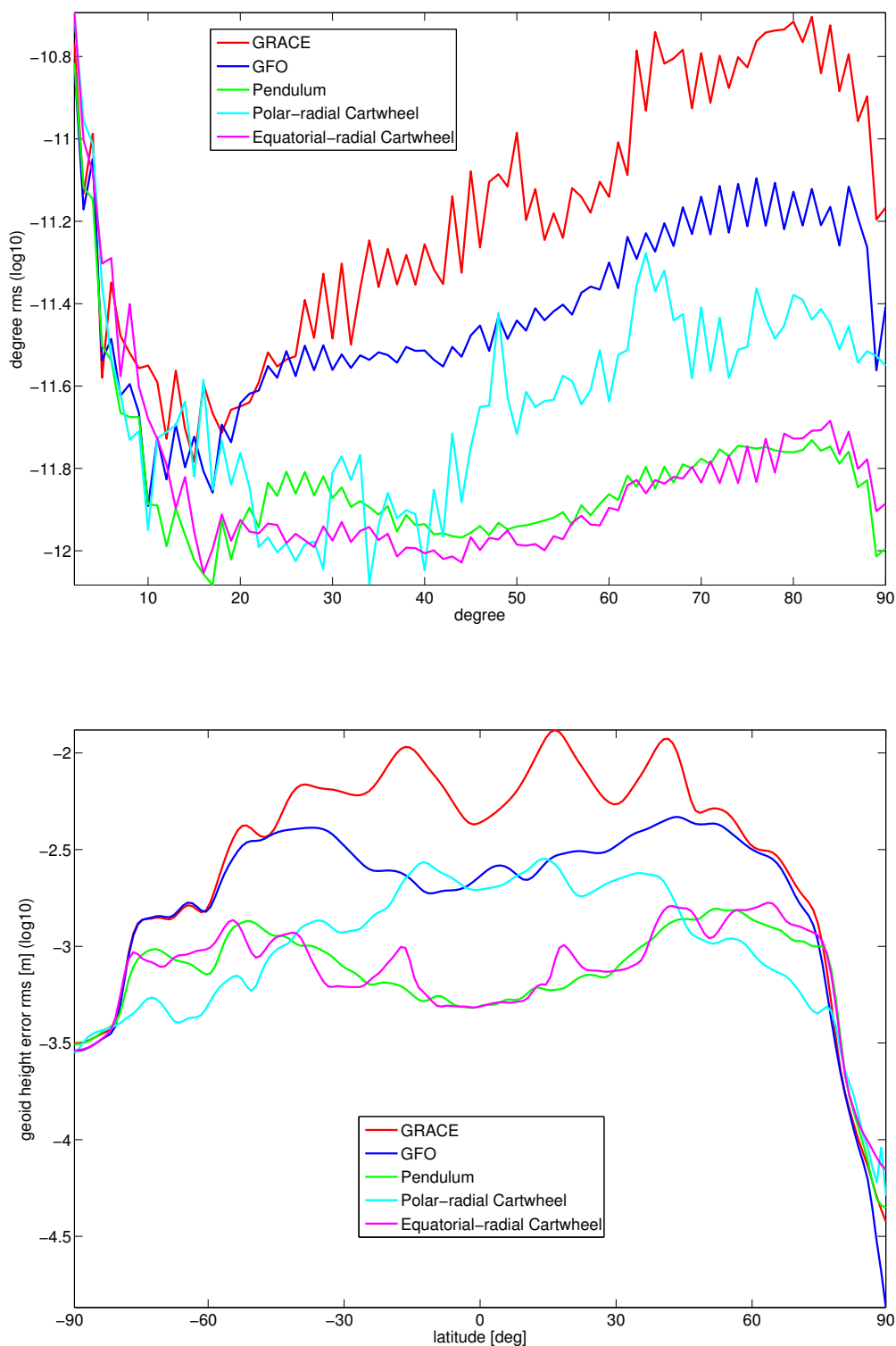


Figure 6.7: Degree rms of the errors (top) and geoid height error rms per latitude (bottom) of the 6-day recoveries by a GRACE-like and alternative formation flights from Table 5.2 for maximum degree 90.

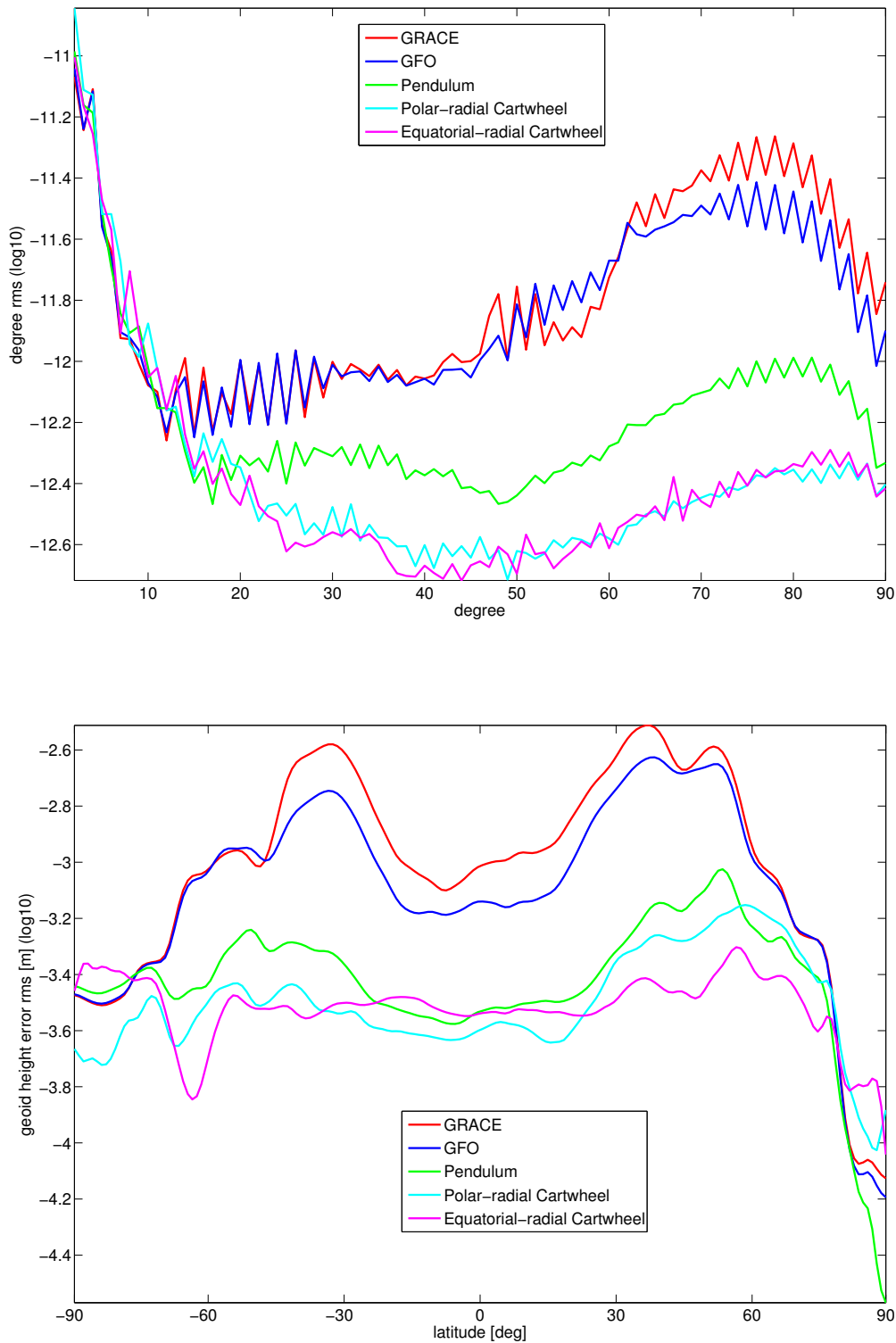


Figure 6.8: Degree rms of the errors (top) and geoid height error rms per latitude (bottom) of the 32-day recoveries by a GRACE-like and alternative formation flights from Table 5.2 for maximum degree 90.

of Table 6.1 (with almost same mission altitudes of two pairs missions), shows a quality improvement of 5 to 10 times for the 3-day recoveries of dual inline missions. The reason, most likely, is the inclined satellite pair which simply adds East-West measurement sensitivity to the North-South component of the near-polar formation which not only doubles the amount of measurements, but also improves the isotropy. Furthermore, the 3-day recoveries suffer less from temporal aliasing of the input time-variable gravity fields of simulations. That means the 3-day gravity solutions also benefit from twice higher time resolution than the 6-day solutions. Comparisons of the 6-day recoveries of single inline satellite mission scenarios and dual pairs missions implies at least 10 times improvements when employing double pairs. Obviously, the improvement depends on the altitude and repeat orbits of the single inline satellite mission scenarios.

Table 6.3 also shows that the quality improvement of dual pairs satellite mission scenarios for 3-day recoveries depend on the missions altitudes. According to the table, scenarios 2.5 – 2.8 benefit from lower altitudes, which provide higher quality of gravity recoveries. However, that is not the case for the 6 and 32-days recoveries, where no improvement is seen in the accuracy level of the Table, i.e. the repeat orbits of Table 6.3 show similar global errors for the 6 and the 32-days recoveries, independent from repeat orbit and altitude of the formations. For the 3-day recoveries, the second category (scenarios 2.5 – 2.8) displays approximately half the error size of the first category (scenarios 2.1 – 2.4) with higher altitudes, but no significant error difference can be observed inside the two categories for the 3-day solutions. As an example Figure 6.10 illustrates the similar quality performance for 3-day gravity solution of scenarios 2.5 – 2.9. This implies that the performance of the formations for the 3-day solutions is almost independent from the repeat patterns, although more investigations should be addressed within the combinations of different repeat modes, esp. those of drifting and slow gap fill-in orbits.

**Polar-gap scenarios** It is also of great interest to investigate the effect of denser sampling of the gravity field in the lower latitudes on the gravity recoveries by low-inclination scenarios. A scenario of two satellite missions, neither of them a polar orbit, causes a polar gap in Earth coverage by the satellites' ground-track patterns, and at the same time sample the lower latitudes denser. As examples, two mission scenarios 2.10 and 2.11 of Table 5.3 with respectively  $15^\circ$  and  $7^\circ$  polar gap radii are studied here. Figure 6.11 illustrates the ground-track pattern of scenario 2.10 for a selected part on the Earth as an example. The latitude-dependent geoid height error rms of these two scenarios are illustrated in Figure 6.12, where they are also compared with the error of scenario 2.9 with only  $0.5^\circ$  polar gap radius. For scenario 2.10 ( $15^\circ$  polar gap radius), the figure does not show improvement in low latitudes for a 3-day recovery, while the quality of the 6-day recovery is very poor in those latitudes. For scenario 2.11, where a Sun-synchronous orbit ( $I = 97^\circ$ ) with a polar gap radius of  $7^\circ$  is employed, some improvements in high latitudes can be seen. This is just below a colatitude of  $7^\circ$  where the quality significantly drops. That means the  $7^\circ$  gap in polar areas does not affect the spherical harmonics associated with other areas very much. Therefore, the scenarios with small polar gap radii can be considered as options for future satellite missions, where the poor quality of polar gap area can be dealt by e.g. regularization methods. It is also important to note that the maximum degree of recoveries has an important effect on the quality of recoveries in the lower latitudes. In fact, the gravity solution of high SH degrees suffer more from the polar gap in the satellite coverage than the recoveries of low SH degrees.

Table 6.3: Global geoid height error rms s for 3, 6 and 32-days recoveries of dual pairs of inline satellite missions of Table 5.3 for maximum degree 90. ( $\Delta\Omega = 180^\circ$ )

scenario	formation	inclination [deg.]	$\beta/\alpha$ [rev./days]	altitude [km]	error [mm]		
					3-day	6-day	32-day
2.1	Inline	89.5	503/32	333.8	0.8	0.4	0.2
	Inline	72	503/32	305.0			
2.2	Inline	89.5	125/8	360.7	0.9	0.4	0.2
	Inline	72	503/32	305.0			
2.3	Inline	89.5	503/32	333.8	1.1	0.4	0.2
	Inline	72	125/8	332.1			
2.4	Inline	89.5	125/8	360.7	1.2	0.4	0.2
	Inline	72	125/8	332.1			
2.5	Inline	89.5	507/32	298.4	0.5	0.4	0.2
	Inline	72	488/31	298.3			
2.6	Inline	89.5	142/9	317.0	0.6	0.4	0.2
	Inline	72	488/31	298.3			
2.7	Inline	89.5	507/32	298.4	0.5	0.4	0.2
	Inline	72	110/7	306.2			
2.8	Inline	89.5	142/9	317.0	0.5	0.4	0.2
	Inline	72	110/7	306.2			
2.9	Inline	89.5	206/13	297.6	0.6	0.4	0.2
	Inline	72	205/13	290.4			

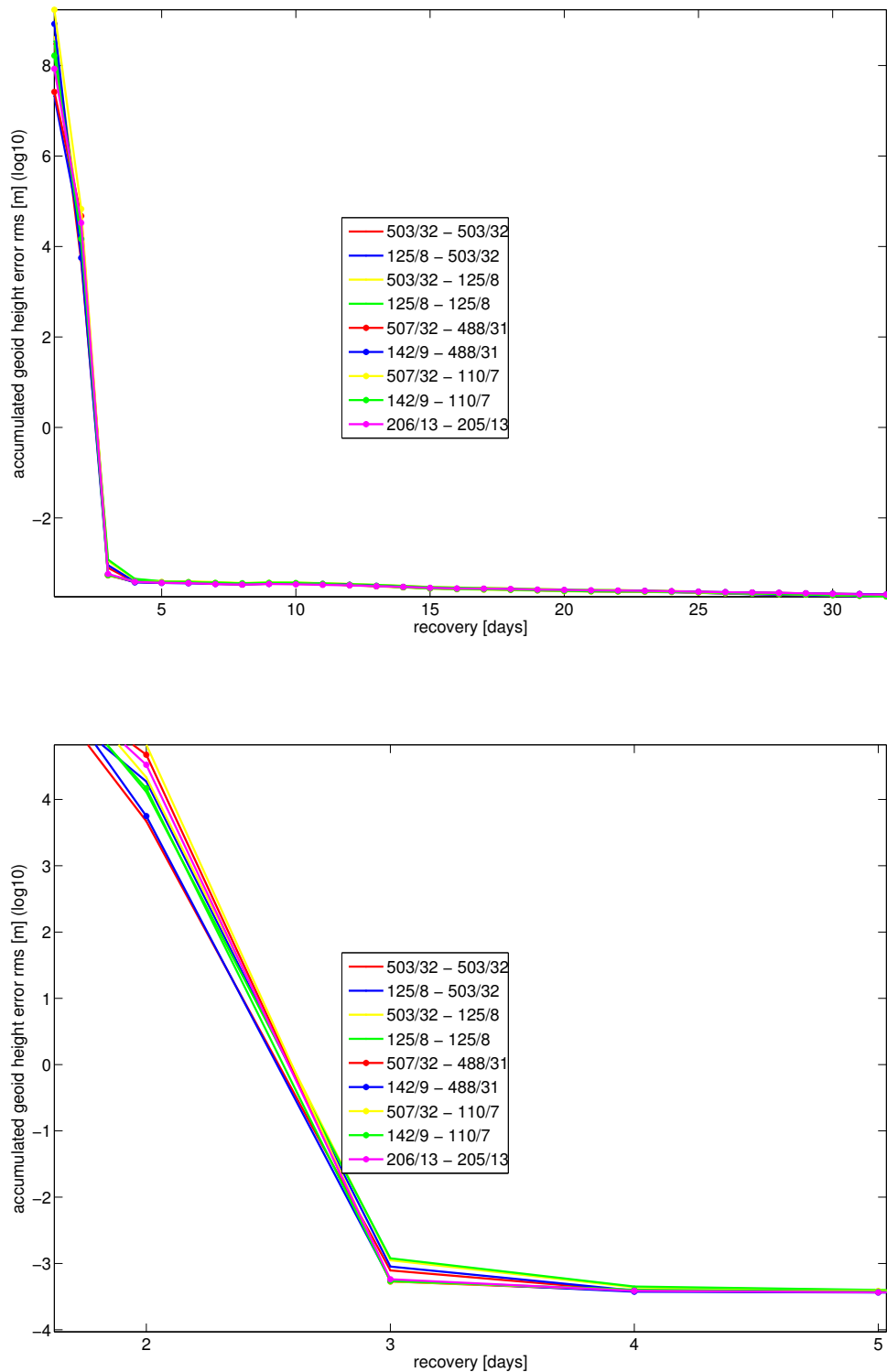


Figure 6.9: Global geoid height error rms of two inline satellite missions scenarios of Table 5.3 for recoveries up to maximum degree 90. The bottom graph is a zoom-in view of the top figure for 2, 3, 4 and 5-days recoveries.

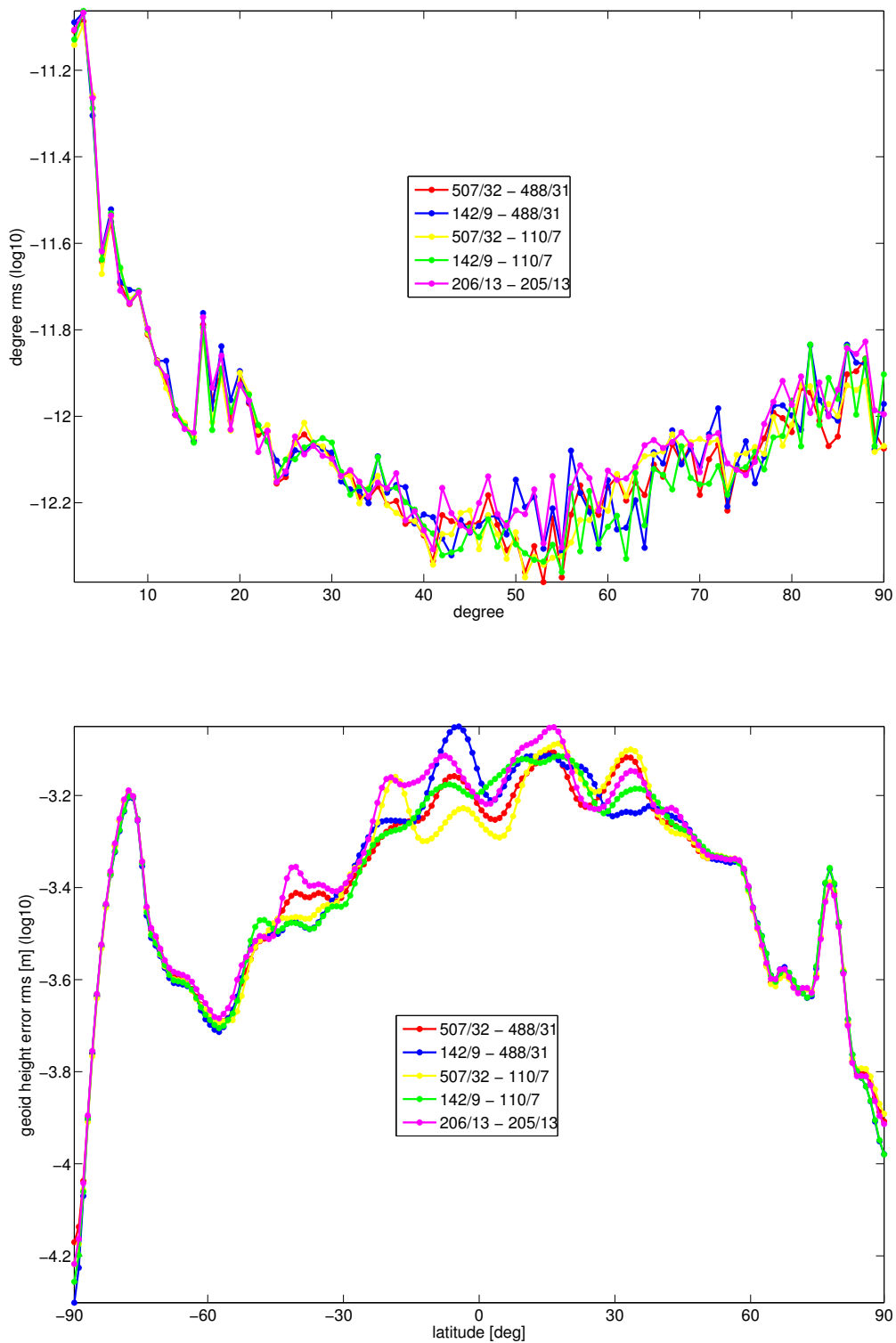


Figure 6.10: Degree rms of the errors (top) and geoid height error rms per latitude (bottom) of the 3-day recoveries by some examples of two pairs of inline satellite missions from Table 5.3 for maximum degree 90.

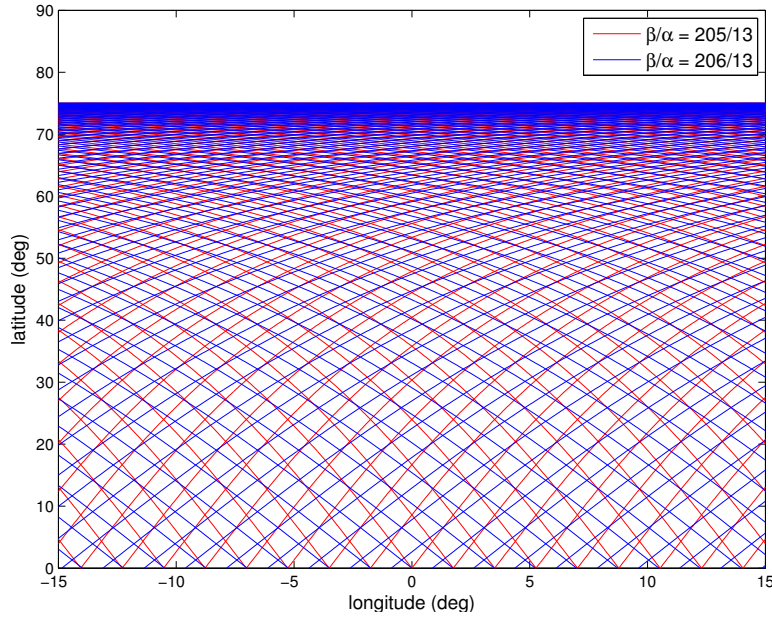


Figure 6.11: A selected part of ground-track pattern of scenario 2.10 with  $15^\circ$  polar gap radius.

### 6.1.2 Effect of White Noise on the Recovery Quality

Besides the aliasing effects of time-variable gravity signals, the measurement noise of the intersatellite link and the accelerometers play an important role for the gravity field accuracy. For the GRACE mission, the sensor noise is one of the most dominant error sources (Loomis et al., 2011). However, future ll-SST missions will benefit from enhanced technology as e.g. laser-link and drag-free system (Mueller et al., 2005; St Rock et al., 2006; Alnis et al., 2008; Pierce et al., 2008; Marchetti et al., 2008; Loomis et al., 2011; ESA, 2011) which aim to reduce the sensor noise significantly by one or two orders of magnitude. Then, aliasing will be the most severe error source, at least if the state-of-the-art background model errors are considered, which are the limiting problem of de-aliasing products.

Nevertheless, it is worth to study the effect of measurement noise on future mission options. Here, a simple white noise model with a power spectral density (PSD) of  $10^{-10} \text{ m s}^{-2}/\sqrt{\text{Hz}}$  on the level of range accelerations, applied in the quick-look-tool, is introduced. This corresponds to a mean level over the measurement bandwidth of realistic instrument scenarios, mentioned in ESA (2011) and Sheard et al. (2012).

Table 6.4 summarizes the effect of white noise in terms of global geoid height error rms for different time-interval recoveries of inline, alternative and dual pair formation flights. Although a significant improvement can be seen by employing alternative formations rather than GRACE-like mission, the table shows very small values compared to the global geoid height error rms by geophysical models of Table 6.2. In addition, the error improvement by long time interval recovery of inline mission, compared to 6-day recovery, is shown in Table 6.4. That is also seen for two pairs of satellite missions, where the 6-day recovery produces smaller error, compared to 3-day recovery. Furthermore, a significant improvement of order 5 is realized for white noise effect by employing two pairs of inline satellite missions rather than only a single inline mission, even when the gravity is solved for short time interval of 3-day rather than 6-day.

Figures 6.13, 6.14 and 6.15 illustrate the effect of white noise on the spherical harmonics spectrum of

## 6.1 Quality of the Gravity Field Recoveries

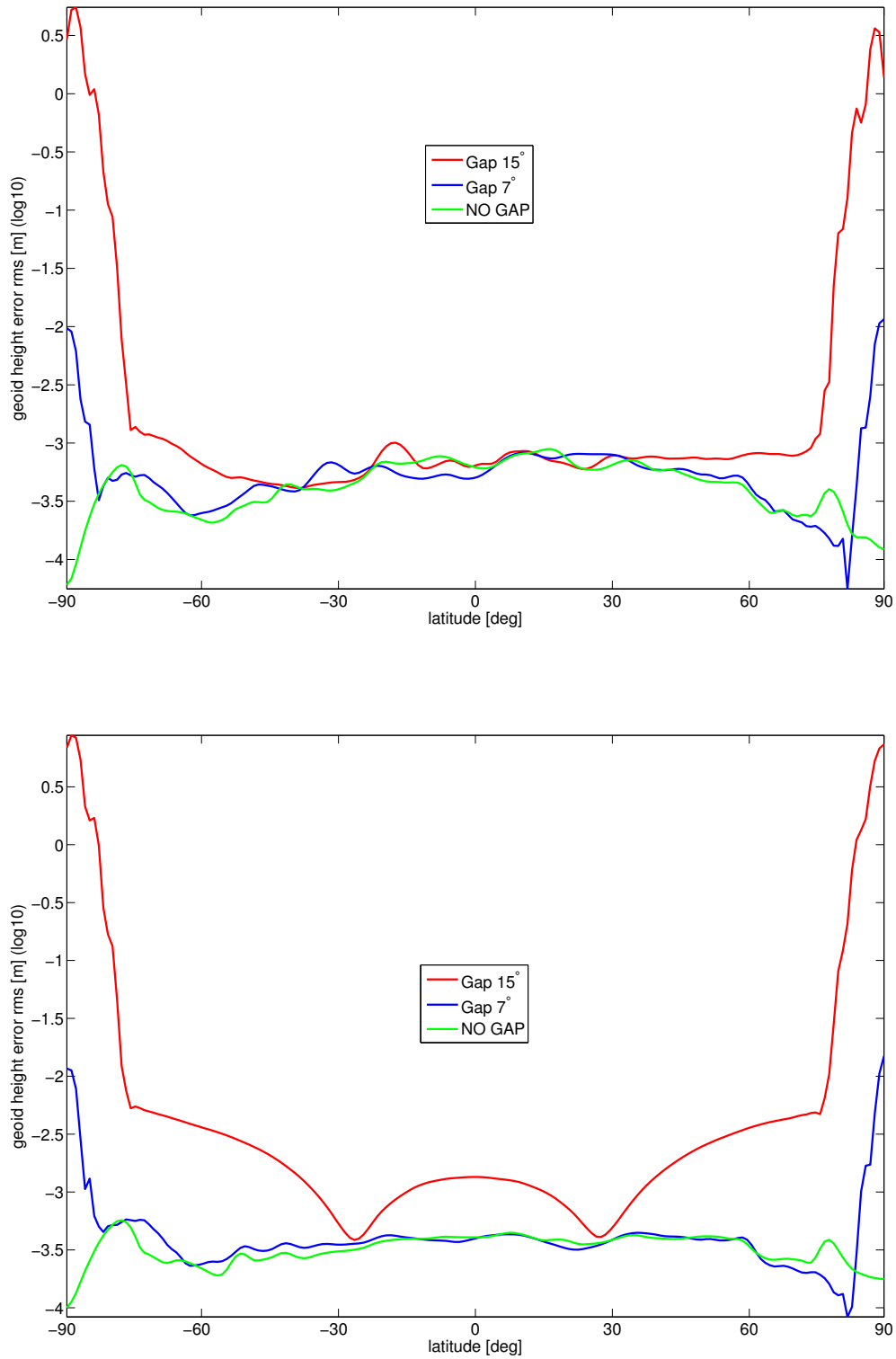


Figure 6.12: Geoid height error rms per latitude of the 3-day (top) and 6-day (bottom) recoveries by two pairs of inline satellite missions scenarios 2.9, 2.10 and 2.11 from Table 5.3 with respectively  $0.5^\circ$ ,  $15^\circ$  and  $7^\circ$  polar gap radii. The recoveries are solved to maximum degree 90.

Table 6.4: The white noise effect in terms of global geoid height error rms for different time-interval recoveries of GRACE-like, alternative and dual inline missions of Table 5.2 and scenario 2.2 of Table 5.3 for maximum degree 90.

scenario	error [mm]		
	3-day	6-day	32-day
GRACE-like	-	0.27	0.03
GFO	-	0.07	-
Pendulum	-	0.02	-
Cartwheel (polar-radial)	-	0.07	-
Cartwheel (equatorial-radial)	-	0.03	-
Dual pairs of inline missions	0.05	0.01	-

$$e_{lm} = \sqrt{C_{lm}^2 + S_{lm}^2} \quad (6.5)$$

The figures show a considerable error decrease for the harmonics near the sectorial band  $l = m$  for the Pendulum compared to the inline formation, while a clear improvement in this band can even be seen for the conservative pendulum formation of GFO. As expected, the improvement is most significant when two inline satellite pairs are employed. Moreover, for both GRACE-like and two pairs missions, the high degrees and orders of spherical harmonics are less affected by white noise in the long time interval gravity solutions (Figures 6.14 and 6.15).

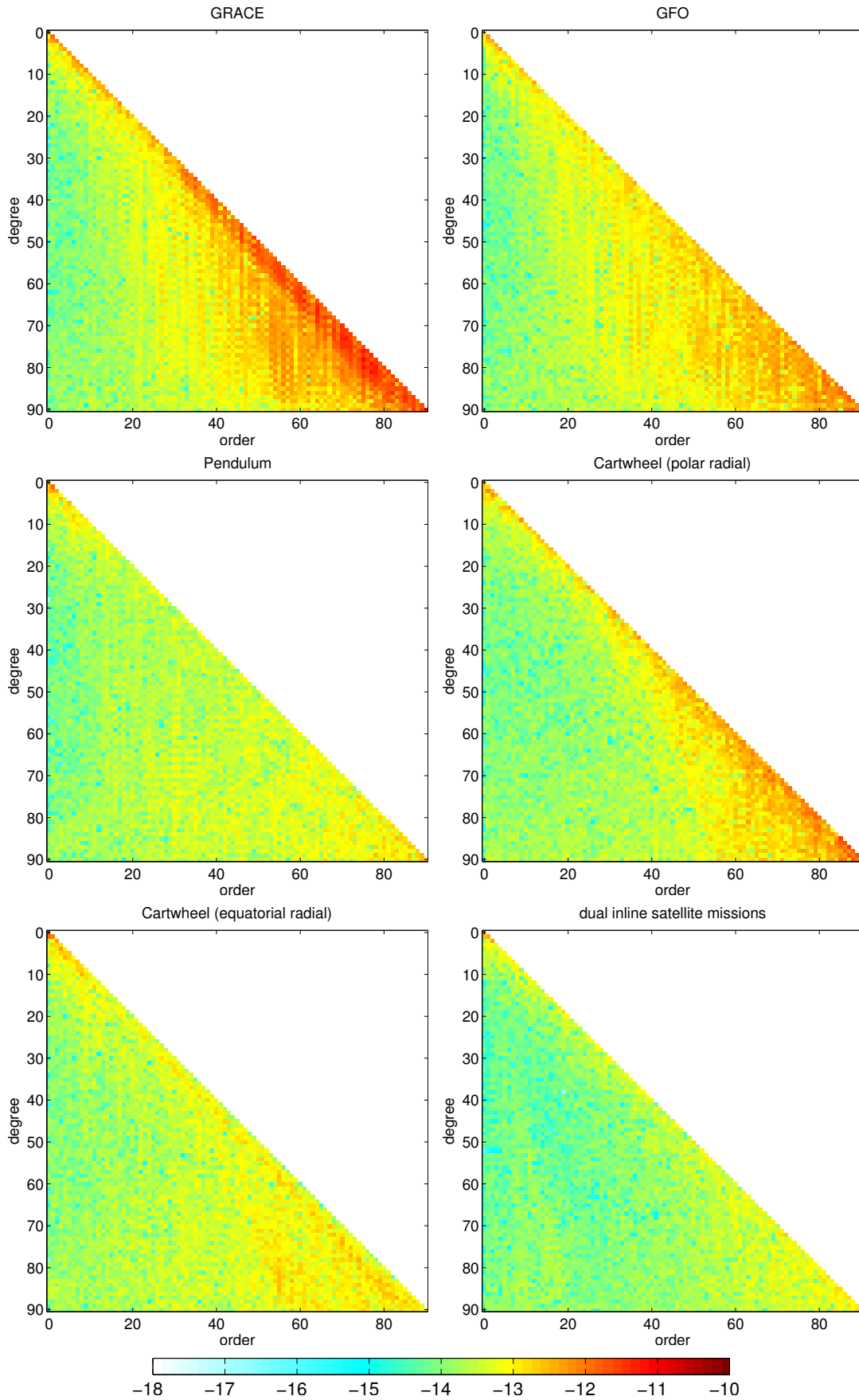


Figure 6.13: SH error spectrum, due to white noise for 6-day recoveries of inline and alternative formation flights of Table 5.2 for maximum degree 90. The coefficients values are in logarithmic scale.

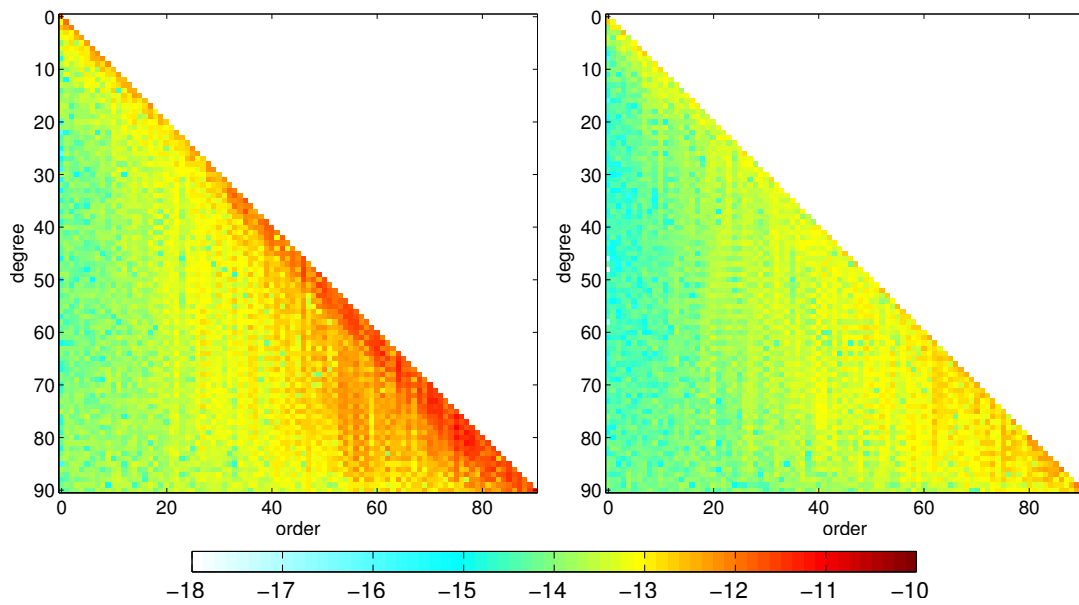


Figure 6.14: SH error spectrum, due to white noise for 6-day (left) and 32-day (right) recoveries of inline formation flight of Table 5.2 for maximum degree 90. The coefficients values are in logarithmic scale.

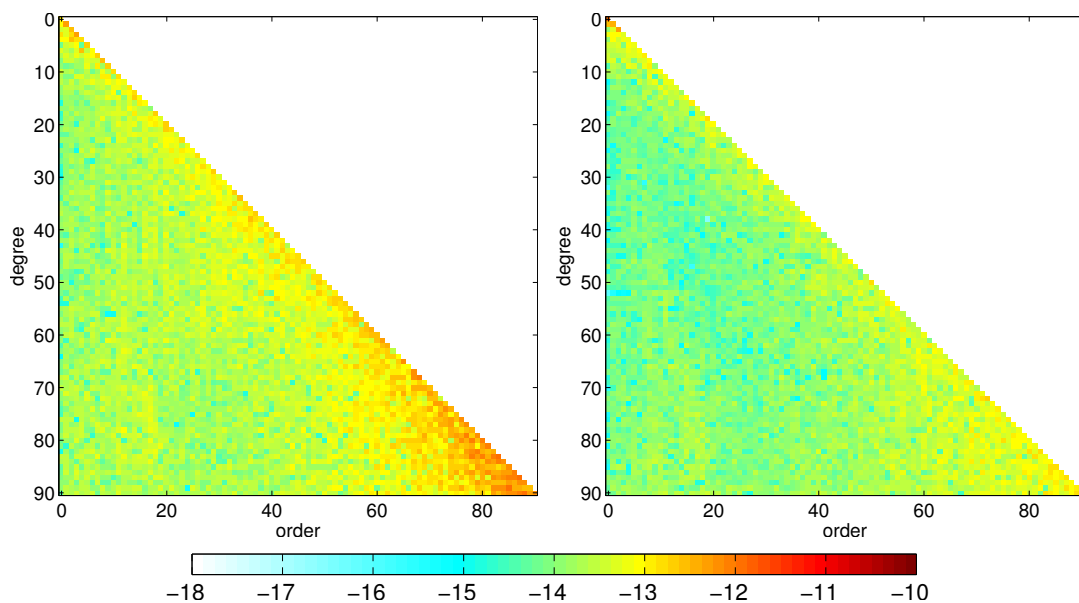


Figure 6.15: SH error spectrum, due to white noise for 3-day (left) and 6-day (right) recoveries of two pairs of inline satellite missions of scenario 2.2 from Table 5.3 for maximum degree 90. The coefficients values are in logarithmic scale.

## 6.2 Error Simulations and Post-processing

The quick-look software of this research study is employed to find optimal orbit configurations and formation flights from the mission scenarios of Tables 5.1, 5.2 and 5.3. The error simulation of the selected scenarios is performed by a simple assumption that 10% of the input geophysical signals (models) is unknown. That means 90% of the true geophysical signals from time-variable gravity fields (AOHIS) are considered as known background model. However, this assumption considers a very simple model for the error simulation which is not realistic, but can still be an appropriate choice for the closed loop simulation of this thesis. It is of great interest to investigate more realistic and sophisticated models' errors in future work. One possibility could be by introducing difference of two models of a same geophysical field as model error of the field (as assumed for ocean tide error of this study).

The simulation and recovery steps of this research study are only performed for 10% of the total signals in addition to the ocean tide error. This part is then called the models' error. Only the retrieved signals (recovery) from the models' errors are subjected to white noise filtering and regularization as the post-processing tools. Furthermore, the correlation tool of this thesis is employed for correlation analysis of the 10% of the geophysical models (AOHIS) as the input of simulation error and the recovery of that 10% as well as the ocean tide error and white noise as the output.

### 6.2.1 Choosing the Optimal Scenarios

Two selection factors play the most important roles in choosing the optimal satellite mission scenarios: (i) the performance of the mission in retrieving the geophysical signals, and (ii) technical and stability issues connected with the mission. From a technical viewpoint, the missions are chosen by the altitude not less than 290 km, while from the view of geodetic sensitivity an orbit height not larger than 320 km is preferable. That is a trade-off between higher sensitivity to short wavelength phenomena by lower altitude and a shorter mission life time due to a larger atmospheric drag force. This decision is due to the expectation that future satellite missions will benefit from drag-free technology like GOCE which allows the mission to fly at lower altitudes (Marchetti et al., 2008; St Rock et al., 2006; Wiese et al., 2011b). Furthermore, an intersatellite distance of 100 km of an inline formation equipped with laser interferometry is chosen as a trade-off between instrument performance and relative accuracy in determining short wavelengths features in the gravity field (Wiese et al., 2009). The stability problem with Pendulum and Cartwheel formations as well as the laser interferometry pointing issue limit the choices to inline formations and conservative Pendulum formations with small opening angle (GFO). However, due to the higher performance of the GFO formation compared to the inline configuration, the GFO would be a favorite scenario for a single pair satellite mission. The scenario is chosen on a repeat orbit of  $\beta/\alpha = 507/32$  which shows a good performance for 6-day recovery (Table 6.1). For dual satellite pairs, two different formation scenarios are selected:

- (i) a combination of a near-polar and an inclined inline missions, and
- (ii) a near-polar GFO formation together with an inclined inline mission.

For both scenarios, the inclination angle of the second pair is considered as  $72^\circ$ . Furthermore, based on the quality assessment of different configurations, scenario 2.5 of Table 6.3 with repeat orbits of  $\beta/\alpha = 507/32$  and  $488/31$  are chosen. These suggestions consider a prediction of launching an independent single near-polar GFO formation as the substitute of the current GRACE in the near future. Therefore, the inclined inline formation can be suggested as add-on to the near-polar mission afterwards. The second pair then improves the quality

Table 6.5: Orbit architectures of our chosen optimal scenarios

scenario	formation	inclination (deg.)	$\beta$ (rev.)	$\alpha$ (days)
7.1	GFO	89.5	507	32
7.2	Inline	89.5	507	32
	Inline	72	488	31
7.3	GFO	89.5	507	32
	Inline	72	488	31

performance of gravity recovery very significantly.

Table 6.5 summarizes the suggested optimal scenarios for the future missions. The 6-day recovery of single pair satellite mission (scenario 7.1) and the 3-day recoveries of two pairs satellite missions (scenarios 7.2 and 7.3) of maximum degree 90 are subjected to the error simulation and post-processing analysis.

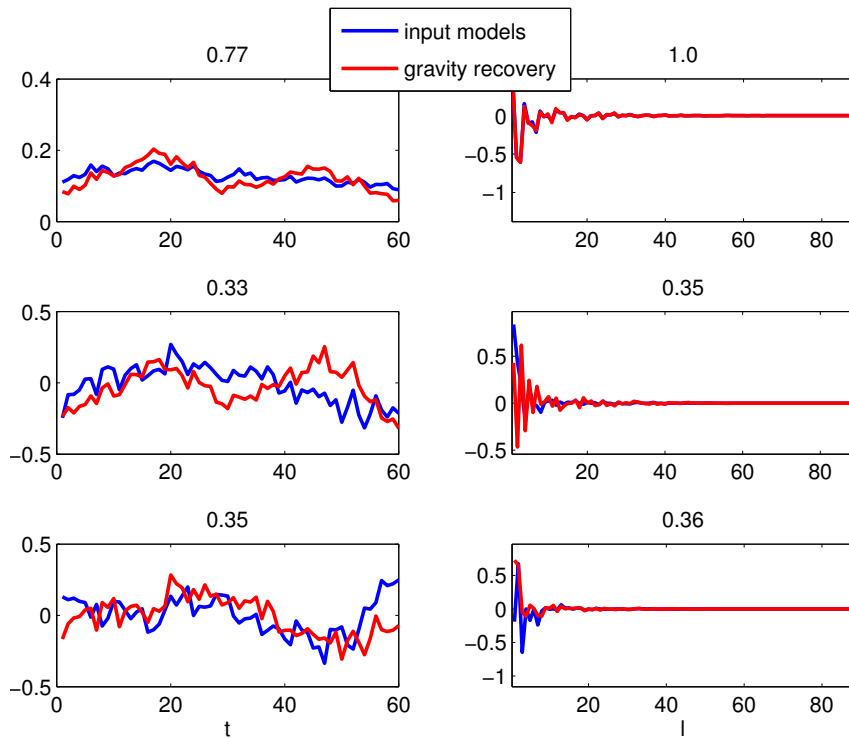
### Correlation Analysis

As discussed in Section 4.4, Empirical Orthogonal Functions (EOF) analysis can be employed as a tool for searching the optimal scenarios. The analysis is especially useful when the mission scenario design pursues specific purposes (e.g. the temporal signatures such as seasonal variations of a geophysical phenomenon). Here, the temporal behavior of the geophysical signals is studied through the modes of principal components of the input and output of the closed loop simulation tool. The possibility of shifting the temporal or spatial signature of a geophysical phenomenon represented by a single mode in one field to another mode in the other field leads the study not only to investigate the correlation of corresponding modes of the two fields, but also to look at the correlation of each mode from one field to all the modes from the other field for a specific order (see Subsection 4.4.4). Examples of the correlation analysis of corresponding modes and the all modes cross-correlation approaches are respectively represented in Figures 6.16 and 6.17.

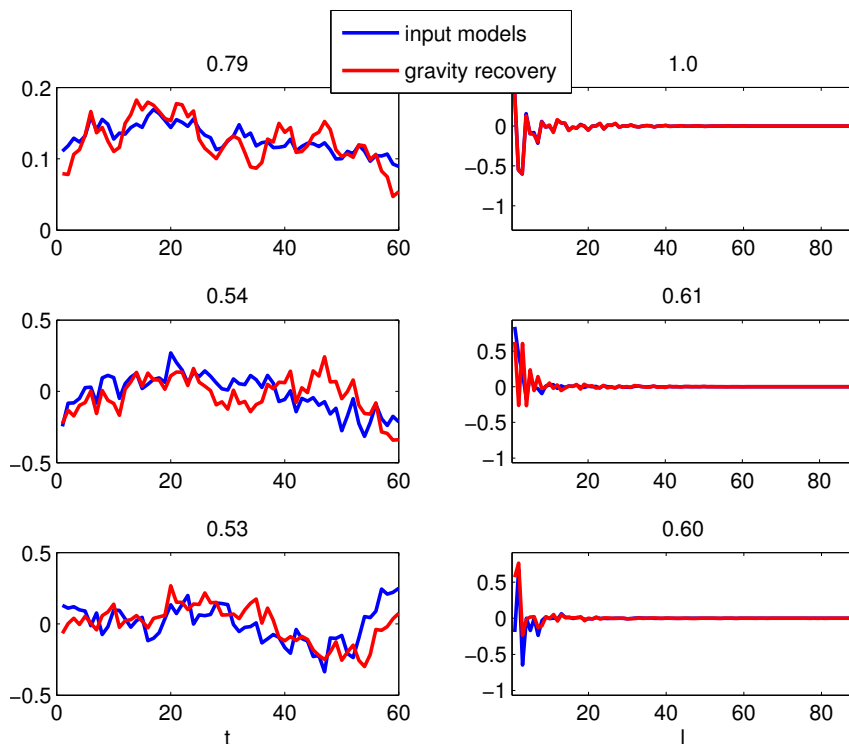
Although, the EOF-based cross-correlation analysis can provide detailed information of the gravity field retrieval processes, the search space of the analysis is extremely vast and requires lots of efforts which is beyond the scope of this study. Clearly, it would not be reasonable to conclude from a correlation analysis of limited number of modes and orders. As an example, Figures 6.16 and 6.17 show that despite the small improvement by employing two pairs satellite missions compare to single pair formation flight for the first three modes of order  $m = 0$  (Figure 6.16), no general improvement for cross-correlation of all the modes can be seen (Figure 6.17). However, as mentioned above, this sort of correlation analysis might be more helpful when it is used for investigating specific features, recovered by different mission scenarios. For general selection procedure of the optimal scenarios of this thesis, the analysis is not very helpful, and therefore has not been employed.

### 6.2.2 Noise Filtering

Dealing with noise is one of the most challenging issues when higher recovery quality is looked for. The noise has different sources. Three of the most important noise sources are



(a) one pair



(b) two pairs

Figure 6.16: The first three temporal (left) and spatial (right) modes of the input field (blue line) and the recovery (red line) of 6-day for single pair (a) and two pairs (b) of inline satellite missions for zonal coefficients for a one year time series (2005). The correlation coefficients between the two fields are provided at the top of each figure. Please note that the temporal modes are shown in the time scale of almost one year ( $60 \times 6$ -day solutions), while the spatial modes are calculated for maximum degree 90.

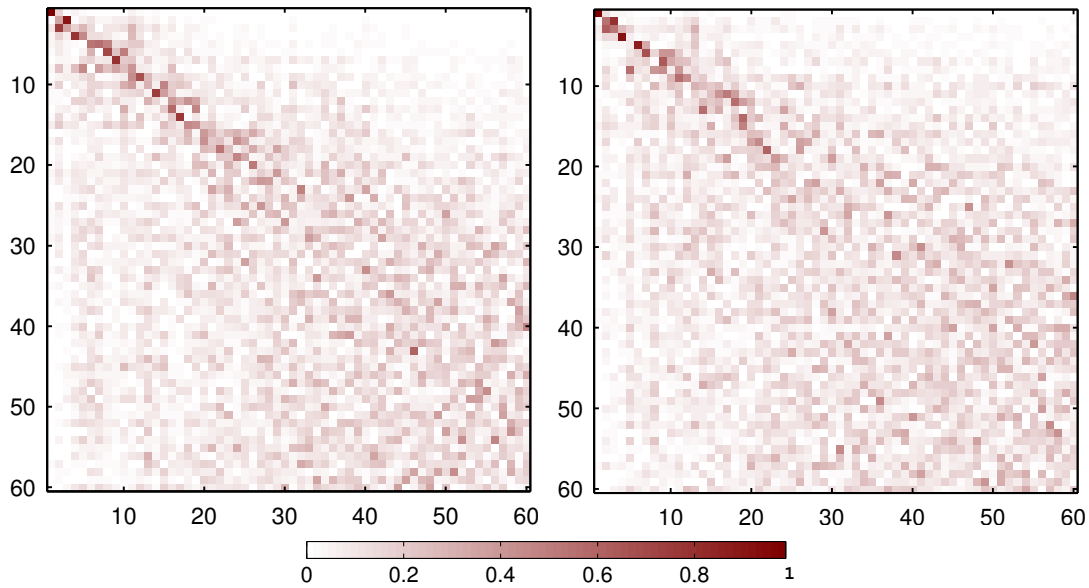


Figure 6.17: The correlation coefficients between temporal modes (principal components) of the input field and the recovery of 6-day for single pair (left) and two pairs (right) of inline satellite missions for zonal coefficients for a one year time series (2005).

- (i) aliasing errors which are due to under-sampling the signals,
- (ii) retrieval errors which are caused by the formation architecture (for example the North-South stripes in GRACE recoveries), and
- (iii) the instruments noise.

Several filter strategies have been suggested to deal with these errors. As it was discussed in 4.4.3, Wouters and Schrama (2007) proposed a filter based on Empirical Orthogonal Functions (EOF) analysis in combination with Kolmogorov-Smirnov white-noise test (KS-Test) on the data time series in the spectral domain. Moreover, Koch and Kusche (2002) and Lorenz (2009) provided regularization methods to deal with both white and colored noise. These two filters are employed here to minimize the effect of noise on the gravity recoveries.

### EOF+KS-Test Filter

Based on Equation (4.32), a left filter operator is utilized for the white noise filtering through EOF+KS-Test analysis (Iran Pour and Sneeuw, 2012). An example of such filter for four specific orders is shown in Figure 6.18. Figures 6.19 and 6.20 illustrate how the filter works on the spherical harmonic coefficients and EWH maps for the selected optimal scenarios. Figure 6.19 shows the error spectrum of the recoveries of 10% of geophysical models as well as tidal error and white noise before and after filtering. The corresponding EWH maps of those products are illustrated in Figure 6.20. The signal energy percentage of accepted modes for each order for 6-day solution of scenario 7.1 is shown in Figure 6.21, where the energy percentage is computed through the summation of the variances of PCs  $a_j$  passing the KS-Test normalized by the sum of variances of all PCs  $a_j$  (Wouters and Schrama, 2007).

Table 6.6 provides improvement of the global geoid height error rms values after filtering. Obviously, the strength of the designed filter depends on the significance level,  $\alpha$ , of the KS-Test in white noise detection. The filter does not differentiate between the noise and the real

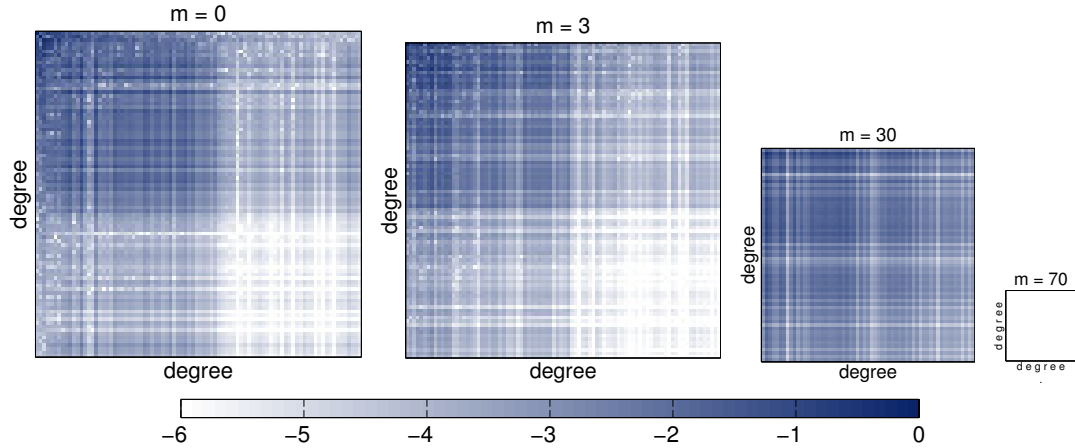


Figure 6.18: The EOF filter operator  $F_u$  of 6-day solution of scenario 7.1 for  $C_{lm}$  orders  $m = 0, 3, 30$  and  $70$  ( $\alpha = 0.05$ ) with  $l \geq m$ . The color-bar is in logarithmic scale.

Table 6.6: Improvement of global geoid height error rms by EOF+KS-Test filter for significance level,  $\alpha = 0.05$ .

scenario	global geoid height error rms [mm]	
	before filtering	after filtering
7.1	0.7	0.3
7.2	0.3	0.2
7.3	0.3	0.2

geophysical signals with the global power density smaller than KS-Test threshold level. For example, Figure 6.19 shows that all the modes of the majority of high orders are recognized as white noise and then filtered out by the KS-Test. That, obviously, does not reflect the truth. Therefore, it would be almost impossible to remove all the white noise without diminishing some of the real signals. It is indeed a very difficult task to find an optimal significance level of the KS-Test for white noise filtering, while the real signals of interest are kept. Examples of the effect of three different significance level values on SH spectrum and EWH maps of 6-day recovery of scenario 7.1 are respectively illustrated in Figures 6.22 and 6.23.

### Regularization

A regularization method by Koch and Kusche (2002) and Lorenz (2009) (see the discussion in Subsection 4.3.2) is employed to deal with both white and colored noise. When the aim is to reestimate a set of spherical harmonic coefficients in terms of sequential estimation, Equation (4.20) can be rewritten as a spectral filter. Therefore, design matrix  $A$  becomes the identity matrix, observation vector  $y$  becomes  $\hat{x}$  and  $\hat{x}$  changes to  $\hat{x}'$

$$\hat{x}' = (P + \lambda P_K)^{-1} P \hat{x} \quad (6.6)$$

where  $x_0 = 0$ . The equation can also be written in form of filter operator  $F_{\text{reg}}$ :

$$\hat{x}' = F_{\text{reg}} \hat{x} \quad (6.7)$$

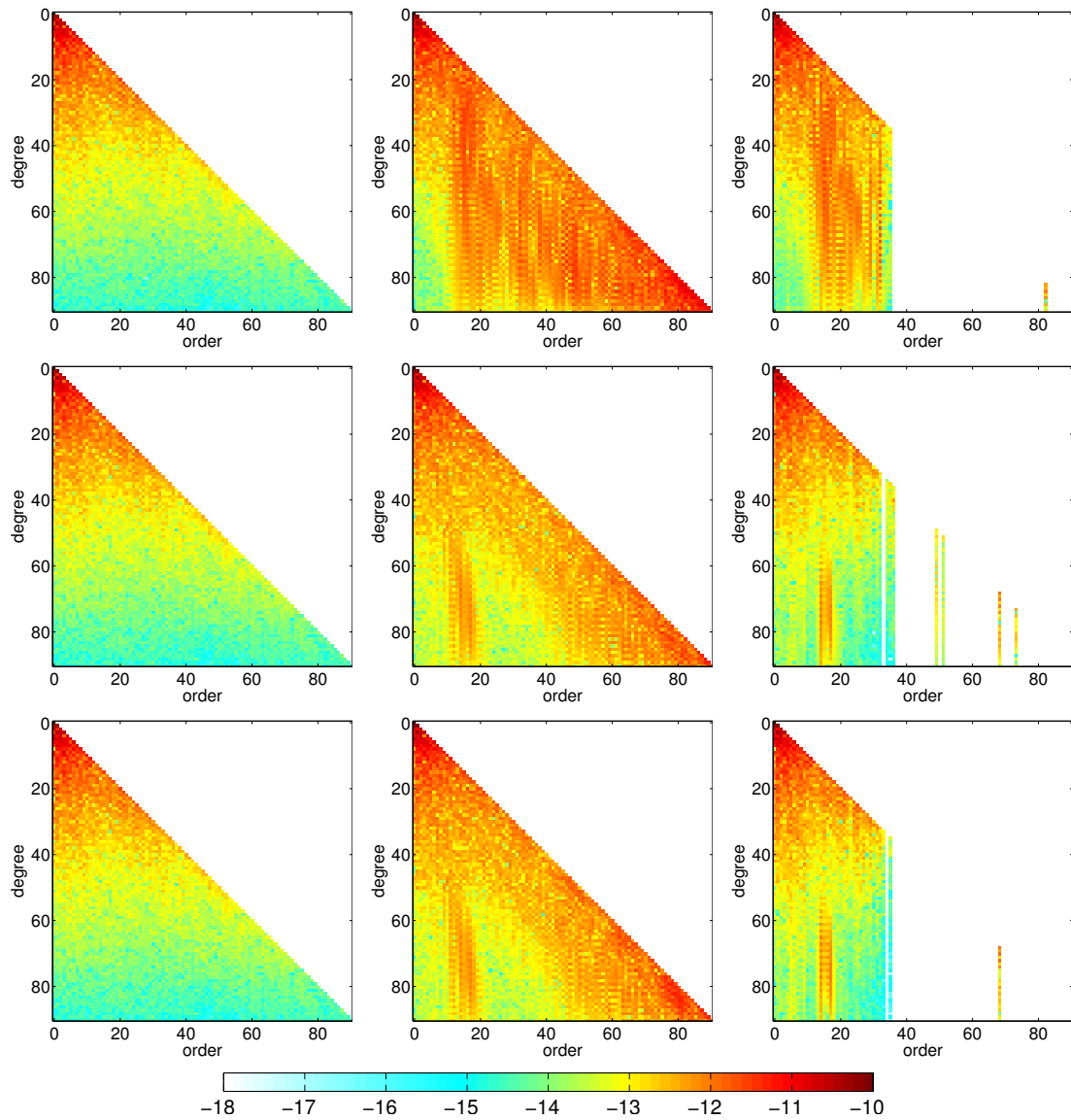


Figure 6.19: Spherical harmonic coefficients of mean input signals (left) and the recoveries before (middle) and after (right) EOF+KS-Test filtering for a 6-day recovery of scenario 7.1 (top) and 3-day recoveries of scenarios 7.2 (middle) and 7.3 (bottom) for maximum degree 90. The significance level,  $\alpha$ , for KS-Test is set to 0.05. The coefficients values are in logarithmic scale.

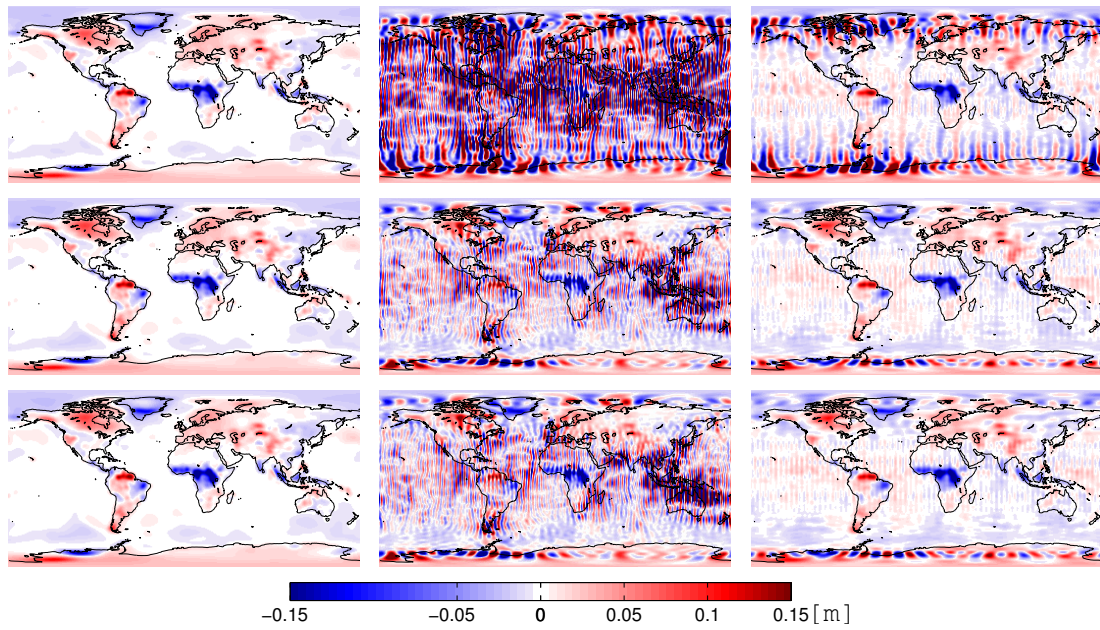


Figure 6.20: Corresponding EWH maps of Figure 6.19

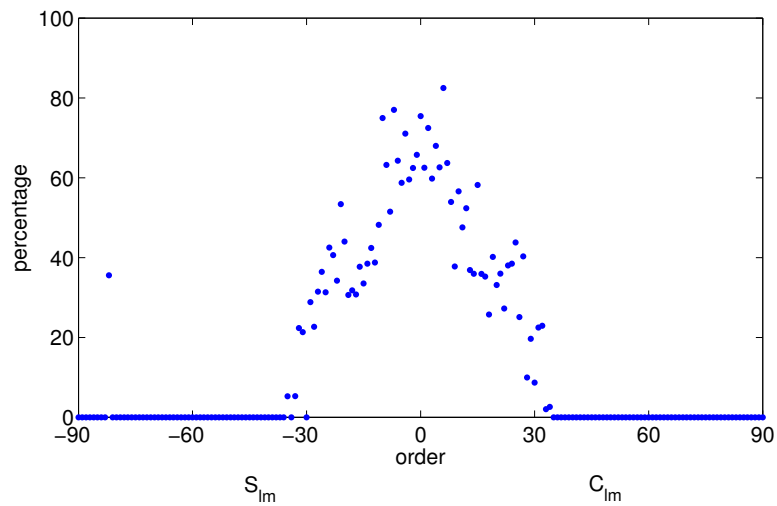


Figure 6.21: The signal energy pass of  $C_{lm}$  and  $S_{lm}$  by the KS-Test of 6-day solution of scenario 7.1 ( $\alpha = 0.05$ )

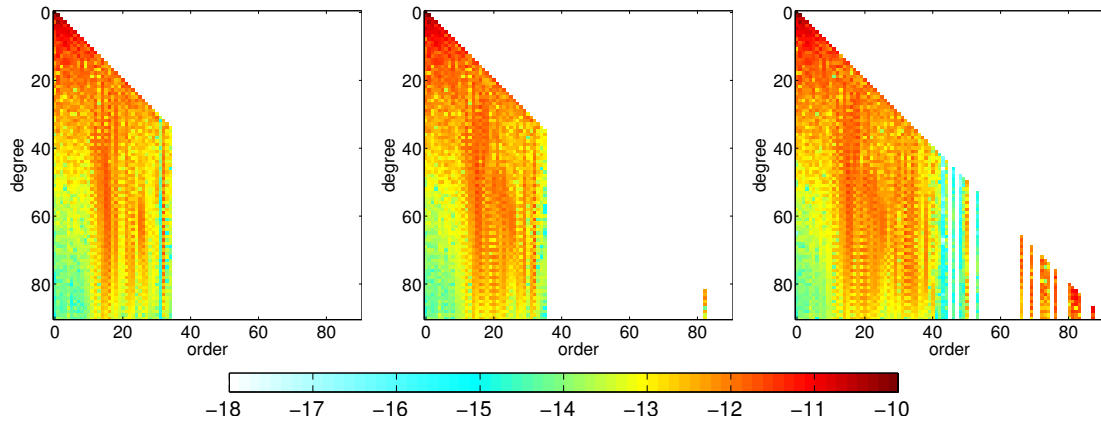


Figure 6.22: Effect of different significance level of EOF+KS-Test filter,  $\alpha$ , on SH spectrum of 6-day solution of scenario 7.1:  $\alpha = 0.01$  (left),  $\alpha = 0.05$  (middle) and  $\alpha = 0.25$  (right). The coefficients values are in logarithmic scale.

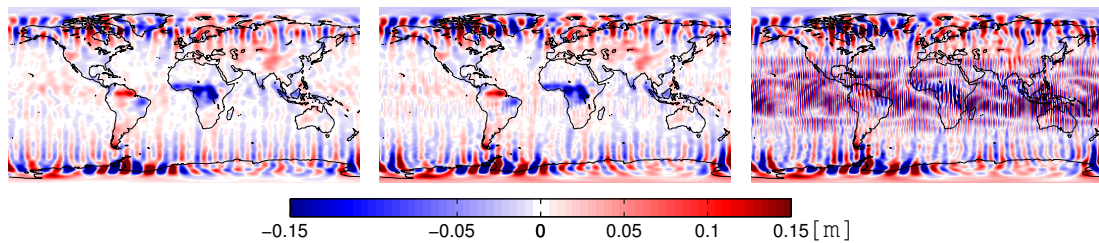


Figure 6.23: Corresponding EWH maps of Figure 6.22.

with  $F_{\text{reg}} = (P + \lambda P_K)^{-1} P$  which has the structure of the Wiener filter (Sasgen et al., 2006; Lorenz, 2009). An example of such filter for 6-day recovery of scenario 7.1 with regularization parameter  $\lambda = 5$  is illustrated in Figure 6.24.

In this study, the regularization method is utilized for processing of the recoveries of selected optimal scenarios (Figures 6.25 and 6.26). The optimal regularization parameter,  $\lambda$ , of Equation (4.18) is chosen with a criterion of having minimum distance of degree rms between 10% of the input models (AOHIS) and the recovery of that 10% when the ocean tide error and white noise are added as well. Similar to the significance level concept in EOF+KS-Test filtering, the regularization parameter plays an important role here. Figures 6.27 and 6.28 show the effect of three different values of  $\lambda$  on the SH spectrum and EWH maps. As it is seen, the small value of regularization parameter ( $\lambda = 0.01$ ) fails to handle the main part of noise, while its large value ( $\lambda = 100$ ) diminish many real signals. Furthermore, concerning the procedure of search for optimal regularization parameter (here  $\lambda = 5$ ), it is important to notice that forcing the degree rms of the recovery to the degree rms of the input models may remove the unknown signals of the recoveries and therefore smooths the results towards the input models as the true models. However, since the true models in reality are not known, that is clearly a disadvantage of this regularization method which uses the input models as reference. Employing the data from other sources e.g. altimeter or in-situ for the regularization will also force the gravity recoveries towards those data. Obviously, more studies should be addressed to the regularization methods.

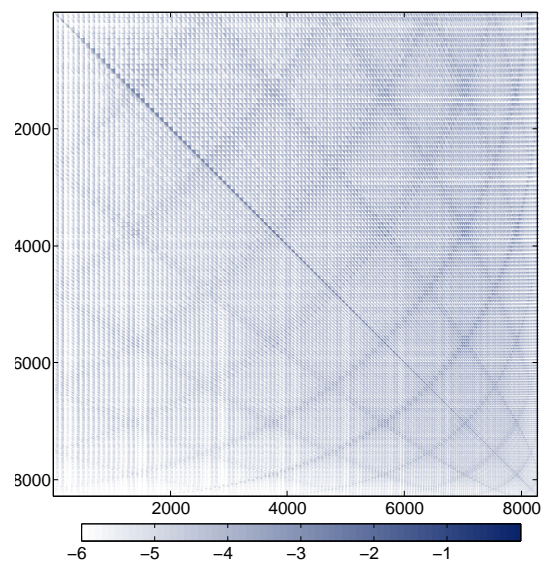


Figure 6.24: The regularization filter operator  $F_{\text{reg}}$  of 6-day solution of scenario 7.1 ( $\lambda = 5$ ). The color-bar is in logarithmic scale.

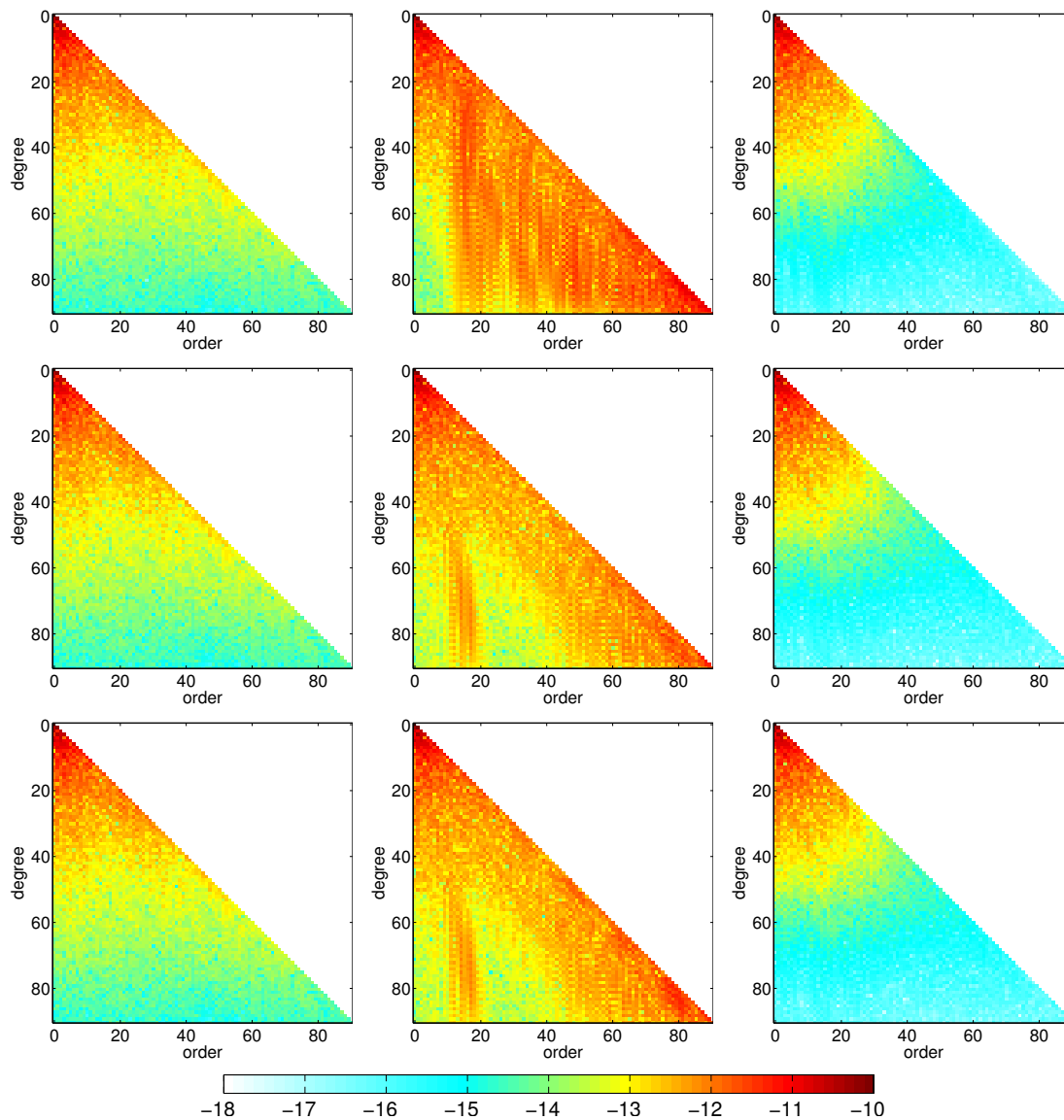


Figure 6.25: The spherical harmonics of the mean input models (left) and the recoveries before (middle) and after (right) regularization for a 6-day recovery of scenario 7.1 (top) and 3-day recoveries of scenarios 7.2 (middle) and 7.3 (bottom) for maximum degree 90. The regularization parameter  $\lambda$  is set to 5 as a near-optimal value. The values are in logarithmic scale.

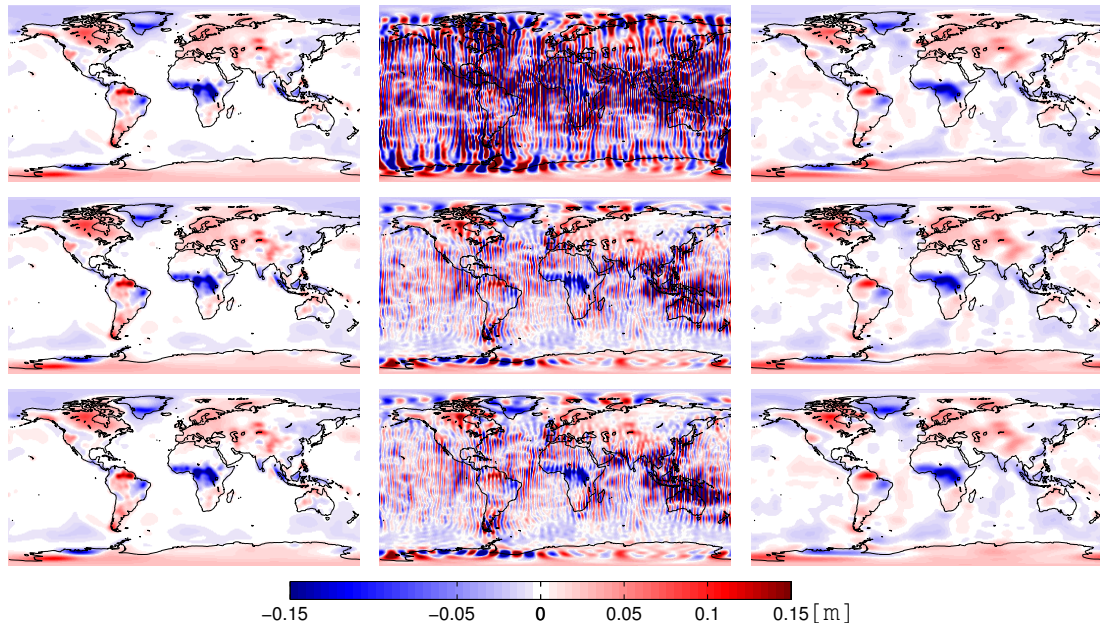


Figure 6.26: Corresponding EWH maps of Figure 6.25

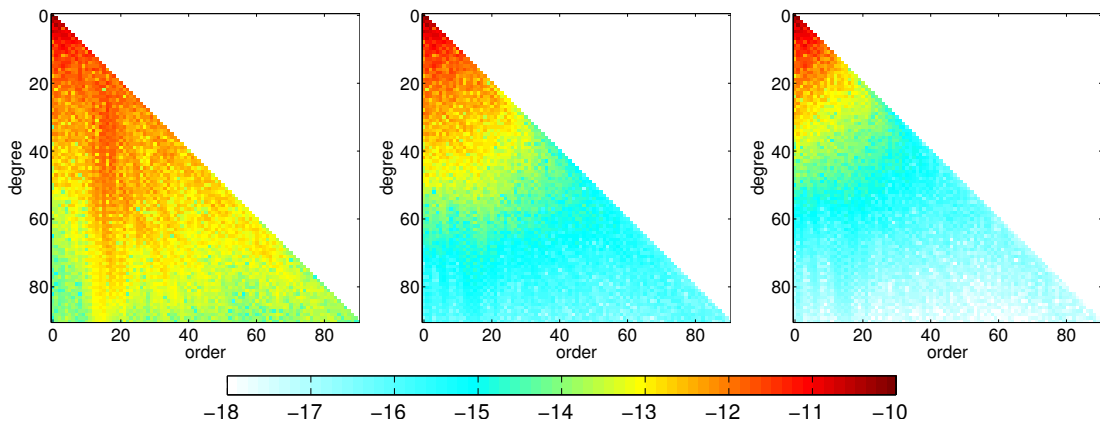


Figure 6.27: Effect of different regularization parameter,  $\lambda$ , on SH spectrum of 6-day solution of scenario 7.1:  $\lambda = 0.01$  (left),  $\lambda = 5$  (middle) and  $\lambda = 100$  (right). The coefficients values are in logarithmic scale.

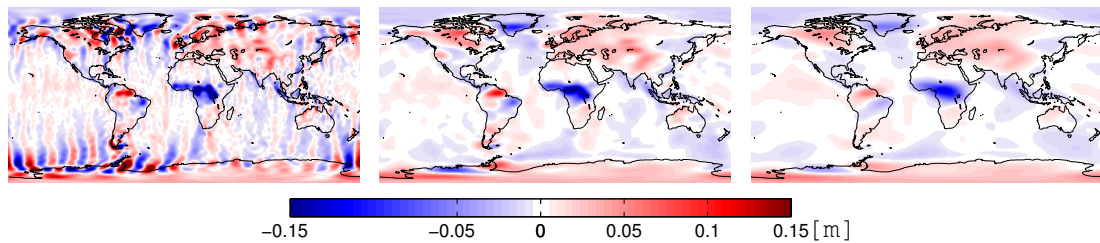


Figure 6.28: Corresponding EWH maps of Figure 6.27.



# 7 Conclusions and Recommendations

## Sampling Theorems

The possibility of having high temporal and spatial resolutions at the same time are restricted by a Heisenberg-type principle in satellite geodesy and the Colombo-Nyquist rule. However the modified Colombo-Nyquist rule of this thesis research states that the spatial resolution of gravity recovery of a satellite mission is significantly improved with the number of satellite revolutions to be equal the maximum spherical harmonic ( $B \approx L_{\max}$ ). The modified Colombo-Nyquist rule enables higher temporal resolution of gravity recoveries, while the high noise level by spatial aliasing of the sub-Nyquist solutions can be dealt by post-processing methods. That means for a single pair satellite mission, an almost good gravity recovery of 6-day for maximum degree 90 is achievable (provided that the ground-track coverage is homogeneous enough). By employing two satellite pairs, one in near-polar orbit and the other in an inclined orbit, this is even achievable by 3-day solutions according to an interpretation of the modified CNR for dual formation missions. Strictly speaking, the latter solution is actually of higher quality. The reason is that an inclined formation rather increases isotropy by adding East-West measurement components instead of only doubling the amount of samples. Moreover, the 3-day solution benefits from higher temporal resolution and consequently less temporal aliasing. An important benefit of having such short time-interval solutions is that they can be applied as dealiasing products (e.g. Wiese et al., 2011a) independent from state of the art geophysical models when aiming of time-variable gravity recoveries of longer time spans, e.g. monthly solutions. Comparing the 6-day recoveries of single inline satellite missions and 6-day recoveries of two pairs missions implies at least 10 times improvement by employing dual satellite missions. Obviously, the quality improvement depends on the altitude, but no significant correlation between the repeat orbits of the dual satellite mission scenarios and the quality of the solutions has been detected. For the dual pair satellite missions with polar gap, it has been shown that the scenarios with small polar-gaps (e.g.  $7^\circ$ ) can be considered as options for the future satellite missions as they may improve the quality of the solutions in the low latitudes. The poor quality of polar-gap area can be adjusted by post-processing tools such as regularization methods. Clearly, the maximum degree of recovery has an important effect on the solutions' quality in the lower latitudes.

**Orbital Parameters** It has been shown that using alternative formations like Pendulum and Cartwheel, the quality of the gravity solutions is considerably improved. However, some technical challenges like the stability of formation and the pointing issues with the tracking system prevent employing them in the near future. On the other hand, a conservative pendulum formation with a small opening angle (GFO) is technically more realistic, while it improves the gravity recovery quality for high degrees and low latitudes.

The selection of orbital parameters, especially homogeneous and smooth gap evolution with avoidance of large unobserved gap (in particular of those in drifting orbit with one day sub-cycle) and the mission altitude have important roles in the quality of gravity solutions. Other important key factors which may influence the recovery quality are addressed to the future works. In particular, it would be of great interest to study the sampling distribution of satellite missions on longitudinal-latitudinal global grids and its possible effect on quality

of the gravity recovery. That is also on demand to investigate the effect of distribution of ground-track patterns of dual pairs satellite missions on the recoveries' quality in more details.

It has also been discussed that employing two satellite missions considerably improves quality of the gravity recovery. Wiese et al. (2011b) suggest a range of parameters' choices, while the mission target is very important for the selection. This work has benefited from Wiese et al. (2011b) suggestions for orbital parameters, although this thesis study has investigated the effects of some orbital parameters on quality of the short-time gravity solutions (as called sub-Nyquist solutions). A combination of a near-polar GRACE-like or conservative pendulum (GFO) formation with a  $72^\circ$  inclined inline formation at altitude around 300 km has been selected as possible optimal future satellite gravity mission scenarios for the sub-Nyquist recovery.

Several repeat orbits with different altitudes and ground-track pattern evolutions have been used as the search space for finding optimal scenarios of single pair and double pair missions. Clearly, more comprehensive search space and finding strategies are necessary to look for the optimal scenarios. One possibility is to employ genetic algorithm to look for the best scenarios for the sub-Nyquist solutions, as it has been used for the full repeat period gravity recovery over the preselected parameters by Ellmer (2011).

### **Error Analysis**

This work has used the error simulation by 10% of the input geophysical models (AOHIS) as the unknown or models' error for the post-processing sections. The simulation then included the models' error, white noise and ocean tide error. That means 90% of the input models (AOHIS) are assumed as known signals or background models. This assumption, however, considers a very simple model for the error simulation which is indeed not realistic. For the future works, more realistic and sophisticated models' errors should be investigated. One possibility for such error scenarios is by introducing difference of two models of a same geophysical field as model error of a geophysical field, as it has been assumed for ocean tide error of this study.

The study of different orbit configurations and formation flights of this dissertation was based on a quick-look simulation tool. The tool assumes a constant repeat orbit,  $\beta/\alpha$ , (nominal orbit) for the satellite mission. This assumption is, however, not realistic, since the orbital parameters of the satellite mission changes with the time-variable gravity field of the Earth. However, the final gravity products of the orbit simulations of the quick-look tool of this study have shown a very good agreement with the results of an orbit-integration simulation package. Moreover, because of avoiding the orbit integration, the quick-look software performance is very fast. Therefore, the tool is suggested for a quick analysis of the gravity recovery by different mission scenarios. The quick-look tool then provide general assessment of those mission scenarios which can later be analyzed by more realistic tools in details.

The simulation procedure of this research has considered the time-variable gravity models of some geophysical fields in atmosphere, ocean, hydrology, ice and solid Earth (AOHIS). Furthermore, the difference of two ocean tide models (tidal error) has been added to the gravity fields as a source for colored noise. The third body gravitational forces (by the Sun, the Moon and the planets) as well as the non-gravitational forces (like atmospheric drag force, radiation pressure, and etc.) and the sensors' colored noise have not been included in the simulation of satellite mission scenarios. The study has only looked for fast analysis of closed loop simulation of satellite missions, affected by time-variable gravity fields and

therefore did not include all the other forces on the satellites as it did not include the errors which are regarding to the measurement devices. Further works should consider more realistic scenarios. In particular, it would be of great interest to investigate the effect of colored noise, produced by satellite sensors and instruments, on different time intervals of gravity solutions of different mission scenarios.

## **Post-processing**

The post-processing tools of this research study has included a white noise filter, based on EOF+KS-Test analysis and a regularization method which in general deals with all kinds of noise. The tools are employed to deal with the high noise level of short-time interval gravity solutions due to the spatial aliasing. However, it is very important to know that both filter approaches suffer from disadvantages and may remove some of the geophysical signals as well. The performance of the filters is highly dependent on the filters' parameters (the significance level,  $\alpha$ , of KS-Test and the regularization parameter,  $\lambda$ , of the regularization approach). Obviously, further researches should be addressed to the filter design for both white and colored noise in the future works.



# Bibliography

- Aguirre-Martinez, M., and N. Sneeuw (2002) *Needs and tools for future gravity measuring missions*, Space Science Reviews, 108, 409–416.
- Allinson, C. R., P. J. Clarke, S. J. Edwards, M. A. King, T. F. Baker, and P. R. Cruddace (2004) *Stability of direct GPS estimates of ocean tide loading*, Geophys. Res. Lett., 31, L15603, doi:15610.11029/12004GL020588.
- Alnis, J., A. Matveev, N. Kolachevsky, T. Udem, and T. W. Hansch (2008) *Sub-hertz linewidth diode lasers by stabilization to vibrationally and thermally compensated ultralow-expansion glass Fabry-Pérot cavities*, Physical Review A, 77 (5), doi: 10.1103/PhysRevA.77.053,809.
- Balmino, G., E. Schrama, and N. Sneeuw (1996) *Compatibility of first-order circular orbit perturbations theories; consequences for cross-track inclination function*, Journal of Geodesy, Vol. 70:554–561.
- Bender, P. (1992) *Integrated laser Doppler method for measuring planetary gravity fields*, in From Mars to Greenland: Charting Gravity with Space and Airborne Instruments, edited by O. L. Colombo, pp. 63–72.
- Bender, P. L., J. L. Hall, J. Ye, and W. M. Klipstein (2003) *Satellite-satellite laser links for future gravity missions*, Space Science Reviews, 108, 377–384, doi: 10.1023/A:1026195913,558.
- Bender, P. L., D. N. Wiese, and R. S. Nerem (2008) *A possible dual-GRACE mission with 90 degree and 63 degree inclination orbits*, Proceedings of the third international symposium on formation flying, missions and technologies. ESA/ESTEC, Noordwijk, pp 1–6.
- Boes, D. C., F. A. Graybill, and A. M. Mood (1974) *Introduction to the Theory of Statistics*, 3rd ed. New York: McGraw-Hill.
- Bonin, J. A., S. Bettadpur and B. D. Tapley (2012) *High-frequency signal and noise estimates of CSR GRACE RL04*, Journal of Geodesy, Vol. 86:1165–1177, doi: 10.1007/s00190-012-0572-5.
- Bos, M. S., T. F. Baker, K. Røthing, K., and H.-P. Plag (2002) *Testing ocean tide models in the Nordic seas with tidal gravity observations*, Geophysical Journal International, 150, 687–694.
- Bouman, I., and R. Koop (1998) *Regularization in gradiometric analysis*, Physics and Chemistry of the Earth 23:41–46.
- Chambers, D. P. (2006) *Evaluation of new GRACE time-variable gravity data over the ocean*, Geophysical Research Letters, 33, L17,603, doi: 10.1029/2006GL027,296.
- Chen, J. L., M. Rodell, C. R. Wilson, and J. S. Famiglietti (2005) *Low degree spherical harmonic influence on Gravity Recovery and Climate Experiment (GRACE) water storage estimates*, Geophysical Research Letters, 32, L14405, doi: 10.1029/2005GL022964.
- Chen, J. L., C. R. Wilson, B. D. Tapley, and S. Grand (2007) *GRACE detects coseismic and postseismic deformation from the Sumatra-Andaman earthquake*, Geophysical Research Letters, 34, L13,302, doi: 10.1029/2007GL030,356.
- Colombo, O. (1984) *The global mapping of gravity with two satellites*, In: Netherlands Geodetic Commission, in publications on Geodesy, vol 7(3).
- Colombo, O. L., and B. F. Chao (1997) *Advanced techniques for mapping gravity and*

## Bibliography

- its changes from space*, in Proceedings of the International GraGeoMar-97 Symposium on Marine Gravimetry, Marine Surveying, and Navigation, IAG Series.
- Davis, J. L., M. E. Tamisiea, P. Elósegui, J. X. Mitrovica, and E. M. Hill (2008) *A statistical filtering approach for gravity recovery and climate experiment (GRACE) gravity data*, Journal of Geophysical Research, 113, B04,410, doi: 10.1029/2007JB005,043.
- Doodson, A. T. (1924) *Meteorological perturbations sealevel and of tides*, Mon. Not. R. Astron. Soc., Geophys. Suppl., 1, 124.
- Drinkwater, M., R. Haagmans, D. Muzzi, A. Popescu, R. Floberghagen, M. Kern, and M. Fehringer (2007) *The GOCE gravity mission: ESA's first core explorer*, in Proceedings of the Third GOCE User Workshop, pp. 1–7, Frascati, Italy, ESA SP-627.
- Duan, X. J., J. Y. Guo, C. K. Shum, and W. van der Wal (2009) *On the post-processing removal of correlated errors in GRACE temporal gravity field solutions*, Journal of Geodesy, 83, 1095–1106, doi: 10.1007/s00,190–009–0327–0.
- Eanes, R. J. (1994) *Diurnal and semidiurnal tides from TOPEX/POSEIDON altimetry*, EOS Trans. AGU, 75, 108.
- Egbert, G. D., and S. Y. Erofeeva (2002) *Efficient inverse modelling of barotropic ocean tides*, J. Atmos. Ocean. Technol., 19, 183–204.
- Ellmer, M. (2011) *Optimization of the orbit parameters of future gravity missions using genetic algorithms*, MSc thesis, University of Stuttgart
- Elsaka, B. (2010) *Simulated satellite formation flights for detecting temporal variations of the earth's gravity field*, PhD thesis, University of Bonn.
- ESA (2007) *The Future of Satellite Gravimetry*, ESA Report from the Workshop on the Future of Satellite Gravimetry - 12–13 April 2007, ESTEC, Noordwijk, The Netherlands.
- ESA (2008) *Monitoring and Modelling Individual Sources of Mass Distribution and Transport in the Earth System by Means of Satellites*, ESA Final Report - ESA contract 20403.
- ESA (2011) *Assessment of a Next Generation Mission for Monitoring the Variations of Earth's Gravity*, ESA Final Report - Reference SD-RP-AI-0688.
- Flechtner, F., M. Thomas, and H. Dobslaw (2010) *Improved Non-tidal Atmospheric and Oceanic De-aliasing for GRACE and SLR Satellites*, System Earth via Geodetic-Geophysical Space Techniques, Advanced Technologies in Earth Sciences 2010, pp 131–142, DOI:10.1007/978-3-642-10228-8\_11, Springer Verlag.
- Grafarend, E. W. (1991) *Relativistic effects in geodesy*, Report Special Study Group 4.119, International Association of Geodesy, Contribution to Geodetic Theory and Methodology ed. F. Sanso, 163–175, Politecnico di Milano, Milano/Italy.
- Grafarend, E., and J. Awange (2012) *Applications of Linear and Nonlinear Models: Fixed Effects, Random Effects and Total Least Squares*, ISBN 978-3-642-22241-2, Springer.
- Gruber, T., J. L. Bamber, M. F. P. Bierkens, H. Dobslaw, M. Murböck, M. Thomas, L. P. H. van Beek, T. van Dam, L. L. A. Vermeersen, and P.N.A.M Visser (2011) *Simulation of the time-variable gravity field by means of coupled geophysical models*, Earth System Science Data, 3:19–35, doi:10.5194/essd-3-19-2011.
- Han, D., and J. Wahr (1995) *The viscoelastic relaxation of a realistically stratified Earth, and a further analysis of postglacial rebound*, Geophysical Journal International, 120, 287–311.
- Helmert, F. R. (1880) *Die mathematischen und physikalischen Theorien der höheren Geodäsie*, Teubner, Leipzig. Reprint Minerva GmbH, Frankfurt a.M. 1961.

- Hill G. W. (1878) *Researches in the Lunar Theory*, American Journal of Mathematics I:5-26, 129-147, 245-260
- Hofmann-Wellenhof B., H. Moritz (2006) *Physical Geodesy*, Springer; 2nd, corr. ed. edition, ISBN: 3-211-33544-7.
- Iran Pour, S., N. Sneeuw (2012) *Properties and applications of EOF-based filtering of GRACE solutions*, Proceedings of the VII Hotine-Marussi Symposium on Mathematical Geodesy, International Association of Geodesy, Symposia 137, pp 273-277, DOI 10.1007/978-3-642-22078-4\_41, Springer.
- Kaula, W. M. (1966) *Theory of Satellite Geodesy*, Blaisdell Publishing Company, Waltham, Massachusetts.
- Kim, J. (2000) *Simulation study of a low-low satellite-to-satellite tracking mission*, Ph.D. thesis, University of Texas at Austin.
- Klees, R., E. A. Revtova, B. C. Gunter, P. Ditmar, E. Oudman, H. C. Winsemius, and H. H. G. Savenije (2008) *The design of an optimal filter for monthly GRACE gravity models*, Geophysical Journal International, 175, 417-432, doi: 10.1111/j.1365-246X.2008.03,922.x.
- Koch, K. R. (1999) *Parameter Estimation and Hypothesis Testing in Linear Models*, ISBN 978-3-540-65257-1, Springer.
- Koch, K. R., J. Kusche (2002) *Regularization of geopotential determination from satellite data by variance components*, J Geodesy 76: 259-268.doi:10.1007/s00190-002-0245-x.
- Kusche, J. (2007) *Approximate decorrelation and non-isotropic smoothing of time-variable GRACE-type gravity field models*, Journal of Geodesy 81:733-749.
- Kurtenbach, E. (2011) *Entwicklung eines Kalman-Filters zur Bestimmung kurzzeitiger Variationen des Erdschwerefeldes aus Daten der Satellitenmission GRACE*, PhD thesis, University of Bonn.
- Kusche, J. (2007) *Approximate decorrelation and non-isotropic smoothing of time-variable GRACE-type gravity field models*, Journal of Geodesy, 81, 733-749, doi: 10.1007/s00,190-007-0143-3.
- Loomis, B. D., R. S. Nerem, and S. B. Luthcke (2011) *Simulation study of a follow-on gravity mission to GRACE*, Submitted to Journal of Geodesy, 2010.
- Lorenz, Ch. (2009) *Applying stochastic constraints on time-variable GRACE data*, MSc thesis, University of Stuttgart.
- Lyard, F., F. Lefevre, Th. Letellier, and O. Francis (2006) *Modelling the global ocean tides: modern insights from FES2004*, Ocean Dynamics, 56, 394-415.
- Marchetti, P., J. J. Blandino, and M. A. Demetriou (2008) *Electric propulsion and controller design for drag-free spacecraft operation*, J Spacecraft Rockets 45(6):1303-1315.doi:10.2514/1.36307.
- Massey, F. J. (1951) *The Kolmogorov-Smirnov Test for Goodness of Fit*, Journal of the American Statistical Association. Vol. 46, No. 253, 1951, pp. 68-78.
- Matsumoto, K., T. Takanezawa, and M. Ooe (2000) *Ocean tide models developed by assimilating TOPEX/POSEIDON altimeter data into hydrodynamical model: A global model and a regional model around Japan*, J. Oceanogr., 56, 567-581.
- McCarthy, D. D., and G. Petit (2004) *IERS Conventions 2003*, Number 32 in IERS Technical Notes. Verlag des Bundesamts für Kartographie und Geodäsie, Frankfurt am Main.
- Mueller, G., I. Thorpe, P. McNamara, and J. Camp (2005) *Laser frequency stabilization for LISA*, NASA/TM-2005-212794, NASA Goddard Space Flight Center, December 2005.
- Pierce, R., J. Leitch, M. Stephens, P. Bender, and R. Nerem (2008) *Inter-satellite range monitoring using optical interferometry*, Applied Optics, 47, 5007-5019, doi:10.1364/AO.47.005,007.

## Bibliography

- Preisendorfer, R. W. (1988) *Principal Component Analysis in Meteorology and Oceanography*, Elsevier, Seattle.
- Rangelova, E., W. van der Wal, A. Braun, M. G. Sideris, and P. Wu (2007) *Analysis of gravity recovery and climate experiment time-variable mass redistribution signals over North America by means of principal component analysis*, Journal of Geophysical Research, 112(F03002), doi:10.1029/2006JF000615.
- Ray, R. D. (1999) *A global ocean tide model from TOPEX/POSEIDON altimetry: GOT99.2*, NASA Technical Memorandum, 58 pp.
- Ray, R. (2008) *GOT4.7 (2008) (Private communication), extension of Ray R., A global ocean tide model from Topex/Poseidon altimetry*, GOT99.2 NASA Tech Memo 209478, Sept. 1999.
- Reigber, Ch., P. Schwintzer, and H. Lühr (1999) *The CHAMP geopotential mission*, Bolletino di Geofisica Teorica ed Applicata, Vol. 40:285–289.
- Reubelt, T., N. Sneeuw, and M. A. Sharifi (2010) *Future Mission Design Options for Spatio-Temporal Geopotential Recovery*, In: Mertikas SP (Ed.) Gravity, Geoid and Earth Observation. IAG Commission 2: Gravity Field, Chania, Crete, Greece, International Association of Geodesy Symposia, Vol. 135, Springer.
- Rosborough, G. W. (1986) *Satellite orbit perturbations due to the geopotential*, CSR, University of Texas.
- Sasgen, I., Z. Martinec, and K. Fleming (2006) *Wiener optimal filtering of GRACE data*, Studia Geoph et Geod 50:499–508.
- Savcenko, R., and W. Bosch (2008) *EOT08a – empirical ocean tide model from multi-mission satellite altimetry*, Report No. 81, Deutsches Geodätisches Forschungsinstitut (DGFI), München.
- Save, H. V. (2009) *Using regularization for error reduction in grace gravity estimation*, Ph.D. thesis, University of Texas at Austin.
- Schaub, H., and J. L. Junkins (2003) *Analytical Mechanics of Space Systems*, AIAA Education Series, Reston, VA.
- Schenewerk, M. S., J. Marshall, and W. Dillinger (2001) *Vertical ocean-loading deformations derived from a global GPS network*, J. Geod. Soc. Japan, 47, 237–242.
- Schrama, E. J. O. (1989) *The role of orbit errors in processing of satellite altimeter data*, Publications on Geodesy 33, Delft. ISBN-13: 978 90 6132 239 9. ISBN-10: 90 6132 239 1.
- Schrama, E. J. O. (1990) *Gravity field error analysis: Applications of global positioning system receivers and gradiometers on low orbiting platforms*, Technical Memorandum 100769, NASA.
- Schrama, E. J. O. (1991) *Gravity field error analysis: Applications of global positioning system receivers and gradiometers on low orbiting platforms*, J. Geophys. Res., 96(B12), 20,041–20,051, doi:10.1029/91JB01972.
- Schrama, E. J. O., B. Wouters, and D. A. Lavallée (2007) *Signal and noise in gravity recovery and climate experiment (GRACE) observed surface mass variations*, Journal of Geophysical Research, 112, B08,407, doi: 10.1029/2006JB004,882.
- Seeber, G. (2003) *Satellite Geodesy: 2nd Edition*, Walter de Gruyter, Berlin.
- Shampine, L. F., and M. K. Gordon (1975) *Computer Solution of Ordinary Differential Equations: the Initial Value Problem*, W. H. Freeman, San Francisco.
- Sharifi, M. A., N. Sneeuw, and W. Keller (2007) *Gravity recovery capability of four generic satellite formations*, In Proc. Kilicoglu, A. and R. Forsberg (Eds.), Gravity Field of the Earth, General Command of Mapping, ISSN 1300-5790, Special issue 18, 211-216.
- Sheard, B. S., G. Heinzl, K. Danzmann, D. A. Shaddock, W. M. Klipstein, and W. M. Folkner (2012) *Inter-satellite laser ranging instrument for the*

- GRACE follow-on mission*, J Geodesy, pp. 29, doi:10.1007/s00190-012-0566-3.
- Sneeuw, N. (2000) *A semi-analytical approach to gravity field analysis from satellite observations*, Dissertationen, Technische Universität München, bei der Bayerischen Akademie der Wissenschaften.
- Sneeuw, N., J. Flury, and R. Rummel (2005) *Science requirements on future missions and simulated mission scenarios*, Earth, Moon, and Planets, 94, 113–142.
- Sneeuw, N. (2006a) *Lecture notes in Physical Geodesy*, Institute of Geodesy, University of Stuttgart.
- Sneeuw, N. (2006b) *Lecture notes in Dynamic Satellite Geodesy*, Institute of Geodesy, University of Stuttgart.
- Sneeuw, N., M. A. Sharifi, and H. Schaub (2008) *Formation Flight Stability in a Gravitational Field*, Proceedings of the 3rd International Symposium on Formation Flying, Missions and Technologies, 23–25 April 2008. ESA/ESTEC Noordwijk, The Netherlands.
- Standish, E. M. (1998) *JPL Planetary and Lunar Ephemerids DE405/LE405*, Jet Propulsion Laboratory, Pasadena.
- St. Rock, B., J. J. Blandino, and M. A. Demetriou (2006) *Propulsion requirements for drag-free operation of spacecraft in Low Earth Orbit*, J Spacecraft Rockets 43(3):594–606. doi:10.2514/1.15819.
- Swenson, S., and J. Wahr (2006) *Post-processing removal of correlated errors in GRACE data*, Geophysical Research Letters, 33, L08,402, doi: 10.1029/2005GL025,285.
- Tapley, B. D., S. Bettadpur, M. Watkins, and C. Reigber (2004a) *The gravity recovery and climate experiment: Mission overview and early results*, Geophysical Research Letters, 31, L09,607, doi:10.1029/2004GL019,920.
- Thomas, M. (2002) *Ocean induced variations of Earth's rotation - Results from a simultaneous model of global circulation and tides*, Ph.D. diss., 129 pp., Univ. of Hamburg.
- Thomas, I. D., M. A. King, and P. J. Clarke (2007) *A comparison of GPS, VLBI and model estimates of ocean tide loading displacements*, J Geod (2007) 81:359–368, doi: 10.1007/s00190-006-0118-9.
- Torge, W. (2001) *Geodesy*, 3rd Edition, Walter de Gruyter, Berlin, 2001.
- Touboul, P., E. Willemenot, B. Foulon, and V. Josselin (1999) *Accelerometers for CHAMP, GRACE, and GOCE space missions: synergy and evolution*, Bollettino di Geofisica Teorica ed Applicata, 40, 321–327.
- Van Beek, L. P. H., Bierkens, and M. F. P. (2008) *The Global Hydrological Model PCR-GLOBWB: Conceptualization, Parameterization and Verification*, Report, Department of Physical Geography, Utrecht University, Utrecht, The Netherlands.
- Van de Berg, W. J., M. R. Van den Broeke, C. H. Reijmer, and E. van Meijgaard (2005) *Characteristics of the Antarctic surface mass balance, 1958-2002, using a regional atmospheric climate model*, Annals of Glaciology, 41, 97–104.
- Visser, P. N. A. M., N. Sneeuw, T. Reubelt, M. Losch, and T. van Dam (2010) *Spaceborne gravimetric satellite constellations and ocean tides: aliasing effects*, Geophysical Journal International, 181 (2), 789–805, doi: 10.1111/j.1365–246X.2010.04,557.x.
- Visser, P. N. A. M., E. Schrama, N. Sneeuw, and M. Weigelt (2011) *Dependency of resolvable gravitational spatial resolution on space-borne observation techniques*, in Geodesy for Planet Earth, Proceedings of the 2009 IAG Symposium, Buenos Aires, Argentina, International Association of Geodesy Symposia, vol. 136, edited by S. Kenyon, M. Pacino, and U. Marti, Springer.

## Bibliography

- Wahr, J., M. Molenaar, and F. Bryan (1998) *Time variability of the Earth's gravity field: hydrological and oceanic effects and their possible detection using GRACE*, Journal of Geophysical Research, 103 (B12), 30,205–30,229.
- Weigelt, M., M. Sideris, and N. Sneeuw (2009) *On the influence of the ground track on the gravity field recovery from high-low satellite-to-satellite tracking missions: CHAMP monthly gravity field recovery using the energy balance approach revisited*, J. Geod., 83(12), 1131–1143, doi: 10.1007/s00190-009-0330-5.
- Weigelt M., N. Sneeuw, E. J. O. Schrama, and P. N. A. M. Visser (2012) *An improved sampling rule for mapping geopotential functions of a planet from a near polar orbit*, J Geodesy.
- Wiese, D. N., W. M. Folkner, and R. S. Nerem (2009) *Alternative mission architectures for a gravity recovery satellite mission*, J Geodesy 83:569-581.doi:10.1007/s00190-008-0274-1.
- Wiese, D. N., P. Visser, and R. S. Nerem (2011a) *Estimating low resolution gravity fields at short time intervals to reduce temporal aliasing errors*, J Advances in Space Research doi:10.1016/j.asr.2011.05.027.
- Wiese D. N., R. S. Nerem, and F. G. Lemoine (2011b) *Design considerations for a dedicated gravity recovery satellite mission consisting of two pairs of satellites*, J Geodesy 86:81–98.doi:10.1007/s00190-011-0493-8.
- Wouters B., and E. J. O. Schrama (2007) *Improved accuracy of GRACE gravity solutions through empirical orthogonal function filtering of spherical harmonics*, Geophys. Res. Lett. 34, doi: 10.1029/2007GL032098.
- Xu, P. (1992) *The value of minimum norm estimation of geopotential fields*, Geophysical Journal International 111:170–178.

# Acknowledgments

Foremost, I would like to express my sincere gratitude to my PhD supervisor, Prof. Dr. Nico Sneeuw for the continued support and guidance with this research project. My special thanks also goes to Prof. Dr. Jakob Flury for his evaluation of my thesis. I also owe many thanks to Dr. Tilo Reubelt for his enormous assistance and support during my research, as well as Dr. Matthias Weigelt for his kind advice and discussions over the topics of this work. My gratitude also goes to Prof. Dr. Wolfgang Keller and Dr. Friedrich Krumm. I took advantage of their lectures for my research. Also, my appreciation to Mrs. Anita Vollmer, secretary of the institute, for her overall help with the official PhD procedure at the university. I am also very grateful to my colleagues Dr. Markus Antoni and Balaji Devaraju for their help during my works at the institute.

This research was funded by the BMBF research program “Geotechnologies–Observation of the System Earth from Space” through the German joint research project “Concepts for Future Gravity Field Satellite Missions”. Here, I would like to acknowledge all the project partners of the research program.

At the end, I would like to give a very special thank you to my parents and brothers for supporting and encouraging me during the whole life.